Nordic Concrete
Research

Nordic
Concrete
Federation

NORDIC CONCRETE RESEARCH

Preface

Nordic Concrete Research (NCR) has during more than 35 years been an important publication for publishing scientific contributions on concrete research conducted in the Nordic countries, i.e., in Denmark, Finland, Iceland, Norway, and Sweden. During these years, there has been a rapid development in the concrete area and the Nordic concrete research has had an important role for the development in several sub-areas, e.g., durability, high performance concrete and self-compacting concrete.

The need of further research is still great and seems to be endless. The subjects for the concrete research changes slowly and the research methods have to a large extent moved from experimental to numerical studies but laboratory experiments and field studies will always be necessary for at least verification. While the changes in subjects and methods are slow, there is a rapid change in publication activities. Paper books and paper journals are to a large extent replaced by Internet searches and electronic journals. Young researchers search their background information, comparison test series, and references on Internet and not in the libraries. PhD students and young researchers have always constituted the lion's part of Nordic concrete research and these are the primary authors of NCR. The Nordic Concrete Federation and its Research Committee, that also constitutes the Editorial Board of NCR, have decided that NCR shall transfer from a paper journal to an electronic journal, where readers may read all papers free of charge. This system is called "Open Access" and is recommended by both universities and research councils to facilitate dissemination of new knowledge. Thereby, we are confident that NCR will attract both more authors and more readers. Due to highly appreciated financial support from the Nordic cement industry, also submitting papers will be free of charge. This volume of NCR is the last paper version.

You are most welcome to submit research articles to the new, electronic Nordic Concrete Research and its first volume that is scheduled for June 2018. For more information on the Nordic Concrete Federation and Nordic Concrete Research, see www.nordicconcrete.net. But for time being, I wish you an interesting reading of this volume's eight papers covering both new materials, e.g., textile reinforced reactor powder concrete, basalt fibre concrete, and light weight aggregate concrete, and analysis of existing concrete structures.

Stockholm in December 2017

Johan Silfwerbrand
Editor of NCR

iv

PUBLICATION NO. 57 2/2017

CONTENTS

Assessment of Existing RC Structures by Virtue of Nonlinear FEM: Possibilities and Challenges

Jiabin Li
Associate Professor, Dr.-Ing.
Oslo and Akershus University College
Pilestredet 35, N-0130 Oslo, Norway
Mailto: lijiabin6598@hotmail.com
Professor, Dr.-Ing.
KU Leuven Campus Bruges
Spoorwegstraat 12, 8200 Bruges, Belgium
Mailto: jiabin.li@kuleuven.be

Glenn Strypsteen
PhD candidate
KU Leuven Campus Bruges
Spoorwegstraat 12, 8200 Bruges, Belgium
Mailto: glenn.strypsteen@kuleuven.be

Mahdi Kioumarsi
Associate Professor, PhD.
Oslo and Akershus University College
Pilestredet 35, N-0130 Oslo, Norway
Mailto: Mahdi.Kioumarsi@hioa.no

ABSTRACT
This paper discusses the possibility and challenges of the assessment of the structural integrity and safety of existing reinforced concrete (RC) structures by virtue of the nonlinear finite element method (FEM). The possibility and viability of applying this tool to predict the mechanical behaviour of existing RC structures are discussed through two sample applications, which deal with the estimation of the actual loading capacities of a RC column-slab joint strengthened by steel plates and a RC parapet element with inadequate transverse reinforcements according to current design codes. The numerical results demonstrate that when properly used, the nonlinear FEM is able to effectively remedy the inadequacy of conventional design and analysis procedures. Some remaining challenges for the utilisation of nonlinear FEM to assess existing RC structures are then discussed.

Key words: Existing reinforced concrete (RC) structures, structural safety, remaining loading capacity, finite element method (FEM), microplane model

1.   INTRODUCTION

The assessment of the real structural integrity and safety of existing reinforced concrete (RC) structures is becoming a more and more important issue for civil engineers. The actual load carrying capacities or the safety factor of existing RC structures need to be known owing to the following reasons:

- Increased loads on existing structures (particularly on bridges due to the increase of the traffic load);
- Material deteriorations such as the corrosion of reinforcing steel and the alkali silica reaction (ASR) damage in concrete;
- The generation of new design codes;
- Pre-existing damages in the structures (e.g. premature cracking in concrete) as well as structural faults (e.g. design and construction error).

Nonlinear finite element method (FEM) provides an efficient tool for the realistic assessment of the actual behaviour and failure of existing RC structures. Since the pioneering work of Ngo and Scoreless [1], numerous efforts have been made in this field, mainly in constitutive modelling of the material behaviour and development of sophisticated analysis algorithms [2]. Given these continuous progresses, nonlinear FEM simulation of RC structures has matured to a significantly high level. Compared to three decades ago, many problems encountered in the engineering practice can be better investigated today by using of this tool. In addition, there is no limit to the applications of this method.

A number of successful applications of nonlinear FEM in the assessment of existing RC structures and bridges including some very complex structural systems have been reported in the literature [3-6]. By virtue of this method, the mechanical responses and failure loads of the investigated structures have been better understood. This has led to more rational and economical strategies for the structures. In the past several years, the first author of this paper has successfully completed a series of structural assessments of various types of existing RC structures through the use of nonlinear FEM, with significant economical and environmental benefits. These benefits have been achieved by avoiding unnecessary material consumptions and construction activities. Two sample applications are presented below.

2.   TWO SAMPLE APPLICATIONS

2.1   Prediction of loading capacity of a RC column-slab connection

In one building in the Public Hospital in Graz, Austria, steel profiles were used to strengthen the RC column-slab connections to benefit the load transfer among different components. The concept of the construction is illustrated in Figure 1, in which a typical type of the column-slab connection is shown. In this element, the RC column has a cross section of 300×400 mm^2. The thickness of the concrete cover is 30 mm. The inner steel profile has a rectangular cross section (width: 30 mm, height: 150 mm) while the outer steel profile is a U-shaped profile, which is U120/55/6 mm according to DIN 1026-1. No shear connectors were used between the steel profiles and the column concrete as well as between the steel profiles and the slab concrete. Outside the column-slab connection region, unreinforced concrete was filled into the steel

profiles. The basic design consideration is that the slab loads transfer firstly to the steel profiles then from the steel profiles further to the RC column.

A notable (or perhaps less efficient) point of this design is that the inner steel profiles are placed (more or less) directly on the RC column concrete cover, see Figure 2.

(a) Three-dimensional (3D) view (b) Top view
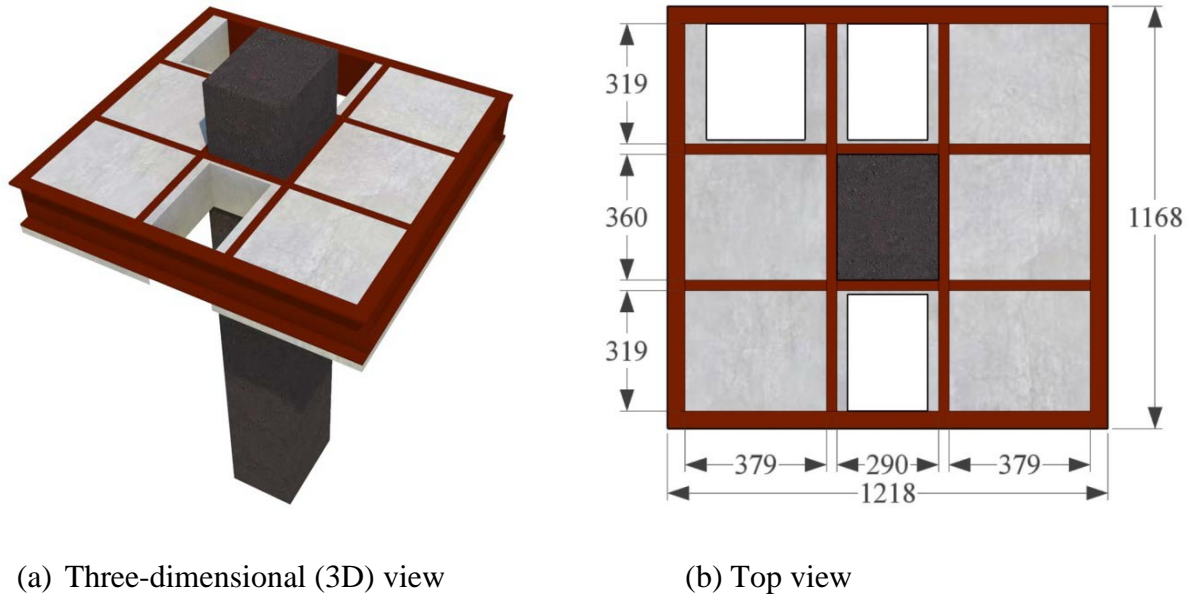
Figure 1 – Construction concept of a typical column-slab connection strengthened by steel profiles (Units: mm. Note: There are openings in the slab).
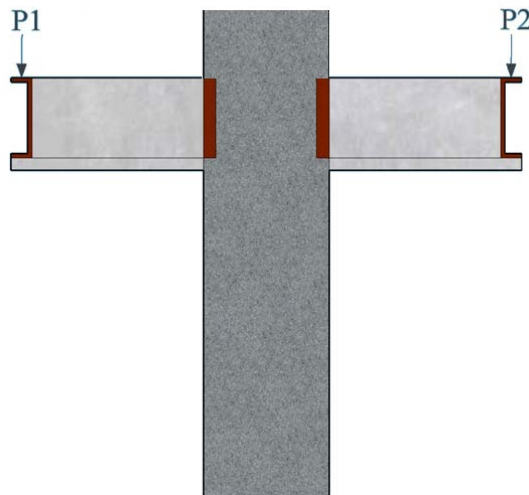
Figure 2 – Designed (favorable) positions of steel profile with reference to RC column.

After the construction, however, it was found that the inner steel profiles of many column-slab connections are located in rather unfavorable positions. Some typical cases are illustrated in Figure 3. In the case shown in Figure 3(a), the left inner steel profile is supported on the concrete cover with a distance of 10 mm from the left edge of the steel profile to that of the column concrete cover; while the right inner steel profile is placed outside the column concrete

cover (!). In the case in Figure 3(b), the left steel profile is precisely placed on the column concrete cover while the right profile is only partially (10 mm!) supported on the column cover.

(a) Unfavorable position 1   (b) Unfavorable position 2
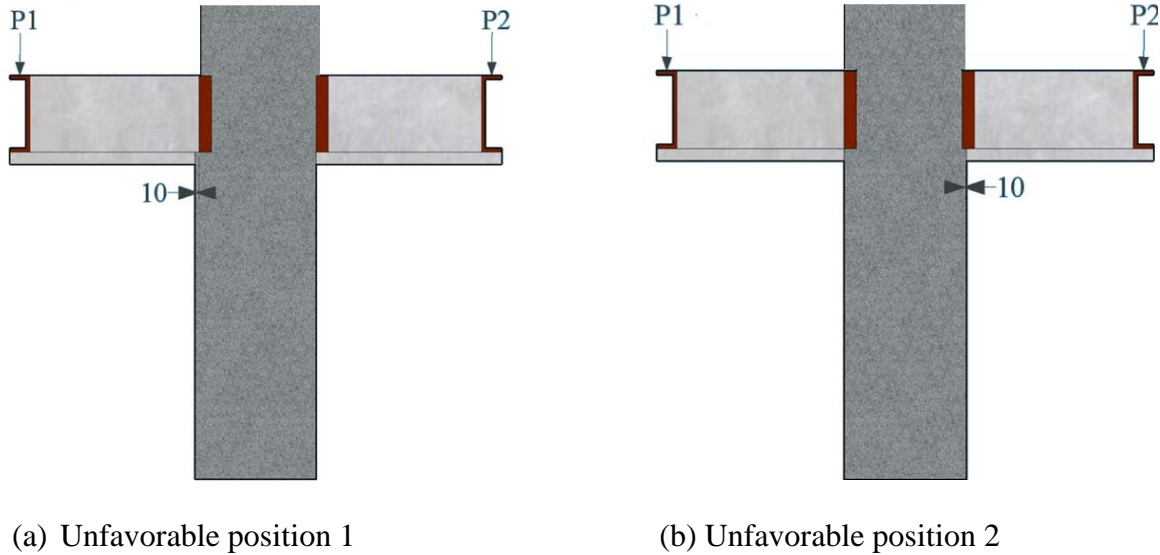
Figure 3 – Typical actual (unfavorable) positions of steel profile with reference to RC column.

There are several types of column-slab connections in the building. The differences between various connection types include the structural dimensions, the column and the slab concrete strength grades as well as the service load level. A simplified engineering analysis, in which the slab loads are assumed to be completely exerted on the column concrete cover, indicated that under the service slab load, a high splitting stress occurs in the column cover concrete and longitudinal cracks formulate in the column cover concrete. Thus, a common opinion had been that when the loads on the slab increase to the ultimate load level, a spalling of the column concrete cover would occur and the steel profiles would then fall to the ground. Thus, a rehabilitation of the structure had been considered to be necessary.

The building had been in service for several years. However, on-site monitoring did not detect any visible longitudinal cracks in the column cover concrete. This is inconsistent with the results of the simplified analysis since longitudinal cracking in the column cover is expected according to the analysis. To better understand the real behaviour of the structure, more sophisticated analysis is obviously required. Three-dimensional (3D) nonlinear FEM simulations were thus performed to investigate the responses of the structure under ultimate design load.

Since the objective of this section is to demonstrate the possibility and viability of the use of nonlinear FEM to predict the load carrying capacity and failure behaviour of exiting RC structures, it is not the intention of the authors to let the readers repeat these simulations. Thus, a very detailed description of the numerical models and procedures is not given here. The modelling details of the column-slab connections can be found in [7-9]. In this part, only the two most important points in the numerical simulations of the structures are highlighted, which are the constitutive modelling of the column concrete and slab concretes, as well as the simulation of the contact between the steel profiles and concretes. The microplane model M4L for concrete developed in [10-12] was employed to simulate the mechanical behaviour of the concretes. This model has been proven to be able to realistically capture the uniaxial, biaxial and triaxial

mechanical behaviour of concrete. More information about the numerical performance of the model for simulating the concrete properties under different kinds of stress states are presented in [11-12]. The discrete contact spring model [9] is employed to simulate the interface behaviour between the steel profiles and the column as well as slab concretes. The constitutive behaviour of the steel material is described by the von Mises yield criterion with isotropic strain hardening and an associated flow rule. Both the concretes and the steel profiles are discretised into 8-node solid elements with $2\times2\times2$ integration points. Figure 4 presents the 3D finite element mesh for a typical connection system.
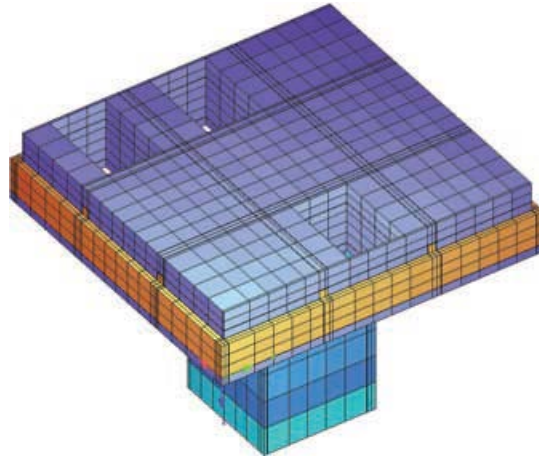

Figure 4 – 3D finite element mesh of a typical column-slab connection.

The detailed numerical simulation results for various connection systems are given in [7], which led to the following interesting findings:

- Under the service slab load, the tensile splitting stress in the column cover concrete is significantly smaller than the concrete tensile strength and thus no cracking in the concrete occurs. This is consistent with the on-site observations;
- The load carrying capacities of the connections are significant higher than that derived by the simplified analysis. The predicted maximum slab loads of the connections are about 2.6 times the service loads, indicating that the load bearing capacities of the connections are adequate according to Eurocode 2 [13];
- For all the investigated connections, the failure was due to the yielding of the inner steel profiles rather than the spalling of the column cover concrete. A falling of the steel profile to the ground at the maximum slab load was not observed in the numerical simulations.

With the guidance of the numerical simulation results, full-scale tests on two types of the connections were performed in the laboratory [14]. The test results were in very good agreement with that predicted by the numerical model. The failure of the tested connections were due to the yielding of the inner steel profiles rather than the spalling of the column cover concrete, and the load carrying capacities of the connection were adequate. More information about the test results and their analysis can be found in [14]. After the tests, numerical analysis of the test specimens was also done using the measured material properties of the column and slab concretes. The predicted deformation behaviour and the failure loads of the connections were very close to the test observations. Figure 5 shows the simulated load-deformation curve of a connection.
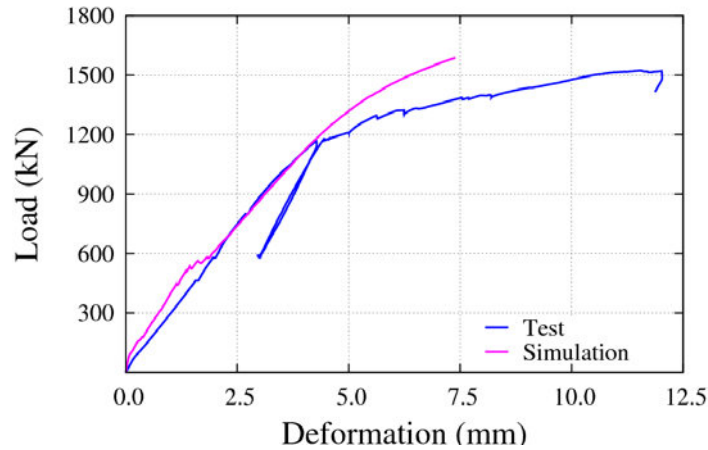
Figure 5 – Comparison of the load-deformation curve from numerical simulation and test.

Because the numerical model was successfully verified by the test data, it is thus possible to investigate the load transfer mechanism in the column-slab system to better understand the actual response of the structure. The analysis results were presented in [9]. It was found that the friction between the inner steel profiles and the column concrete has a significant contribution to the load bearing capacities of the connections. This is because when there is relative movement between the inner steel profile and column concrete under the slab (bending) load, the friction between the surfaces of the two materials activates and this friction transfers a part of the load from the slab to the column core concrete (not the column cover concrete!) . This explains why the actual load carrying capacities of the column-slab connections are much higher than that estimated from the simple engineering analysis.

Further, the load carrying capacities of the rest of the connection systems were predicted by using of the validated numerical model. It was found that all the connections have adequate load bearing capacities. Therefore, no retrofit of the structure is required. This finally led to a significant cost because of the avoidance of unnecessary material consumptions as well as construction activities.

2.2   Estimation of maximum load of a parapet with low transverse reinforcement

This example deals with the load bearing capacity of a RC parapet element with low amount (insufficient) transverse reinforcements according to the design codes. In one garage at the Berlin-Brandenburg International Airport, RC parapet elements were constructed to resist the force of the bracing system. The longitudinal reinforcements in these elements were overlapped with the connecting reinforcements in the foundation. The lapped length of the reinforcements met the requirements of the German design code DIN 1045-1 [15]. However, in some built elements, the amount of the transverse reinforcements for resisting the possible splitting tensile force in the RC parapet element is too low in comparison to that required by DIN 1045-1. The available reinforcements were found to be insufficient to bear the splitting tensile force determined by the engineering model recommended in DIN 1045-1 [15]. Therefore, a post-installation of additional transverse reinforcements had been considered to be necessary. However, this is not an optimal choice since it would impose the structure into an unfortunate condition due to the post installation of additional transverse reinforcements. On the other hand,

since the engineering model in DIN 1045-1 is generally conservative, the use of this model might be inadequate to determine the real load carrying capacity of the parapet elements.

To investigate the real load carrying capacity of the parapet elements, 3D nonlinear FEM simulations were carried out [16]. A representative element was computationally studied. To reduce the computational expense, only a strip of the parapet element (cross section: 400×700 mm^2, height: 950 mm) was simulated. The 3D view and the front view of the modelled parapet element are shown in Figure 6(a) and 6(b), respectively. The longitudinal reinforcements in the modelled parapet element are shown in Figure 7 (a), which include three groups:

- Group 1: 10 Φ10 reinforcements in the outer edge of the cross section;
- Group 2: 4 Φ 25 reinforcements in the middle of the cross section; and
- Group 3: 6 Φ 20 reinforcements between the above two groups of reinforcements.

The transverse reinforcements have a diameter of 10 mm. However, it should be noted that the reinforcements of the top layer are different from that of the other layers, as shown in Figure 7(b) and 7(c), respectively. More details of the modelled parapet element, such as the material properties of the concrete and the reinforcements can be found in [16].

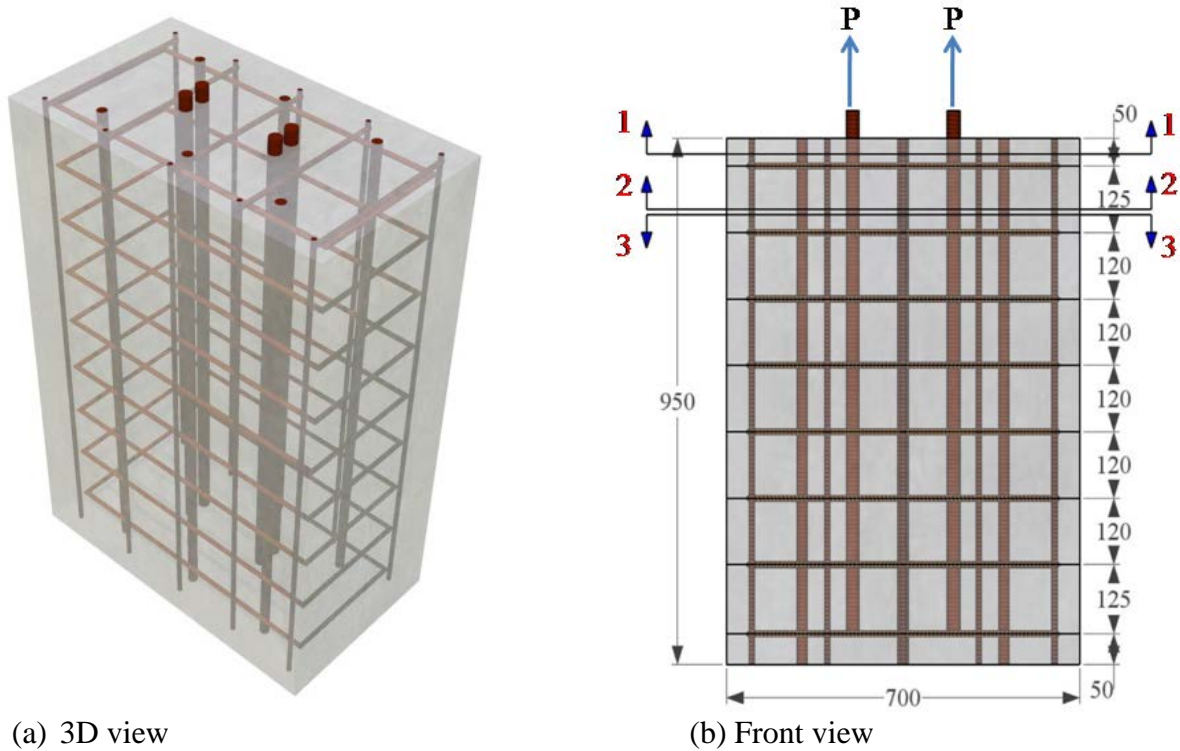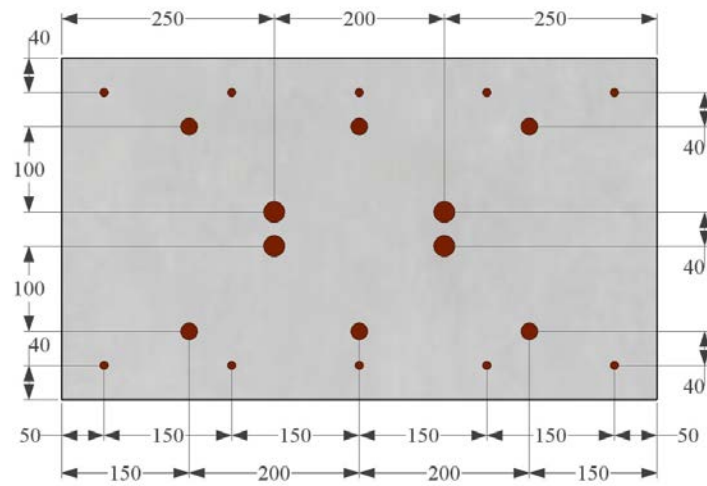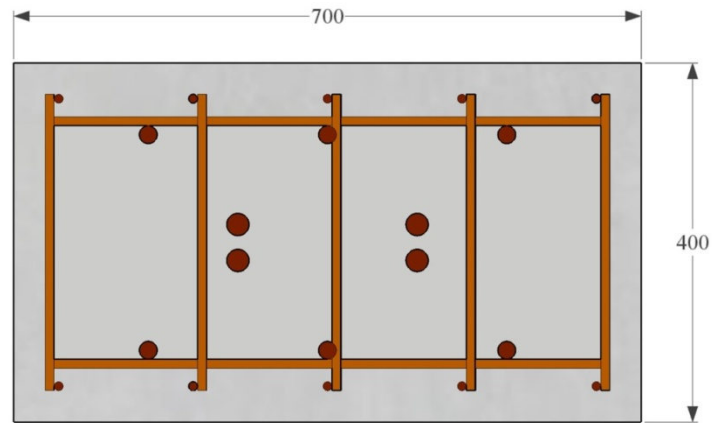(a) 3D view

(b) Front view

Figure 6 – Geometry of the modelled parapet element without additional transverse reinforcement (Units: mm) [16].
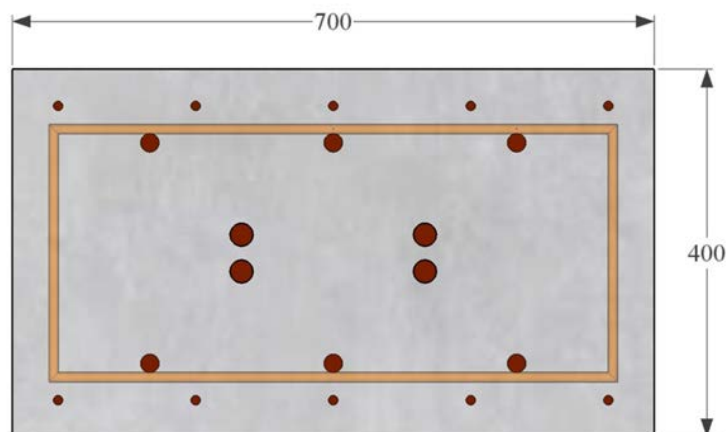
(a) Section 1-1

(b) Section 2-2

(c) Section 3-3

Figure 7 – Details of the reinforcements in the modelled parapet element without additional transverse reinforcement (Units: mm) [16].

The microplane model M4L for concrete [7-9] was again used to simulate the concrete in the parapet element. All the reinforcements in the element were modelled as an elastic-perfect plastic material described by its modulus of elasticity E_s and the yield strength f_y. The bond-slip behaviour between the concrete and the reinforcements plays an important role in the simulation of the element. The bond-slip model in MC90 [17] was employed in the numerical model. The concrete was discretised into 8-node solid elements with $2 \times 2 \times 2$ integration points, while the reinforcing steel was simulated with 2-node truss element. More details about numerical modelling, such as the material parameters, the finite element mesh and the solution algorithm etc can be found in [16].

The numerical results indicated that the failure of the simulated RC parapet element was caused by the yielding of the four axially tensioned reinforcements with a diameter of 25 mm; while an inclined splitting failure in the concrete was not detected. This is due to the fact that the four load-introducing longitudinal reinforcements (Φ 25) have a relatively large side concrete cover. Owing to the thick concrete cover, the low amount of the loading reinforcements and the actual transfer of the load between the reinforcements and the concrete, the splitting failure of the concrete in the element was delayed or prevented. Depending on the bond strength between the concrete and the steel reinforcements, the failure of the parapet element was caused by the pull-out failure or yielding of the four 25 mm diameter longitudinal reinforcements, prior to the tensile splitting failure of the concrete. The predicted failure load, which is in fact the yielding load of the four loading longitudinal reinforcements, is approximately 1.80 times the design load, indicating the parapet element is still on the safe side. An extensive parameter study through varying the tensile strength of the concrete and the bond strength between the concrete and the reinforcing steel was also conducted, yielding a better understanding of the load carrying behaviour of the parapet element. The numerical results and their discussions are given in [16, 18].

On the basis of the numerical simulation results, it was found that no post-installation of additional transverse reinforcement would be necessary.

3.   SOME REMAINING CHALLGENCES

From the above two samples in this paper as well as some other successful applications reported in the literature, it can be concluded that when properly used, nonlinear FEM is able to serve as a very useful tool in the assessment of the real structural integrity and safety of existing RC structures. Despite that, some rather big challenges still remain in the practical application of this tool, especially when the simulations of RC structures are done in engineering offices with commercial finite element packages. Some of these challenges are discussed in the following.

3.1   Numerical Accuracy

The question on how accurate are the numerical results or how confident is the engineer in the calculation results is commonly asked when nonlinear FEM simulations of RC structures are used in engineering practice, in particular when the mechanical behaviour of the structure is not yet fully understood and no test data are available. Numerous excellent simulations of the load-deformation curves of different RC structures have been reported in the literature; however, many results are not adequate if compared with the test observations on the crack propagation,

the reinforcement strain and the failure mode [19].

The robustness and performance of the concrete material model often govern the accuracy of the simulation results. A large amount of concrete constitutive models have been developed. Unfortunately, none of existing models is able to realistically represent all important material behaviour of concrete subjected to general loading conditions, since the modelling of concrete is a notoriously hard task. Most of the models can only yield case-dependent success and there are always arguments on the objectivity of the numerical simulation results. The use of nonlinear FEM simulations incorporating insufficient concrete material models to RC structures in engineering practice can result in very big risk of structural failure, if the real load bearing capacity is overestimated by the numerical model. The formulation of a robust and versatile constitutive model of broad applicability and capability is still a big challenge.

On the other hand, a RC structure consists of different constituents: concrete, reinforcement and sometimes also structural steel. The nonlinear actions of the individual constituents are in some cases an important cause of the responses of the structure. Therefore, material models for these composite actions, such as the bond-slip between reinforcement and concrete, the aggregate interlock (shear friction) in cracked concrete when lateral compression exists, and the dowel action of steel reinforcement as well as the bond-friction between concrete and structural steel, are required to precisely represent the behaviour of the structure. Unfortunately, adequate models for describing these actions are not yet available. Some existing commercial FE packages provide options for simulating some types of actions, e.g. the interface behaviour between concrete and structural steel. However, they generally belong to quite simplified solutions and the scope of application is still rather limited. How to realistically simulate these interaction behaviours and how to select the model parameters in the structural simulations are also big challenging problems and more efforts in this field are necessary.

It is well known that concrete exhibits softening behaviour under many types of loadings. When this material behaviour is included, a problem related to the finite element mesh, known as mesh dependency, frequently occurs, including the dependency on element size and the dependency on mesh pattern. The former refers to the size of the localized zone decreases as the element size decreases. The crack band model is often used in commercial packages to minimise the influence of the element size on the numerical results for tensile dominated failures. However, when the crack band model is used, the simulated cracks tend to develop parallel to the element mesh lines, that is, a dependency of the mesh pattern. For this reason, the crack band model is generally difficult to use unless the crack pattern of the investigated problem is known in advance, which is, however, often not the case for practical applications.

Smeared crack models are commonly implemented in commercial finite element packages for simulating RC structures. However, when the softening branch of the stress-strain curve of concrete is adjusted to keep the fracture energy constant according to the concept of the crack band model, the simulated cracks often occur in multiple elements instead of being localized. This is not correct since the fracture energy and the stress-strain curve are given assuming that the crack is localized in one element. The solution is acceptable only when the used element size coincides with the macroscopic crack spacing of the actual structure.

Other techniques such as the non-local approaches and the gradient type methods might be more suitable for avoiding the mesh dependency problems. However, these techniques are not yet popular and they are absence in most commercial finite element packages. Generally, the mesh dependency in nonlinear FEM simulations of RC structures has not been well solved. Simple and efficient approaches to avoid the mesh dependency are not available. At present, when nonlinear

FEM simulations are used for predicting the behaviour of existing RC structures in practice, it is often recommended that mesh sensitivity tests should be performed to validate the finite element mesh of the model. Different mesh cases with different element sizes and their effects on the numerical results should be assessed [20]. In the case of significant mesh sensitivity, the numerical model should be considered as not objective.

3.2   Numerical Efficiency

When nonlinear FEM simulations are used in engineering offices to investigate the integrity of existing RC structures in practice, the efficiency of the simulations can be even more important than the accuracy. This is because the work in engineering offices has to be concerned with time, money and personnel. In such a case, deadlines are very important and the task must be completed on time with available resources.

Compared to conventional specimens in the laboratory, existing RC structures in the engineering practice are usually of much larger scale. On the other hand, triaxial stress states frequently occur in most RC structures. Hence, 3D modelling needs to be used to achieve more realistic simulation results. Only in some special cases, the problems can be simplified into one- or two-dimensional problems. In the 3D numerical model of a real RC structure, an enormous number of finite elements and degrees of freedoms are often included. Moreover, to accurately represent the structural behaviour, advanced material models are often needed. Numerical experiences indicate that even with today's state-of-the-art computers, nonlinear FEM simulations incorporating sophisticated material models can become computationally intractable in case of large amounts of finite elements and/or complex stress states in structures. In most cases, numerical convergence problems lead to expensive computational cost. The computational expense greatly hampers the practical utilisation of nonlinear FEM simulations of existing RC structures and it can be regarded as one important obstacle.

High performance computers and parallel algorithm on a work station are helpful for reducing the computational time. However, these resources are usually not available in most design or consulting offices. New algorithms, such as multi-scale techniques and parallel algorithm on single or separated personal computer are useful for improving the efficiency of the computer simulations in engineering offices.

3.3   Safety Format

In addition to the accuracy and the efficiency of the computer simulations, the reliability of using the simulation results within codes of practice framework is another important issue. In other words, how to reliably use the simulation results in conjunction with codes of practice? A sound safety format for the numerical analysis is another challenge related to the use of nonlinear FEM in assessing existing structures in engineering practice.

The usual design condition is written as

$$F_d < R_d \tag{1}$$

where, F_d is the design actions and R_d is the corresponding design resistance. F_d is predicted with the mean values of the material parameters while R_d should be assessed using the design

values according to the requirement of the semi-probabilistic approach. Nevertheless, as discussed in [21-22], the mean values of the material parameters should be used in the nonlinear analysis. When the test data are compared with the numerical results, the actual structural behaviour can be reproduced only when the mean values are used. The use of design values in the nonlinear FEM analysis result in an erroneous assessment of the structural behaviour, the deformability and the load bearing capacity. This causes some difficulties for evaluating the reliability when applying the nonlinear simulation results within mostly design code of practice framework.

Several safety formats have been proposed to solve this inconsistency, for example, in [20, 22 23]. However, a sound safety format is still missing, especially when complex material models are used since they are calibrated with limited test data. Currently, the safety of the nonlinear FEM simulations is usually assessed based on the characteristic values of the material properties [24], which are also used in the two sample application presented in this paper. Obviously, there are still some inconsistencies with this methodology.

4.   CONCLUSIONS AND REMARKS

This paper deals with the assessment of existing RC structures by virtue of nonlinear FEM. Two recent sample applications are presented to illustrate the possibility and viability of this tool. Some challenges of using nonlinear FEM in predicting the behaviour of existing RC structures in the engineering practice are also discussed. The following conclusions can be drawn from this study:

- Considerable progress has been achieved in nonlinear FEM simulation of RC structures. Together with the relentless increase of the computer power, this has made it possible to apply nonlinear FEM to assess existing RC structures in practice;
- When properly used, nonlinear FEM is able to provide a very efficient tool to rationally assess the real mechanical response and load carrying capacity of existing RC structures;
- In comparison to conventional analysis or design procedures in current codes of practice, Nonlinear FEM is able to give more realistic descriptions of the real behaviour and load carrying capacity of existing RC structures;
- In spite of many successful applications, nonlinear FEM should be used with caution in the assessment of existing RC structures, especially when used in engineering offices with commercial software;
- There are still several big challenges when nonlinear FEM is utilised to predict the behaviour of existing RC structures. They are mainly related with the numerical accuracy, numerical efficiency and safety format. Further developments in these fields will greatly increase the viability of this tool.

REFERENCES

1.   Ngo D & Scordelis A C: "Finite Element Analysis of Reinforced Concrete Beams," *Journal of American Concrete Institute*, Vol. 64, No. 3, 1967, pp. 152-163.
2.   fib Task Group 4.4. *Practitioners' Guide to Finite Element Modeling of Reinforced Concrete Structures*. Bulletin 45, International Federation for Structural Concrete (fib), 2008.

3.   Mahalingam S & Sharma P: "The Use of Finite Element Analysis in Practical Concrete Design: Case Studies of Longholme Bridges and Other Assessments," *Finite Element in Engineering and Science*, Rotterdam: A.A. Balkema, 1997, pp. 93-106.

4.   Vecchio F J: "Non-linear Finite Element Analysis of Reinforced Concrete: At the Crossroads?" *Structural Concrete*, Vol. 2, No. 4, 2001, pp. 201-212.

5.   Vecchio F J: "Contribution of Nonlinear Finite-Element Analysis to Evaluation of Two Structural Concrete Failures," *ASCE- Journal of Performance and Construction Faculties*, Vol. 16, No. 3, pp. 110-115.

6.   Maekawa K, Okamura H, Pimanmas A: "*Nonlinear Mechanics of Reinforced Concrete*," London: SPON Press, 2003.

7.   Tue N V & Li J: "FE Berechung zur Ermittlung der Traglast von Stützen/Deckenknoten Bauwerk LKH, Graz West, " Technical Report, Institut für Betonbau, TU Graz, 2011.

8.   Tue N V & Li J: "FE Berechnung zur Ermittlung der Traglast von Deckenknoten mit Pilztyp 7, 8 und 9 Bauwerk LKH Graz West, " Technical Report, Institut für Betonbau, TU Graz, 2012.

9.   Tue N V, Li J, Turner K: "Advanced Numerical Simulations for Prediction of Bearing Capacity and Failure of Complex RC Structures," *Structural Engineering International*, Vol. 24, No. 2, 2013, pp. 211-216.

10.   Li J: "*Development and Validation of a new Material Model for Concrete On the basis of Microplane Theory*," Graz: Verlag der TUG, 2011.

11.   Tue N V, Li J, Caner F C: "Microplane Constitutive Model M4L for Concrete. I: Theory," *Computers & Structures*, Vol. 128, 2013, pp. 219-229.

12.   Li J, Tue N V, Caner F C: "Microplane Constitutive Model M4L for Concrete. II: Calibration and Validation," *Computers & Structures*, Vol.128, 2013, pp. 146-159.

13.   European Committee for Standardization (CEN). Eurocode 2. Design of concrete structures, 2009.

14.   Tue N V & Turner K: "Versuchsbericht zum Durchschlupfwiderstand von ausgewählten stahlpilzverstärkten Deckenknoten des LKH Graz West," Technical Report, Institut für Betonbau, TU Graz, 2012.

15.   DIN 1045-1. Tragwerke aus Beton, Stahlbeton und Spannbeton – Teil 1: Bemessung und Konstruction, 2008.

16.   Tue N V, Schneider H, Li J: "Tragfähigkeit der Brüstungen mit geringer Querbewehrung beim Parkhaus PNA des BBI, "Technical Report, Institut für Betonbau, TU Graz, 2011.

17.   CEB-FIP. Model Code (MC) 90. Thomas Telford, 1993.

18.   Tue N V & Li J: "Computer Simulations of RC Structures for Practice," *Structural Engineering International*, Vol. 24, No .2, 2013, pp. 222-228.

19.   Rokugo K & Uchida Y: "Trends in Numerical Analysis of Concrete Structures in Japan," *Finite Element in Engineering and Science*, Rotterdam: A.A. Balkema, 1997, pp.15-25.

20.   Cervenka V: "Reliability-based Non-linear Analysis According to fib Model Code 2010", *Structural Concrete*, Vol. 14, No. 1, 2014, pp. 19-28.

21.   CEB. "New Developments in Non-linear Analysis Methods," Bulletin No. 229, Lausanne, 1995.

22.   Allaix D L, Carbone V I, Mancini G: "Global Safety Format for Non-linear Analysis of Reinforced Concrete Structures," *Structural Concrete*, Vol.14, No.1, 2013, pp. 29-42.

23.   Schlune H, Gylltoft K, Plos M: "Safety Formats for Non-linear Analysis of Concrete Structures," *Magazine of Concrete Research*, Vol. 64, No.7, 2012, pp. 563-574.

24.   Hendriks M A N: "Nonlinear Finite Element Analysis of Concrete Structures," *JCSS Workshop on Semi-probabilistic FEM calculation*, 2009, Delft, the Netherlands.

Nonlinear FEM Simulation of Structural Performance of Corroded RCColumns subjected to Axial Compression

Jiabin Li
Associate Professor, Dr.-Ing.
Oslo and Akershus University College
Pilestredet 35, N-0130 Oslo, Norway
Mailto: lijiabin6598@hotmail.com
Professor, Dr.-Ing.
KU Leuven Campus Bruges
Spoorwegstraat 12, 8200 Bruges, Belgium
Mailto: jiabin.li@kuleuven.be

Gro Markeset
Professor, Dr. Ing.
Oslo and Akershus University College
Pilestredet 35, N-0130 Oslo, Norway
Mailto: Gro.Markeset@hioa.no

Mahdi Kioumarsi
Associate Professor, Dr. Ing.
Oslo and Akershus University College
Pilestredet 35, N-0130 Oslo, Norway
Mailto: Mahdi.Kioumarsi@hioa.no

ABSTRACT

This paper presents a numerical model for predicting the behaviour of reinforced concrete (RC) columns with corroded reinforcing steel subjected to axial compression. The influence of the steel corrosion on the mechanical properties of the rebars and the concrete (in the unconfined cover and the confined core) is taken into account in the numerical model. In addition, the premature buckling behaviour of the corroded longitudinal rebars under compression is also considered. To model the complex material behaviour of the concrete, the recently developed microplane model M4L is used. It is found that the predictions from the computational model are in very good agreement with the test observations.

Key words: Reinforced concrete (RC) column, axial compression, steel corrosion, finite element simulation, microplane model

5.   INTRODUCTION

The corrosion of embedded reinforcing steel is the principal cause of deterioration of reinforced concrete (RC) structures in a chloride-laden environment. The corrosion of the reinforcing steel results in the loss of the steel cross section and of the mechanical properties of the material, the cracking, spalling and delamination of the cover concrete, as well as the decrease of the bond between concrete and steel. As a consequence, the serviceability, the load carrying capacity and the residual service life of the structures are reduced.

Nonlinear finite element method (FEM) provides an important option for studying the response and residual load carrying capacity of corroded RC structures. In the past years, significant efforts have been devoted in this field. Nonlinear FEM simulation of corroded RC structures is often conducted through incorporating the corrosion induced damage into the computational model for non-corroded structures through modifying various input parameters. Most previous efforts were focused on the numerical simulation of the flexural and shear performance of RC members. In these studies, the loss of the cross section and/or the strength and ductility of the reinforcing steel, as well as the reduction of the bond between concrete and steel were often considered [1]. In some studies [2-4], the decrease of the compressive strength of the cracked concrete caused by the steel corrosion was also taken into account to better simulate the structural response. Recently, Kioumarsi et al. [5-6] performed a detailed 3D non-linear finite element simulation of the residual flexural capacity of corroded RC beam. In their work, the damage induced by the steel corrosion was simulated by reducing the cross section, reducing the yield and ultimate strength of the rebars, decreasing the bond strength and modifying the bond-slip behaviour between concrete and steel, and reducing the strength of cracked concrete.

Until now, only very limited work on the numerical simulation of corroded RC columns under axial compression has been carried out, despite that the corrosion of the reinforcing steel can have a profound influence on the stiffness and the load carrying capacity of RC columns [7-8]. It is thus of crucial importance to accurately predict the real behaviour of axially loaded RC columns affected by steel corrosion. Finozzi and Saetta [9] reported such a numerical simulation using a two-dimensional (2D) numerical model based on damage mechanics. The predicted failure loads for the columns were in good agreement with the test data; however, the depicted stiffness and deformation behaviour of the columns are less satisfactory. This has motivated the authors of this paper to carry out the study in the present paper.

In this paper, a three dimensional (3D) numerical model incorporating a sophisticated material model for concrete is developed to simulate the structural performance of corroded RC columns.

6.   ANALYTICAL OBJECTS

Based on the related experimental evidences [7-8], the following effects need to be taken into account in the analysis of axially compressed RC columns affected by steel corrosion:
  – The loss of the steel cross section;
  – The cracking and spalling of the cover concrete;
  – The reduction of the confinement provided by the transverse steel to the core concrete;
  – The premature buckling of the longitudinal rebars; and
  – The increase of the load eccentricity.

Rodríguez et al. [8] tested a total of 24 RC columns to investigate the impact of the steel corrosion on the response of RC columns. In the present work, two columns tested by Rodríguez et al. [8] are simulated. They are column No. 28 with corroded steel rebars and column No. 22 without any corrosion as a reference column. The columns had a 200×200 mm^2 cross section and a height of 2000 mm. The longitudinal rebars were 4 Φ16 and the transverse rebars were Φ6 (spacing s = 150 mm).The compressive strength of the concrete were 34.0 MPa and 35.6 MPa in the non-corroded and corroded columns, respectively. The yield strengths of the longitudinal and transverse rebars were in the range of 550 – 590 MPa. The chloride attack penetration depth in the corroded longitudinal rebars was 0.63 mm while it was 0.50 mm in the transverse rebars (maximum value of 4.7 mm). The reference column failed at a load of 1702 kN while the failure load of the corroded column was 997 kN, which is about 51% lower than that of the reference column. As mentioned above, the two columns were also simulated by Finozzi and Saetta [9] using a 2D numerical model based on damage mechanics.

7. MODELLING DETAILS

7.1 Material model for concrete

In numerical analysis of RC structures, the modelling of concrete has always been a challenging issue due to the complexity of its material behaviour. To simulate the complex behaviour of the concrete in RC columns under axial compression, a triaxial constitutive model is necessary. In this study, the microplane model M4L for concrete, which was developed in [10-11] recently, is employed to simulate both the column core concrete and the column cover concrete. The model M4L is a macroscopic material model for concrete, which represents a refinement of the previous model M4 [12-13]. In the model M4L for concrete, the constitutive properties of the material are characterized by a relation between the stress and strain components on the mesolevel. The stress-strain relations are defined not in terms of the macrolevel continuum tensors, but in terms of the stress and strain vectors on planes of all possible orientations within the material, which are called microplanes. Through comparing the model predictions with a broad range of test data in literature, the model M4L has been proven to be able to realistically simulate the uni-, bi- and triaxial material behaviour of concrete. More details about the performance of the model and the comparisons with the test data can be found in [11].

The model M4L uses a set of parameters to simulate the mechanical behaviour of concrete subjected to various stress states. These parameters include the modulus of elasticity E_c, the Poisson's ratio v and two groups of microplane parameters, namely k_1 - k_4 and c_1 - c_{27}. The k- and c- parameters are connected to the microplanes, thus they have generally no direct macroscopic physical meanings. The microplane parameters can be identified through numerical fitting of material test data. Numerical experiments [11, 14] indicated that the c- parameters can generally be fixed for all normal concretes. Their reference values are given in [11]. These values for the c- parameters are used in the present work. However, the k- parameters have to be calibrated according to the specified concrete.

However, due to the fact that the microplane constitutive laws on individual microplanes are generally simple one-to-one relations, the fitting of the microplane parameters is possible by using test data for simple stress states, such as unconfined uniaxial compression test, hydrostatic compression test and high confinement compression test. In most cases, only the unconfined uniaxial compression test data is adequate for determining the model parameters.

For the core and the cover concretes in the non-corroded column as well as the core concrete in the corroded column, the model parameters can be easily determined on the basis of the assumed unconfined compression behaviour. It should be noted that the same set of parameters are used for the core and the cover concretes in the non-corroded column, namely,

$E_c = 26165$ MPa, $v = 0.20$, $k_1 = 1.12 \times 10^{-4}$, $k_2 = 1000$, $k_3 = 16$, $k_4 = 15$.

For the core concrete in the corroded column, the used model parameters are:

$E_c = 26774$ MPa, $v = 0.20$, $k_1 = 1.14 \times 10^{-4}$, $k_2 = 1000$, $k_3 = 16$, $k_4 = 15$.

In the corroded RC column, the corrosion of the reinforcing rebars causes longitudinal cracking in the cover concrete. This cracking reduces the compressive strength of the concrete and needs to be taken into account in numerical simulation. In this paper, the proposal by Coronelli and Gambarova [2] is adopted. In this method, the compressive strength of the (cracked) cover concrete is computed as:

$$f_c^* = \frac{f_c}{1 + k \dfrac{\varepsilon_1}{\varepsilon_{c0}}} \tag{1}$$

in which k is a coefficient depending on the bar roughness and diameter, typically $k = 0.1$; ε_{c0} is the strain at the peak compressive stress (strength) f_c; ε_1 is the average tensile strain in the cracked concrete. More details about the determination of the compressive strength of the cracked concrete can be found in Coronelli and Gambarova [2].

Based on the estimated compressive strength of the cracked cover concrete according to Equation (1), the model parameters for the (cracked) cover concrete in the corroded column are determined as:

$E_c = 15032$ MPa, $v = 0.20$, $k_1 = 0.66 \times 10^{-4}$, $k_2 = 1000$, $k_3 = 16$, $k_4 = 15$.

3.2 Material model for reinforcing steel

The stress-strain behaviour of the non-corroded reinforcing steels is simulated by a linear elastic-perfect plastic material model, which is described by the modulus of elasticity E_s and the yield strength f_y of the material.

For the corroded rebars, the loss of the cross section and/or the mechanical properties needs be taken into account in the numerical model. In addition, the premature buckling of the longitudinal rebar and the break of the transverse rebar, as observed in the test [8], should also be considered. In this paper, a bilinear constitutive model is adopted to describe the premature buckling of the corroded longitudinal rebar:

$$\sigma_s = \begin{cases} E_0 \varepsilon_s & (0 \le \varepsilon_s \le \varepsilon_{crit}) \\ E_n \varepsilon_s & (\varepsilon_s > \varepsilon_{crit}) \end{cases} \tag{2}$$

where, ε_{crit} is the steel strain corresponding to the critical stress σ_{crit}, which is calculated as [8]:

$$\sigma_{crit} = \frac{\pi^2 E_s (0.25D)^2}{(0.75L^2)} \tag{3}$$

where, D is the diameter of the corroded longitudinal rebars while L is the buckling length of the transverse rebars, which is assumed to be $L = 3s$ (transverse rebar spacing) since it was detected in the test [8] that 4 transverse rebars were broken. E_n is the slope of the softening branch, which is determined as in [9].

The corroded transverse reinforcing steel is simulated with a linear elastic – plastic material model with limited ductility. The reduced ultimate strain of the steel due to the corrosion is described according to Du et al. [15-16].

3.3 Modelling of reduced cross section of corroded reinforcements

It was observed in the test [8] that the longitudinal rebars in the corroded columns mainly underwent uniform corrosion; while the transverse rebars exhibited both uniform and profound localised (pitting) corrosion with a higher damage level. Based on these observations, the residual cross section of the corroded longitudinal rebar is calculated as:

$$A_{sl} = \frac{\pi}{4} (D_0 - 2\chi)^2 \tag{4}$$

in which, D_0 is the initial diameter of the reinforcement; χ is the depth of corrosion (mm).

The residual cross section area of the corroded transverse reinforcement is computed as [9]:

$$A_{st} = \frac{\pi}{4} D_0^2 - \frac{\pi}{4} (2D_0\chi - \chi^2) \tag{5}$$

(a) *Cover and core concrete*   (b) *Longitudinal and transverse reinforcements*
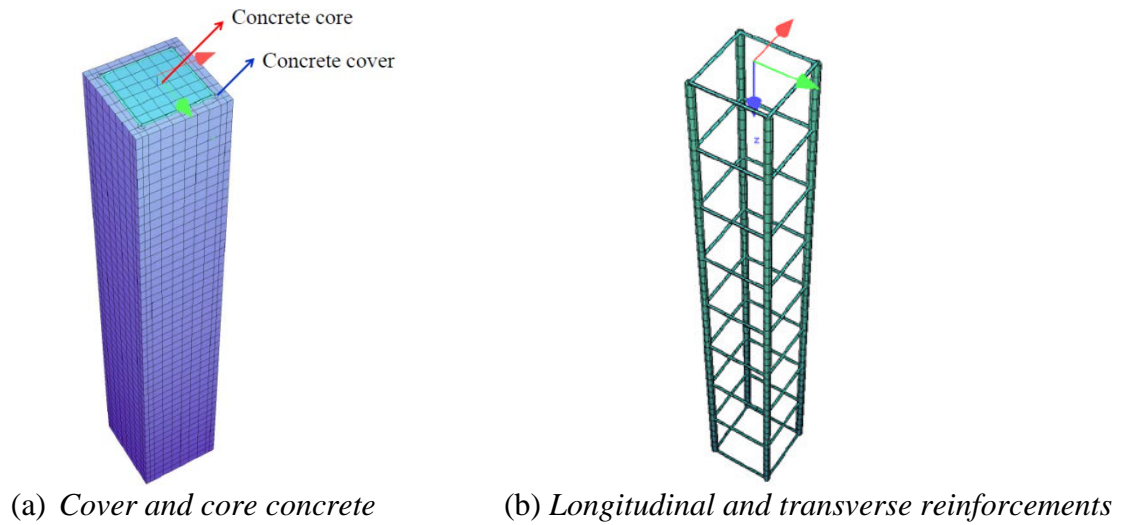
Figure 1 – Finite element mesh of the columns

3.4   Finite element types and meshes

Both the column core and cover concretes are discretised into 8-node brick elements with $2 \times 2 \times 2$ integration points. The reinforcing steels are simulated with 2-node truss elements. Since the columns were subjected to axial compression, no slip between the concrete and reinforcements is assumed. The 3D finite element mesh of the column is illustrated in Figure 1. To facilitate the comparison, the same mesh is used for both the non-corroded and corroded columns. The general crack band model is used to minimize the mesh sensitivity. A uniform displacement is applied on the column top to simulate the axial loading. The increased eccentricity due to the asymmetric damage of the cover concrete is ignored since the selected columns had minimal eccentricity.

8.   NUMERICAL RESULTS AND DISCUSSIONS

Figure 2 shows the simulated load – average strain curve of the column No. 22. It can be seen from the figure that the simulations are very close to the test data, both for the stiffness and the ultimate load. This implies that the model M4L is able to realistically capture the complex behaviour of the concrete in the column.
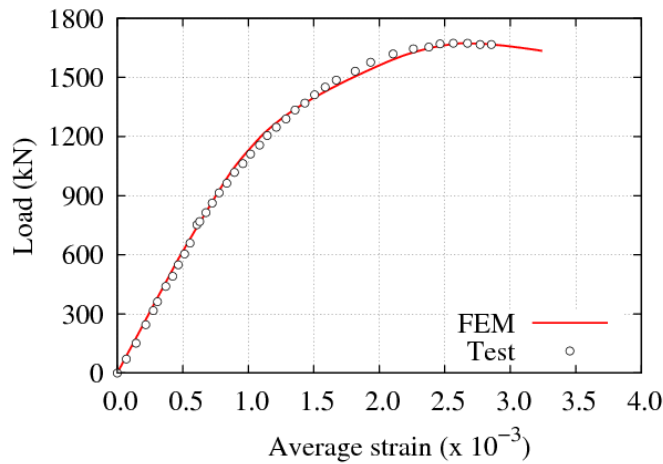
Figure 2 – Load –average strain curve of non-corroded column No.22

A comparison of the predicted load – average curves with the test data for the corroded column No.28 is shown in Figure 3. Two simulation results are shown in the figure: one considers the premature buckling of the longitudinal reinforcement while the other ignores the buckling of the longitudinal rebar (the rebar is modelled as a linear elastic-perfect plastic material). It can be seen that when the premature buckling behaviour of the longitudinal rebar is considered, the numerical predictions are fairly consistent with the test data; while the ignorance of this behaviour results in an overestimation of the maximum load and the post-peak ductility of the column. This indicates that it is necessary to take into account the premature buckling of the longitudinal rebar in numerical simulation of corroded RC columns under axial compression.
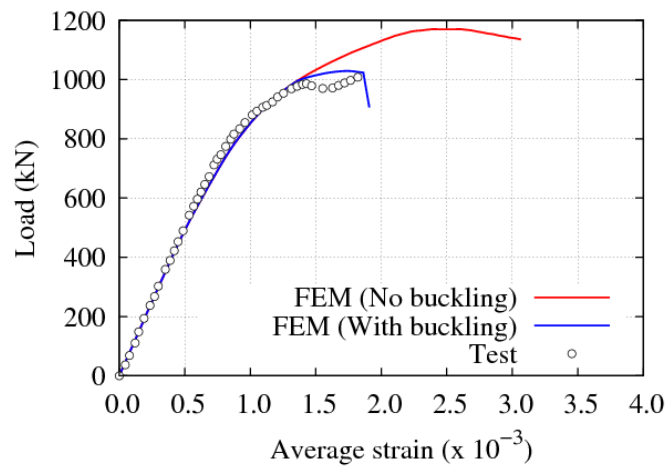
Figure 3 – Load –average strain curve of corroded column No.28

9. CONCLUSIONS AND REMARKS

This paper presents a numerical simulation of non-corroded and corroded RC columns under axial compression by virtue of nonlinear FEM. This work leads to the following conclusions:

- The adopted microplane model M4L is able to realistically capture the behaviour of the concrete in RC columns subjected to axial compression;
- The behaviour of the axially compressed RC column with corroded reinforcing steel can be simulated with adequate accuracy through properly taking into account the cracking and spalling in the concrete cover, the loss of cross section and the reduction of mechanical properties of the transverse rebar, as well as the premature buckling behaviour of the longitudinal rebar;
- An ignorance of the premature buckling of the longitudinal rebar overestimates the ultimate load and the post-peak ductility of the corroded RC column;
- Although the numerical model developed in this paper yields satisfactory simulations of the global load-strain (deformation) response of the corroded column, it should be noted that this model is not adequate for a realistic simulation of the occurrence of the spalling and the delamination of the cover concrete;
- The numerical model for corroded RC columns developed in this paper can be used to quantitatively assess the effect of each individual damage due to the corrosion, such as the corrosion in the reinforcing steel rebars, the premature buckling of the longitudinal rebars, the cracking and spalling of the cover concrete on the structural behaviour of RC columns, which helps to better understand the effect of the corrosion damage on the response of this kind of elements.

REFERENCES

25. Horrigmoe G & Sand B: "Residual Strength of Deteriorated and Retrofitted Concrete Structures: A Numerical Approach," Proceedings, IABSE Symposium, 2002, pp. 39-50.

26. Coronelli D & Gambarova P: "Structural Assessment of Corroded Reinforced Concrete Beams: modeling Guidelines," *ASCE – Journal of Structural Engineering*, Vol. 130, No. 8, 2004, pp. 1214-1224.

27. Kallias A N & Rafiq M I: "Finite element investigation of the structural response of corroded RC beams," *Engineering Structures*, Vol. 32, No. 9, 2010, pp. 2984-2994.

28. Hanjari K Z, Kettil P, Lundgren K: "Analysis of Mechanical Behavior Corroded Reinforced Concrete Structures," *ACI Structural Journal*, Vol. 108, No. 5, 2011, pp. 532-541.

29. Kioumarsi M M, Hendriks M A, Geiker M R, "Quantification of the Interference of Localised Corrosion on Adjacent Reinforcement Bars in a Concrete Beam in Bending," *Nordic Concrete Research*, Vol. 49, 2014, pp. 39-57.

30. Kioumarsi M M, Hendriks M A N, Kohler J, Geiker M R: "The Effect of Interference of Corrosion Pits on the Failure Probability of a Reinforced Concrete Beam," *Engineering Structures*, Vol. 114, 2016, pp. 113-121.

31. Uomoto T & Misra S: "Behavior of Concrete Beams and Columns in Marine Environment when Corrosion of Reinforcing Bars Take Place," *ACI Special Publication*, Vol. 129, 1988, pp. 127-146.

32. Rodríguez J, Ortega L M, Casal J: "Load Bearing Capacity of Concrete Columns with Corroded Reinforcement," Proceedings, Fourth International Symposium on Corrosion of Reinforcement in Concrete Construction, 1996, pp. 220-230.

33. Finozzi I & Saetta A: "Damage Model for the Analysis of Structural Response of RC Columns Subjected to Corrosion Phenomena," Proceedings, International Conference on Concrete Solutions, Queen's University Belfast, 2014, pp. 793-800.

34. Tue N V, Li J, Caner F C: "Microplane Constitutive Model M4L for Concrete. I: Theory," *Computers & Structures*, Vol. 128, 2013, pp. 219-229.

35. Li J, Tue N V, Caner, F C: "Microplane Constitutive Model M4L for Concrete. II: Calibration and validation," *Computers & Structures*, Vol. 128, 2013, pp. 146-159.

36. Bažant Z P, Caner F C, Carol I, Adley M D, Akers S A: "Microplane Model M4 for Concrete. I: Formulation with Work-Conjugate Deviatoric Stress," *ASCE – Journal of Engineering Mechanics*, Vol. 126, No. 9, 2000, pp. 944-953.

37. Caner F C, & Bažant Z P: "Microplane Model M4 for Concrete. II: Algorithm and Calibration," *ASCE – Journal of Engineering Mechanics*, Vol. 126, No. 9, 2000, pp. 954-961.

38. Li J: "Development and Validation of a New Material Model for Concrete on the Basis of Microplane Theory," Graz University of Technology Press, 2012.

39. Du Y G, Clark L A, Chen A H C: "Residual Capacity of Corroded Reinforcing Bars," *Magazine of Concrete Research*, Vol. 57, No. 3, 2005, pp. 135-147.

40. Du Y G, Clark L A, Chen A H C: "Effect of Corrosion on Ductility of Reinforcing Bars," *Magazine of Concrete Research*, Vol. 57, No. 7, 2005, pp. 407-419.

Screening of Low Clinker Binders, Compressive Strength and Chloride Ingress

Mette Rica Geiker, M.Sc., Ph.D.
Professor, Department of Structural Engineering, Norwegian University of Science and Technology, NO-7491 Trondheim, Norway
Visiting Professor, Department of Civil Engineering, Technical University of Denmark, Brovej 118, DK-2800 Kgs. Lyngby, Denmark
e-mail: mette.geiker@ntnu.no

Klaartje De Weerdt
M.Sc., Ph.D., Associate Professor
Department of Structural Engineering, Norwegian University of Science and Technology
NO-7491 Trondheim, Norway
e-mail: klaarte.d.weerdt@ntnu.no

Sergio Ferreiro Garzón
M.Sc., Ph. D., Chemical Engineer
Research and Development Center, Cementir Holding S.p.A.
Aalborg Portland, 9220 Aalborg, Denmark
e-mail: sergio.f.garzon@aalborgportland.com

Mads Mønster Jensen
M.Sc., Ph.D.
Department of Civil Engineering, Technical University of Denmark
Brovej 118, DK-2800 Kgs. Lyngby, Denmark
e-mail: mmoj@byg.dtu.dk

Björn Johannesson
M.Sc., Ph.D., Professor
Department of Building Technology, Linnæus University
e-mail: bjorn.johannesson@lnu.se

Alexander Michel
M.Sc., M.Sc., Ph.D., Assistant Professor
Department of Civil Engineering, Technical University of Denmark
Brovej 118, DK-2800 Kgs. Lyngby, Denmark
e-mail: almic@byg.dtu.dk

ABSTRACT

This paper reports an initial screening of potential new binders for concrete with reduced CO_2-emission. Mortars cured saturated for 90 days are compared with regard to a) compressive strength of mortars with similar water-to-binder ratio, and b) chloride ingress in similar design strength mortars exposed to seawater. The reference used was a binder composition typical for a Danish ready mixed concrete for aggressive environments and strength class C35/45. Based on the present investigation and assumptions up to around 15% reduction in CO_2 emission from binder production might be obtained without compromising the 90 days compressive strength and resistance to chloride ingress in marine exposure by using selected alternative binders.

Key words: Cement, chlorides, CO_2-emission, supplementary cementitious materials (SCM).

1.   INTRODUCTION

Despite continuous improvements in the cement industry, e.g. [1], the CO_2 emissions has been increasing due to the growth in cement demand in the developing countries, and the share of cement production is now estimated to be around 6-10% of the total anthropogenic greenhouse gases [2].

A recent report on potential, economically viable solutions for a low-CO_2 cement based materials industry identified two main areas delivering substantial additional reductions in global CO_2 emissions related to production and use of cement and concrete: a) increased use of low-CO_2 supplementary cementitious materials (SCMs) as partial replacement of Portland cement clinker and b) more efficient use of Portland cement clinker [2].

In order to create substantial reduction in CO_2 emission, the concrete types with the highest sales volumes should be the target, rather than tailored cements and concretes for special applications. Ready-Mixed Concrete (RMC) has been the main concrete product within the last decade [3], consuming around 50% of the total cement produced in Europe (Fig. 1).

Similar RMC production-to-cement consumption ratios are observed in the Nordic countries, with the exception of Norway where around 70% of the total cement produced is used for RMC. Compared to Finland and Denmark RMC produced in Norway and Sweden generally contains lower additional amounts of siliceous fly ash added at the concrete plant on top of cement. Lower quantities of fly ash added at the concrete plant in Norway and Sweden are due to noticeable greater demand of RMC with the highest strength class (Fig. 2) than in Denmark or Finland, but also because some of the cement types employed in RMC production in Norway already contain large amounts of fly ash on their own (CEM II type). Fig. 2 also shows that the most used strength classes for RMC production in the EU and average of Nordic countries are the intermediates: C25/30 and C30/37 [3].

Particularly in Denmark, most of RMC plants produce different concrete strength classes by mixing CEM I type cements with varying fly ash content (and water-to-binder ratio), consuming around 60-70% of the total Aalborg Portland grey cement production along with other imported cements supplied by non-national producers. The most often manufactured RMC strength class for aggressive environments is C35/45, and the typical concrete is made with a binder composition of 83% of CEM I type cement and 17% of siliceous fly ash.
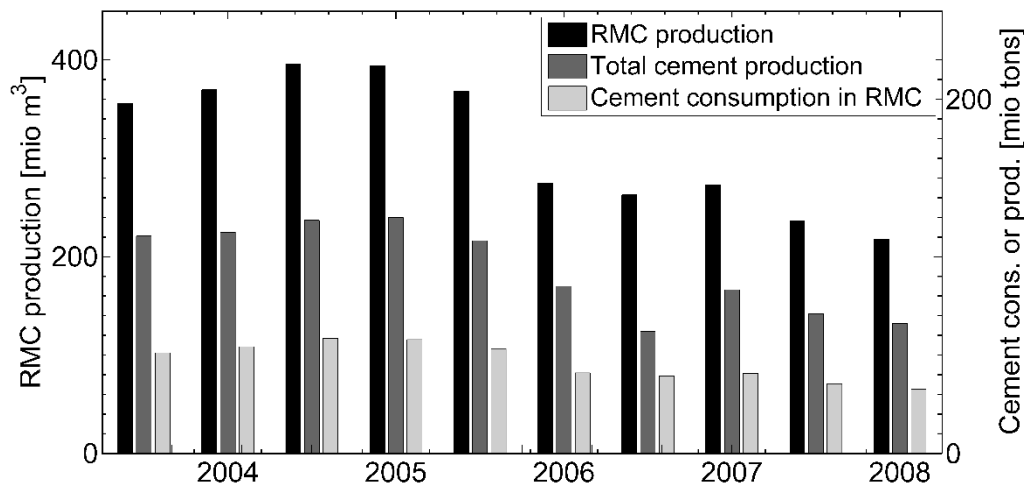
Figure 1 - RMC production (left hand scale); cement consumption and production (right hand scale) in EU from 2004 to 2013 [3].
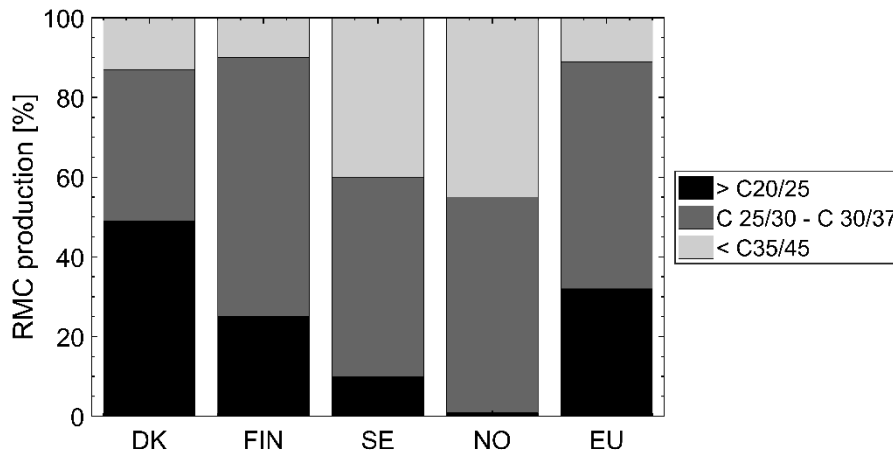

Figure 2 - RMC production by strength class in Nordic countries and EU in 2012 [3].

Regarding possible improvements in cement production, the use of alternative fuels as biomass or waste materials has ecological and economic benefits, such as conserving non-renewable resources. Waste combusted in the cement kiln systems as opposed to dedicated incinerators result in net global reduction in CO_2 emissions and lower CO_2 penalties [4]. However, the use of alternative fuels may result in kiln dust with higher chloride content than other sources. Consequently, the use of kiln dust as limestone filler for production of blended cements type CEM II/A-LL may be constrained by the maximum chloride content in cement (0.10%wt) prescribed in EN 197-1 [5].

Concerning cement and concrete composition, two separate or combined strategies to produce potentially greener concrete by lowering clinker content can be used: partial replacement of the clinker in cement by SCMs according to EN 197-1 [5] and/or partial replacement of the cement in the concrete by mineral additions such as silica fume, siliceous fly ash and/or limestone as described in e.g. the NADs to EN206. The concrete standards differ between countries with regard to the required cement types and strength classes, maximum water-to-cement ratios and minimum cement contents, and the allowed types of mineral additions and cement-to-addition ratios. This introduces large variations in concrete compositions between countries.

This paper reports an initial screening of potential new binders for concrete with reduced CO_2-emission. The objectives of the paper are to compare low clinker binders with regard to

- the compressive strength of mortars with similar water-to-binder ratio
- the chloride ingress in similar strength mortars exposed to seawater
- the CO_2-emission from production of the binders.

The materials investigated include a) a new clinker optimized for facilitating clinker grinding and pozzolanic reactions of supplementary cementitious materials (SCMs) and b) selected SCMs: burnt shale, calcined clay, limestone filler with low and high chloride content, and siliceous fly ash.

2. EXPERIMENTAL

2.1 Constituent materials

The chemical compositions determined by X-ray fluorescence (XRF) of the current clinker (K1), the new highly mineralized clinker (K2) and the other binder constituents are summarized in Table 1. The burnt shale (T) sample was supplied by Eesti Energia AS from Estonia, and the clay (Q) was calcined at FLSmidth as part of another project ("SCM project"). All other materials were supplied by Cementir Holding - Aalborg Portland including two limestone fillers (LL) differing in chloride content and a fly ash (V).

The calculated mineralogical composition of the clinkers and the compressive strength development measured according to EN 197-1 [5] are given in Table 2 and Table 3, respectively.

Table 1 - Chemical composition (%wt), density and Blaine fineness of binder constituents. Two batches of LL with different chloride content were used.

Method	Property	unit	K1	K2	LL	Q	T	V
XRF	SiO_2	%	20.2	19.5	12.7	62.5	34.2	55.0
XRF	Al_2O_3	%	5.5	6.1	3.6	16.6	8.2	19.9
XRF	Fe_2O_3	%	4.0	3.3	1.8	9.4	4.8	5.5
XRF	CaO	%	65.4	66.0	44.0	0.8	30.1	4.5
XRF	MgO	%	0.80	0.92	0.60	2.95	5.59	1.81
XRF	K_2O	%	0.54	0.52	0.58	2.82	4.38	2.16
XRF	Na_2O	%	0.21	0.25	0.23	1.95	0.11	1.12
XRF	SO_3	%	1.5	1.6	0.4	0.4	5.6	0.4
XRF	Cl	%	0.03	0.00	0.21/-	0.03	0.29	0.00
EN 196-2 [6]	LOI	%	0.24	0.47	35	2.39	4.55	3.2
EN 196-6 [7]	Density	kg/m^3	3170	3180	2710	2430	2790	2300
EN 196-6 [7]	Blaine fineness	m^2/kg	390	330	1262	-	432	345
EN 196-6 [7]	20 μm residue	%	-	-	-	10.5	-	-
EN 196-2 [7]	Cl	%	0.02	0.01	0.14/0.48	0.01	0.30	0.02

Table 2 - Mineralogical composition of clinkers (%wt).

Clinker minerals	K1	K2
C_3S	65.8	70.1
C_2S	8.2	3.1
C_3A	7.9	10.4
C_4AF	12.1	10.1

Table 3 – Compressive strength development (MPa) of clinkers (+ hemihydrate) measured according to EN 196-1 (normalised to 2% air).

Age	K1		K2	
(d)	Mean	SD	Mean	SD
1	22.0	0.2	-	-
2	32.9	0.3	36.6	0.6
7	50.5	1.4	55.9	1.3
28	64.6	1.4	65.0	1.4
91	-	-	71.8	1.1

The composition of the new clinker was selected to maximize the C_3S content for rapid strength development and rapid release of $Ca(OH)_2$ to enhance pozzolanic reactions. The optimized C_3S content of the new clinker resulted in an equivalent 28 days strength for a Blaine of 330 m^2/kg compared to current clinker ground at fineness around 390 m^2/kg. Low fineness of the ground clinker is recommended for manufacturing of blended cements with a high substitution level of finely ground SCMs to reduce water demand and improve workability.

The burnt shale is called CFB and collected at the 1st electrostatic precipitator of Eesti Power plant [8] and contains some phases that may affect the reactions of mortars, such as lime, portlandite, anhydrite, periclase and some clinker phases.

The dried raw clay containing around ¾ by wt. of clay minerals, mainly montmorrilonite but also illite, along with other minerals such as quartz, feldspar and phyllosilicates [9], was calcined in a flash calciner [10] at 850°C and subsequently, finely ground to maximize pozzolanic reactivity of calcined clay (Q) within 28 days [9].

Table 4 - Binder compositions in (%wt) and CO_2 emission from binder production. H: hemihydrate; for remaining abbreviations please see the text.

id	K1	K2	H	LL high Cl	LL low Cl	T	Q	V	SO_3	Cl	CO_2 (t/t binder)
R1	76.7		2.6	4.0				16.7	3.30	0.04	0.65
B1		76.5	2.8	4.0				16.7	3.33	0.03	0.65
B2		63.7	2.3		15.8			18.2	2.82	0.03	0.56
B3		63.7	2.3	15.8				18.2	2.82	0.09	0.56
B4		63.7	1.5	7.9		7.9		19.0	2.82	0.07	0.55
B5		63.7	1.1	4.0		11.9		19.4	2.82	0.06	0.55
B6		63.7	2.3		34.0				2.31	0.05	0.58
B7		63.7	2.3	8.5			25.5		2.31	0.05	0.62
B8		63.7	2.3				34.0		2.31	0.01	0.63
B9		58.9	2.2	15.7			15.7	7.5	2.31	0.09	0.56

Binder B1 was used to compare chloride ingress resistance of the new clinker (K2) and the current clinker (K1) in the presence of siliceous fly ash (V), i.e. (B1 vs R1).

The binder compositions given in Table 4 were selected to illustrate the either separate or combined effect of the new clinker, chloride content, SCM type, and clinker replacement on the resistance to chloride ingress and the potential reduction in CO_2 emissions compared to a typical binder composition presently used in ready mixed concrete (RMC) production in Denmark (R1).

Two batches of limestone filler (LL) differing in chloride content (0.14 and 0.48%) were used in binders B2 and B3 to illustrate the potential impact of initial chloride content on chloride ingress. The binder compositions corresponded to cement type CEM II/A-LL for the maximum allowed clinker replacement by limestone filler, i.e. 20% and addition of siliceous fly ash (V) on top to achieve 35% total clinker replacement in binder, both calculated in accordance with EN 197-1 [5] (i.e. omitting $CaSO_4$). Clinker replacement was calculated similarly for all binders. Table 4 gives the actual clinker replacement.

As shown in Table 4, except for binder B6, the remaining LL-containing binders contain LL with high chloride content. This is to illustrate to potential impact of increased use of alternative fuels for clinker production on the resulting limestone fillers. To meet the requirement to chloride content, Cl ≤ 0.10% according to EN 197-1 [5], binder B6 was prepared with the LL with low chloride content.

Binders B3, B4 and B5 were included to investigate the performance of burnt shale in cement type CEM II/A-M (T-LL). The binders contained 20% of combinations of burnt shale (T) and limestone filler (LL) with three different ratios, expressed as T/(T+LL) = 0, 0.5 and 0.75. Siliceous fly ash (V) was added to achieve 35% clinker replacement in the binder resulting in (T+V)/(T+V+LL) = 0.53, 0.77 and 0.89.

Binders B6, B7 and B8 were included to investigate the performance of cement types CEM II/B-M (Q-LL) without any addition of siliceous fly ash (V), but containing 35% of combinations of calcined clay (Q) and limestone filler (LL) in three different ratios, expressed as Q/(Q+LL) = 0, 0.75 and 1. Binder B9 aimed to show the effect of further clinker reduction (to 60% of binder) by addition of siliceous fly ash (V) to a CEM II/B-M (Q-LL) type cement with 35% clinker replacement and a ratio of Q/(Q+LL) = 0.5 resulting in (Q+V)/(Q+V+LL) = 0.60.

Finely ground calcium sulphate hemihydrate (hemihydrate, H) with a SO_3 content of 56.3% (measured according to EN 196-2) was included in all binders to control early hydration. The optimum SO_3 content for reference binder (B2) containing only the new clinker (K2) and hemihydrate was determined to 3.5%. The hemihydrate content in other binders was reduced according to the clinker content. For the binders with burnt shale (B4 and B5) the hemihydrate content was further reduced to compensate for SO_3 content of the burnt shale.

The binders were mixed with CEN Standard sand and demineralised water. In addition polycarboxylate ether based superplasticizer (SP), manufactured by BASF with a solid residue of 20% was added to some of the mortars. The density of CEN Standard sand and SP was 2650 kg/m^3 and 1100 kg/m^3, respectively.

2.2 Series 1, constant w/b

A first series of mortars were mixed and cured according to EN 196-1 [11] (water-to-binder ratios, w/b=0.5) to determine compressive strength at 90 days. Although 28 day strength is the most relevant strength parameter for RMC producers at present due to current standards, a curing time of 90 days was selected to enable the SCMs to react further. The mortar compositions are summarized in Table 5. Polycarboxylate ether based superplasticizer (SP) was added to mortars containing either burnt shale or calcined clay in order to achieve similar and comparable flow to R1. Liquid and solid fractions of the SP were considered as part of water and binder, respectively.

Table 5 – Series 1: Composition, flow, air content, and 90 day compressive strength of mortar measured as in accordance with EN 196-1 (w/b/s=1/2/6 by mass)

Mortar ID	Binder	SP	Water	Sand	Flow	Air content	90 day strength (MPa)		CO_2 reduction
	(g)	(g)	(g)	(g)	(cm)	(%vol)	mean	SD	(%)
R1	450.0		225.0	1350	23.3	0.2	73.9	0.9	-
B1	450.0		225.0	1350	22.8	0.9	70.7	2.4	0
B2	450.0		225.0	1350	21.9	1.1	64.8	1.5	15
B3	450.0		225.0	1350	21.7	1.3	66.5	1.1	15
B4	449.9	0.71	224.4	1350	22.7	1.0	70.3	0.7	16
B5	449.8	1.07	224.1	1350	22.9	0.5	70.9	2.2	17
B6	450.0		225.0	1350	20.1	2.7	56.3	1.3	12
B7	449.8	1.15	224.1	1350	20.6	2.1	78.8	2.7	6
B8	449.7	1.53	223.8	1350	20.4	2.7	69.5	0.9	3
B9	449.9	0.53	224.6	1350	20.9	1.8	72.7	1.6	15

The air content of mortars was determined in accordance with [12] on the basis of the density of theoretically air void free mortar and the weight at demoulding. The compressive strength was normalized to an air content of 2 vol % using Bolomey's equation, e.g. [12].

The mortar mixing procedure was amended from EN 196-1 [11] to include one step for a delayed addition of the superplasticizer. Cement and at least 85% of total mixing water were placed into the bowl of a Hobart mixer and mixed for 30 s at the low speed. After these 30 s of mixing, sand was steadily added during the next 30 s and mixing was continued. After 90 s, superplasticizer diluted in remaining mixing water was added to mortar and mixing was continued for an additional 30 s at low speed. Then, mixer was switched to the high speed and mixing lasted for another 30 s. Afterwards, the mixer was stopped for 90 s. During the first 30 s, mortar adhering to the wall and bottom part of the bowl was removed and placed in the middle by means of a rubber scraper. Finally, mixing was continued at high speed for 60 s.

2.3   Series 2, similar 90 day compressive strength

Based on Series 1, new water-to-binder ratios were estimated in accordance with Bolomey's equation [13] to result in 90 day compressive strength equivalent to R1 and constant paste volume. The expected equivalent strengths were, however, not experimentally verified. The compositions of the mortars used for Series 2 are summarized in Table 6. Different dosages of SP were added to mortars in order to achieve comparable flow to the reference (R1). Liquid and solid fractions of the SP were again considered as a part of water and binder, respectively.

The second series of mortars were mixed as Series 1. The mortar samples were cast, cured, exposed and analysed according to procedures reported recently [14]. The mortars were cast in 125 ml plastic bottles (ø 50.5 mm). A small amount of water was added on top of the mortar to ensure saturated conditions. After 90 days curing, approximately 5 mm was cut from the bottom surface and the remaining surfaces were sealed by epoxy. The samples were re-saturated and finally exposed to artificial seawater with a composition according to ASTM D1141-3 [15]. Twelve samples were submerged in 2.5 L. The exposure solution was exchanged after 14 and 28 days and thereafter every 30 days. After 90, 180 and 270 days of exposure, chloride ingress was determined by profile grinding and titration.

Table 6 – Series 2: Mortar compositions (adjusted to same compressive strength; paste/sand = 376/509 by volume) and CO_2 emission from binder production. The calculated CO_2 reductions combine the impact of binder composition and w/b.

id	Binder (g)	SP (g)	Water (g)	Sand (g)	w/b (-)	Cl (%wt)	CO_2 reduction (%)
R1	450.0		225.0	1350	0.50	0.009	-
B1	452.6		224.5	1350	0.50	0.007	0
B2	464.2	1.02	216.3	1350	0.47	0.007	13
B3	456.8	0.59	219.2	1350	0.48	0.020	14
B4	448.8	0.83	222.0	1350	0.50	0.016	17
B5	451.7	1.35	220.7	1350	0.49	0.013	17
R6	482.9	1.79	213.3	1350	0.44	0.012	6
B7	416.7	0.45	233.1	1350	0.56	0.010	13
B8	434.2	2.37	224.2	1350	0.52	0.002	7
B9	433.6	0.38	226.2	1350	0.52	0.019	18

1.3 CO_2 emission from binder production

The CO_2 emissions per ton of binder (Table 3) were estimated considering hemihydrate, fly ash and burnt shale as CO_2 neutral, i.e. CO_2/t, and assuming 0.85 t CO_2/t of clinker, 0.1 t CO_2/t of limestone filler, and 0.27 t CO_2/t of calcined clay. The CO_2 reductions were calculated considering the CO_2 emissions from each constituent and the w/b variations.

3   RESULTS AND DISCUSSION

3.1   Compressive strength

The 90 day compressive strength of the mortars with w/b=0.5 (Series 1) normalized to the same air content (and thus differing from Table 5) is illustrated in Fig. 3. The compressive strength of the mortars with the two clinkers (R1 vs B1) are comparable, while some of the SCM types or combinations appear to affect the 90 day compressive strength.

As has been reported earlier, a synergistic effect between alumina containing SCMs and limestone filler (LL) exists (e.g. [9,16]. This is illustrated in Fig. 4 for calcined clay (Q). An optimum composition that maximized the compressive strength at 90 days can be observed. The strength enhancement is attributed to pozzolanic reactions of the calcined clay and synergetic effects between reactive alumina from the clinker and SCM and the $CaCO_3$ from the limestone filler [9]. For binders with calcined clay (Q) (B7, B8, B9) the performance of B7 is significantly better than the reference (R1). (Note that the clinker content is lower further reduced in B9.) No synergetic effect was observed for burnt shale (T).
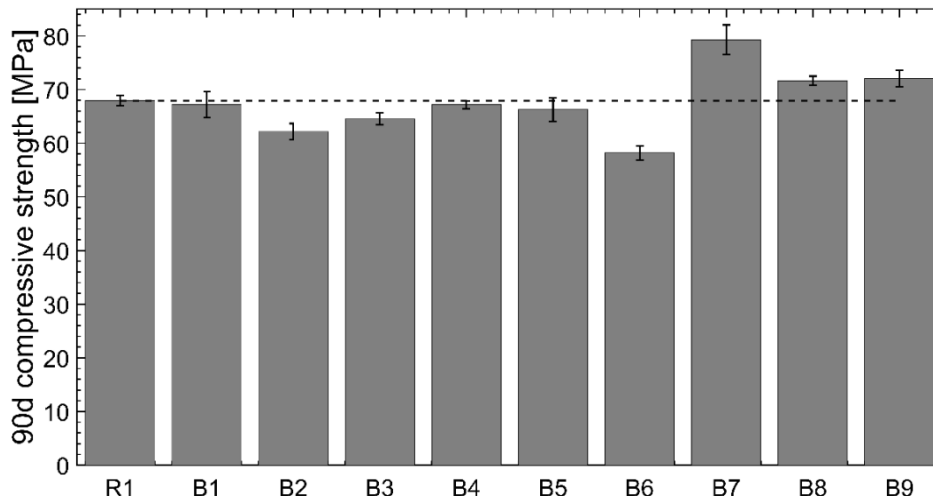
Figure 3 - Series 1: 90 day compressive strength of mortars of (w/b = 0.5), normalized to 2% air content. The dotted line compares to the average compressive strength of B1. The error bars indicate +/- SD.

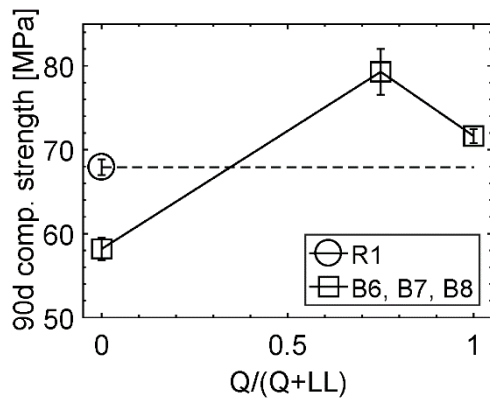*Figure 4 - Synergetic effect between limestone filler (LL) and calcined clay (Q). 90 day compressive strength of mortars of (w/b = 0.5), normalized to 2% air content. The error bars indicate +/- SD.*

The equivalent performance achieved by B9 with 40% clinker replacement by V, Q and LL compared to B6-B8 with 35% clinker replacement by only Q (B8) or Q and LL (B6-B7), indicates that binders containing only 60% of clinker and higher contents of limestone filler than optimum, may still provide sufficient $Ca(OH)_2$ and $CaCO_3$ to enable pozzolanic reaction and synergetic effects between reactive alumina and $CaCO_3$.

3.2. Chloride ingress

Chloride ingress profiles after 90, 180 and 270 days exposure to seawater of mortars with comparable 90 days compressive strength are shown in Fig. 5. To allow for possible use of the data, e.g. for verification of models, the measured data are also given in tabular form (Appendix, Table A1 – Table A3. It should be kept in mind that w/b varies between the mortars; from 0.44 (B6) to 0.56 (B7), ref. Table 6.
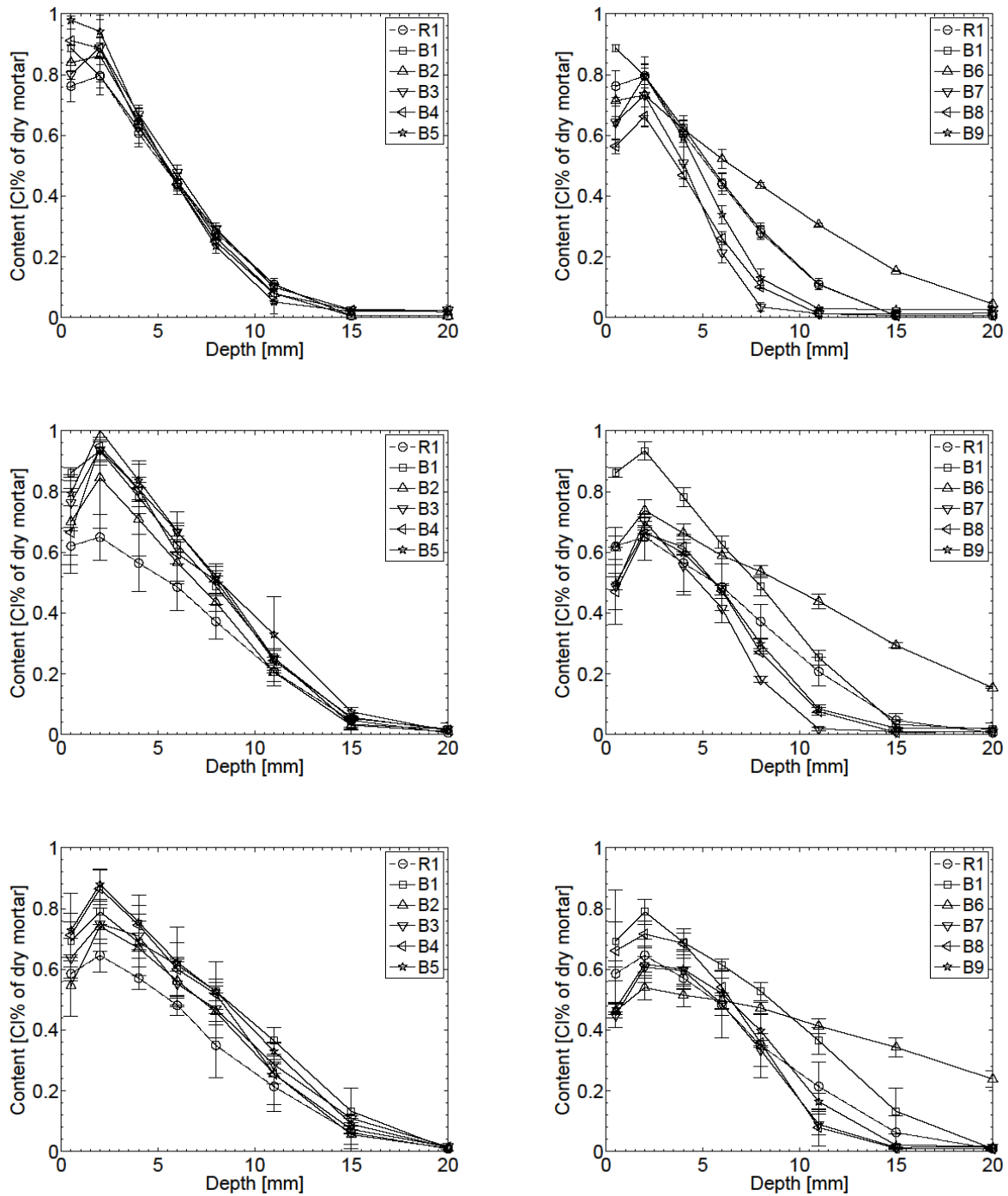
Figure 5 – Chloride profiles after 90 (upper), 180 (middle), and 270 (lower) days exposure to artificial sea water at 20°C. The error bars indicate +/- SD.

The maximum total chloride concentration after 270 days exposure was found at a depth of approximately 2-3 mm for all mortar samples, while a decreased total chloride concentration was observed at the surface. The effect is explained by leaching and other phase changes causing a reduced binding capacity, see e.g. [17,18].

The ingress depths are in general comparable for all binders, except for the binder with 34% limestone filler (B6), which exhibited a very low ingress resistance. Most binders with alternative binder constituents exhibited a higher maximum chloride content, indicating an increased binding capacity compared to the reference blend (R1).

Except at the outer surface, the profiles of mortars with the new and old clinker (B1 vs R1) were similar after 90 days exposure. However, after 180 and 270 days the surface concentration in the mortar with the old clinker (R1) appeared reduced; and, more importantly, the chloride content at deeper depth appeared lower in R1. Furthermore, only mortars with calcined clay (B7-B9) showed lower chloride ingress than the reference mortar (R1). This despite that some of the other mortars had a lower w/b than the reference (R1), see Table 6.

There was no measureable impact of the mortar prepared from the limestone filler with low and high chloride content (B2 vs B3).

The mortars with burnt shale (B4 and B5 vs B3) showed the highest chloride concentrations in the surface near region, indication the highest binding capacity.

The beneficial impact of calcined clay (B7-B9) is illustrated in Fig. 5 (right). The binding capacity for these blends appeared increased while the ingress depth was decreased, compared to the binder with only limestone filler (B6). The observations are in agreement with recent findings; see e.g. [19]. More importantly, the chloride ingress at deeper depth appeared lower than in the reference (R1) – and in the mortar with the new clinker (B1), which was also used for B7 – B9.The beneficial impact of the calcined clay appears to be diminishing with exposure time.

Except for the mortars with limestone filler (B6), all mortars with high substitution rate by alternative binder constituents showed higher resistance to chloride ingress than the mortar with the same (new) clinker and only 16.7% fly ash (V) (B1) after 180 and 270 days exposure. Comparing 90 days ingress data, where B1-B5 show similar chloride profiles, the data indicate prolonged reaction of the alternative binder constituents in these mortars.

Except for the mortars with calcined clay (B7, B8, B9), which within the period of testing showed highest chloride ingress resistance, all mortars with the new clinker showed lower resistance to chloride ingress than the reference mortar (R1). The results indicate that around 15% reduction in CO_2-emission (Table 6) can be obtained by using alternative binders without compromising the resistance to chloride ingress in marine exposure of mortars with similar design compressive strength at 90 days.

4.   CONCLUSIONS

Based on the present investigation and assumptions, up to around 15% reduction in CO_2 emission from binder production might be obtained for selected binders without compromising the 90 days compressive strength and short-term resistance to chloride ingress in marine exposure by using alternative binders instead of a binder composition typical for a Danish ready-mixed concrete for aggressive environments and strength class C35/45. Due to varying degree of reaction at testing the long-term chloride resistance needs to be documented. Other issues to be considered are e.g. carbonation resistance and conditions for reinforcement corrosion.

ACKNOWLEDGEMENTS

REFERENCES

1. Damtoft, J.S., Lukasik, J., Herfort, D., Sorrentino, D., Gartner, E.M., "Sustainable development and climate initiatives Sustainable development and climate change initiatives," *Cement and Concrete Research*, Vol. 38, No. 2, 2008, pp. 115–127.
2. Scrivener, K.L, John, V.M., Gartner, E.M., "Eco-efficient cements. Potential, economically viable solutions for a low-CO_2, cement-based materials industry," United Nations Environment Program, Paris 2016.
3. ERMCO 2016. Annual reports 2004-2013 based on the European ready-mixed concrete industry production data http://www.ermco.eu/publications/statistics/, accessed February 2016.
4. Chinyama, M.P.M. "Alternative Fuels in Cement Manufacturing", Alternative Fuel, Manzanera, M. (Ed.), ISBN 978-953-307-372-9. InTech, (2011) DOI: 10.5772/22319.
5. EN 197-1. Cement - Part 1: Composition, specifications and conformity criteria for common cements, 2012.
6. EN 196-2. Method of testing cement - Part 2: Chemical analysis of cement, 2013.
7. EN 196-6. Methods of testing cement. Determination of fineness, 2010.
8. L. Bityukova, R. Mõtlep, K. Kirsimäe, Composition of oil shale ashes from pulverized firing and circulating fluidized-bed boiler in Narva Thermal Power Plants, Estonia, *Oil Shale*, 2010, Vol. 27, No. 4, pp. 339–353 doi: 10.3176/oil.2010.4.07.
9. Ferreiro, S., Herfort, D., Damtoft, J. S., "Effect of raw clay type, fineness, water-to-cement ratio and fly ash addition on workability and strength performance of calcined clay – limestone Portland cements," Cement and Concrete Research, Vol. 101, 2017, pp. 1–12.
10. http://www.flsmidth.com/~/media/PDF%20Files/Pyroprocessing/FLSmidth_FlashCalciner_Brochure_email.pdf.
11. EN 196-1. Methods of testing cement - Part 1: Determination of strength, 2005.
12. Osbaeck, B., "The Influence of Air Content by Assessing the Pozzolanic Activity of Fly Ash by Strength Testing*," Cement and Concrete Research*, Vol. 15, 1985, pp. 53-64.
13. Herholdt, A. D., Justesen, C. F. P., Christensen, P. N., Nielsen. A., "Beton-Bogen," Cementfabrikkernes tekniske oplysningskontor, Aalborg Portland , 2nd edition (1985). ISBN 87-980916-0-8.
14. De Weerdt, K., Geiker, M.R., "Comparing chloride ingress in Portland cement based binders with slag or fly ash exposed to seawater and deicing salt". In preparation
15. ASTM D1141 - 98, Standard Practice for the Preparation of Substitute Ocean Water, 1998 (Reapproved 2013).
16. De Weerdt, K. Ben Haha, M., Le Saout, G., Kjellsen, K., Justnes, H., Lothenbach, B. (2011) "Hydration mechanisms of ternary Portland cement containing limestone powder and fly ash," *Cement and Concrete Research,* Vol 41, pp. 279-291.
17. De Weerdt, K., Orsakova, D., Muller, A.C.A, Larsen, C.K, Pedersen, B.; Geiker, M.R., "Towards the understanding of chloride profiles in marine exposed concrete, impact of leaching and moisture content," *Construction and Building Materials.* Vol. 120, 2016.
18. Jakobsen, U.H., De Weerdt, K., Geiker, M.R., "Elemental zonation in marine concrete," *Cement and Concrete Research.* Vol. 85, 2016.

19. Shi, Z., Geiker, M.R., Lothenbach, B., De Weerdt, K., Ferreiro Garzón, S. Enemark-Rasmussen, K., Skibsted, J., "Friedel's salt profiles from thermogravimetric analysis and thermodynamic modelling of Portland cement-based mortars exposed to sodium chloride solution," *Cem. Concr. Compos*. Vol. 78, 2017, pp. 73 – 83.

APPENDIX

Table A1 – Total chloride content (%wt of dry mortar) after 90 days exposure to artificial sea water. Mean and SD (in brackets).

Depth [mm]	R1	B1	B2	B3	B4	B5	B6	B7	B8	B9
0.5	0.762 (0.051)	0.888 (0.011)	0.839 (0.055)	0.801 (0.042)	0.912 (0.081)	0.979 (0.030)	0.714 (0.051)	0.643 (0.082)	0.564 (0.023)	0.641 (0.057)
2	0.796 (0.062)	0.795 (0.040)	0.863 (0.060)	0.889 (0.034)	0.887 (0.110)	0.942 (0.038)	0.732 (0.068)	0.732 (0.105)	0.662 (0.031)	0.795 (0.027)
4	0.607 (0.044)	0.625 (0.022)	0.645 (0.043)	0.669 (0.023)	0.632 (0.058)	0.660 (0.038)	0.620 (0.043)	0.509 (0.053)	0.469 (0.037)	0.592 (0.014)
6	0.439 (0.035)	0.446 (0.030)	0.448 (0.027)	0.478 (0.026)	0.437 (0.020)	0.435 (0.008)	0.522 (0.031)	0.213 (0.034)	0.260 (0.021)	0.339 (0.030)
8	0.280 (0.022)	0.287 (0.025)	0.264 (0.024)	0.292 (0.018)	0.249 (0.009)	0.235 (0.024)	0.435 (0.010)	0.035 (0.014)	0.100 (0.006)	0.129 (0.032)
11	0.108 (0.005)	0.109 (0.019)	0.079 (0.033)	0.099 (0.015)	0.078 (0.018)	0.051 (0.040)	0.305 (0.006)	0.012 (0.008)	0.012 (0.008)	0.029 (0.003)
15	0.005 (0.000)	0.005 (0.000)	0.005 (0.000)	0.025 (0.002)	0.024 (0.001)	0.019 (0.007)	0.153 (0.003)	0.010 (0.004)	0.006 (0.001)	0.026 (0.002)
20	0.005 (0.000)	0.005 (0.000)	0.005 (0.000)	0.024 (0.003)	0.023 (0.001)	0.019 (0.006)	0.044 (0.007)	0.014 (0.007)	0.006 (0.002)	0.027 (0.002)

Table A2 – Total chloride content (%wt of dry mortar) after 180 days exposure to artificial sea water. Mean and SD (in brackets).

Depth [mm]	R1	B1	B2	B3	B4	B5	B6	B7	B8	B9
0.5	0.620 (0.061)	0.862 (0.016)	0.700 (0.110)	0.763 (0.094)	0.665 (0.134)	0.794 (0.041)	0.616 (0.039)	0.488 (0.127)	0.470 (0.061)	0.498 (0.022)
2	0.650 (0.075)	0.934 (0.030)	0.846 (0.167)	0.939 (0.041)	0.949 (0.063)	1.002 (0.033)	0.738 (0.036)	0.702 (0.014)	0.661 (0.022)	0.667 (0.007)
4	0.564 (0.094)	0.782 (0.032)	0.709 (0.120)	0.807 (0.040)	0.809 (0.081)	0.836 (0.064)	0.662 (0.031)	0.555 (0.097)	0.618 (0.025)	0.597 (0.006)
6	0.485 (0.076)	0.625 (0.027)	0.565 (0.068)	0.668 (0.027)	0.596 (0.092)	0.669 (0.065)	0.589 (0.025)	0.415 (0.045)	0.473 (0.024)	0.475 (0.016)
8	0.372 (0.057)	0.488 (0.033)	0.435 (0.030)	0.522 (0.019)	0.506 (0.048)	0.513 (0.049)	0.536 (0.021)	0.181 (0.010)	0.270 (0.004)	0.299 (0.017)
11	0.207 (0.047)	0.253 (0.025)	0.205 (0.030)	0.250 (0.031)	0.243 (0.033)	0.329 (0.126)	0.438 (0.023)	0.018 (0.007)	0.075 (0.013)	0.083 (0.013)
15	0.046 (0.024)	0.033 (0.017)	0.030 (0.015)	0.053 (0.002)	0.056 (0.001)	0.074 (0.015)	0.293 (0.008)	0.009 (0.004)	0.006 (0.001)	0.021 (0.003)
20	0.005 (0.000)	0.017 (0.020)	0.008 (0.003)	0.017 (0.001)	0.014 (0.001)	0.011 (0.003)	0.154 (0.002)	0.009 (0.003)	0.009 (0.002)	0.019 (0.001)
26	0.000 (0.000)	0.000 (0.000)	0.000 (0.000)	0.017 (0.000)	0.013 (0.001)	0.000 (0.000)	0.033 (0.029)	0.000 (0.000)	0.000 (0.000)	0.018 (0.001)
36	0.000 (0.000)	0.000 (0.000)	0.000 (0.000)	0.000 (0.000)	0.000 (0.000)	0.000 (0.000)	0.000 (0.000)	0.000 (0.000)	0.000 (0.000)	0.000 (0.000)

Table A3 – Total chloride content (%wt of dry mortar) after 270 days exposure to artificial sea water. Mean and SD (in brackets).

Depth [mm]	R1	B1	B2	B3	B4	B5	B6	B7	B8	B9
0.5	0.585 (0.022)	0.692 (0.064)	0.546 (0.101)	0.637 (0.065)	0.712 (0.072)	0.728 (0.121)	0.463 (0.023)	0.448 (0.039)	0.661 (0.201)	0.470 (0.020)
2	0.645 (0.054)	0.789 (0.041)	0.741 (0.082)	0.750 (0.064)	0.865 (0.064)	0.880 (0.048)	0.540 (0.039)	0.606 (0.037)	0.716 (0.044)	0.616 (0.061)
4	0.571 (0.037)	0.688 (0.031)	0.669 (0.090)	0.709 (0.074)	0.745 (0.064)	0.755 (0.091)	0.514 (0.037)	0.595 (0.051)	0.685 (0.048)	0.600 (0.064)
6	0.481 (0.033)	0.614 (0.021)	0.561 (0.078)	0.551 (0.075)	0.600 (0.089)	0.623 (0.118)	0.497 (0.026)	0.485 (0.111)	0.541 (0.029)	0.520 (0.052)
8	0.349 (0.105)	0.527 (0.030)	0.459 (0.086)	0.469 (0.054)	0.518 (0.050)	0.526 (0.099)	0.472 (0.017)	0.334 (0.054)	0.358 (0.009)	0.397 (0.054)
11	0.214 (0.081)	0.364 (0.044)	0.256 (0.101)	0.286 (0.029)	0.255 (0.033)	0.330 (0.028)	0.413 (0.024)	0.089 (0.034)	0.078 (0.062)	0.164 (0.027)
15	0.062 (0.055)	0.132 (0.076)	0.055 (0.032)	0.108 (0.014)	0.072 (0.011)	0.090 (0.018)	0.343 (0.031)	0.013 (0.001)	0.010 (0.004)	0.020 (0.001)
20	0.008 (0.007)	0.008 (0.003)	0.010 (0.003)	0.016 (0.001)	0.015 (0.001)	0.012 (0.001)	0.238 (0.027)	0.014 (0.002)	0.008 (0.005)	0.017 (0.001)
26	0.000 (0.000)	0.000 (0.000)	0.000 (0.000)	0.012 (0.001)	0.014 (0.001)	0.000 (0.000)	0.135 (0.015)	0.000 (0.000)	0.000 (0.000)	0.017 (0.000)
36	0.000 (0.000)	0.000 (0.000)	0.000 (0.000)	0.000 (0.000)	0.000 (0.000)	0.000 (0.000)	0.067 (0.008)	0.000 (0.000)	0.000 (0.000)	0.000 (0.000)

Concrete-Ice Abrasion Test with Sliding Ice and Ice Spallation

Guzel Shamsutdinova
M.Sc., Ph.D. candidate,
Norwegian University of Science and Technology
Richard Birkelands vei 1a, NO-7034 Trondheim
e-mail: guzel.shamsutdinova@ntnu.no

Max A.N. Hendriks
M.Sc., Ph.D., professor
Norw. Univ. of Sc. and Tech./Delft University of Technology
Richard Birkelands vei 1a, NO-7034 Trondheim
e-mail: max.hendriks@ntnu.no / m.a.n.hendriks@tudelft.nl

Stefan Jacobsen
M.Sc., Ph.D., professor
Norwegian University of Science and Technology,
Richard Birkelands vei 1a, NO-7034 Trondheim
e-mail: stefan.jacobsen@ntnu.no

ABSTRACT
The concrete-ice abrasion process is a surface degradation mechanism due to ice-structure interaction. The ice drift can cause wear rates on high quality concrete that can be in the order of 0.1 – 1 mm per year. The topic is especially relevant for concrete gravity-based structures in the Arctic offshore. So far, experiments have been the main evaluation method for concrete durability under ice abrasion. This paper presents concrete-ice abrasion experiments between the surface of sawn concrete (28 days cubic compressive strength 90 MPa) and fresh-water ice. Based on our results (ice pressure, ice consumption rate, coefficient of friction, abrasion depth) and visual observations, we identified two types of interaction between the concrete surface and the sliding ice specimen: sliding and sliding with spallation of ice. The results show both higher abrasion and higher friction during sliding-spallation, than during sliding, under otherwise identical experimental conditions. The increased damage with ice spallation indicates that the damage mechanisms could be some form of three-body wear.

Key words: Concrete, ice, abrasion, experiments.

1.   INTRODUCTION

The concrete-ice abrasion process has been studied for the last 30 years, and has been defined as the surface degradation of concrete structures due to interaction with drifting ice floes. Several research groups have studied this topic through laboratory experiments [1-6] and field observations [1, 7]. A recent review [8] has proposed mechanisms, which can contribute to damage of concrete due to sliding ice: high concrete tensile stress from ice asperity sliding contact, water pressed into cracks on wet ice-collision, three-body wear and fatigue from repeated asperity contacts.

The collision of an ice floe with a circular concrete column causes various behaviour of ice around the column, such as crushing, transition region between crushing and sliding, and sliding (Figure 1). Region 1 is characterized by the frontal collision of the ice floe against the structure. The ice imposes high normal stresses on the concrete surface [8], and ice crushing takes place when the stresses reach a limit along the contact area [9]. A series of indentation tests [10-12] have been made on this interaction.

The crushing of the ice was found to be the dominant failure mechanism when the indentation speed was high and the ratio of structure width to ice thickness was low. Region 2 is the transition region between Regions 1 and 3. Here normal loading decreases and tangential loading increases [8]. Crushed fragments of the ice floe get locked in the interaction zone. The ice floe drives them along the concrete structure. Some subsequent local crushing of fragments can take place. Region 3 is the sliding zone [6, 8, 13], where the ice floe slides along both sides of the concrete column.
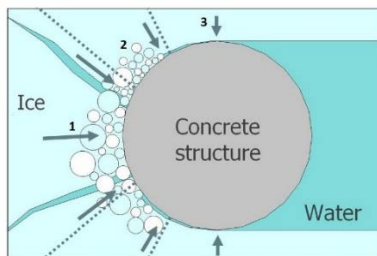
Figure 1 – Schematic of interaction of ice floe with concrete structure (top view). Region 1 – crushing; Region 2 – transition region; Region 3 – sliding.

Laboratory examinations in Canada [6] simulated all these types of interaction between a conical ice sample and a concrete sample to facilitate analysis of the abrasion process. The authors concluded that Region 1 experienced the highest level of concrete-ice abrasion. A potential critical parameter during this test is the conical shape of the ice sample. The cone tip is possibly destroyed in the beginning of a test after a limited sliding distance and may hamper interpretations accordingly.

Field observation studies on bridge piers in Hokkaido, Hara et al. [14], claim that ice interaction with concrete in Regions 1 and 2 causes more abrasion than in Region 3. Møen et al. [15] measured the abrasion depth on the Raahe lighthouse (the Gulf of Bothnia) in-situ, with known annual ice drifting data. The authors reported that the abrasion rate was highest in Region 3. The differences in the conclusions based on field observations is remarkable. Two issues are worth mentioning and might possibly explain the differences. Firstly, the bridge pier [14] has a semi-circular cross section, whereas the lighthouse has a circular cross section. Secondly, the ice drift direction is much easier to detect for rivers, than for a sea.

The different opinions on concrete-ice abrasion origin and unknown mechanics behind the degradation process requires that this topic should be investigated further. The present paper describes a laboratory method of a concrete-ice abrasion study. An evaluation of various methods of testing concrete-ice abrasion resistance [16] recommends the sliding abrasion test as the most appropriate in terms of assessing abrasion caused by ice floe movements. The sliding abrasion test fulfils the required conditions; the most critical are ability to vary the contact pressure and action of both kinetic and static coefficient of friction alternatively. And, so far,

most experimental work has been based on the sliding interaction between ice and concrete, either ice on concrete [4, 5, 17] or concrete on ice [2, 6, 18, 19].

Our laboratory method was based on the sliding of an ice sample along a fixed concrete sample. It is hence a friction test with a constant normal loading as the only load. It is intended for studying concrete-ice abrasion as a standalone deterioration mechanism that can occur without any other deteriorating mechanism (such as freeze/thaw, chemical attack, corrosion of reinforcement, etc.). The scope of this paper is to present our experimental system and to simulate sliding between fresh water ice and a sawn concrete surface. Furthermore we demonstrate that the setup that slides ice on concrete gives opportunities to test various sliding: sliding and sliding with ice spallation.

2. EXPERIMENTS

The experimental study included simulation of concrete-ice abrasion followed by measurement of abrasion depth. The abrasion machine simulated concrete-ice abrasion with an ice specimen sliding along a fixed concrete sample. The concrete abrasion was measured using a laser scanner. The experimental equipment, materials tested, and the experimental set-up are described below.

2.1. Abrasion Machine

The abrasion machine is a modified shaping machine (Figure 2(a)). It has been used for concrete-ice abrasion testing since 2008. The machine was recently renovated in collaboration with the mechanical and electronics workshops at the Department of Structural Engineering, NTNU. The setup is now able to control the sliding distance, velocity, vertical loading, horizontal and vertical load responses, room temperature, and concrete surface temperature. The components of the abrasion machine are described below.

Mechanical parts
The machine makes the ice sample holder move in repeated sliding movements in a horizontal direction. The horizontal stroke length of the machine is constant and equals 200 mm. An electronic motor control regulates the velocity of the stroke. Figure 3 (b) is a position plot showing the sinusoidal motion and velocity of an ice sample. The velocity is derived from position and time. The average velocity in this experiment was 0.16 m/s.

The engine on the top (Figure 2(a)) drives a vertical piston, which continuously pushes the ice sample against the concrete surface with a constant load. The piston and machine stop automatically when the desired consumption level of ice is reached at 110 mm.

The concrete sample is positioned on a linear sliding system and fixed with a pre-stressing screw on one side (on the right in Figure 2(b)) and a horizontal load cell on the other (on the left in Figure 2(b)). The linear ball bearing sliding system has a very low coefficient of friction (μ=0.0015-0.005). Two vertical load cells under the sliding bearing system measure the vertical load response.

(a)   (b)
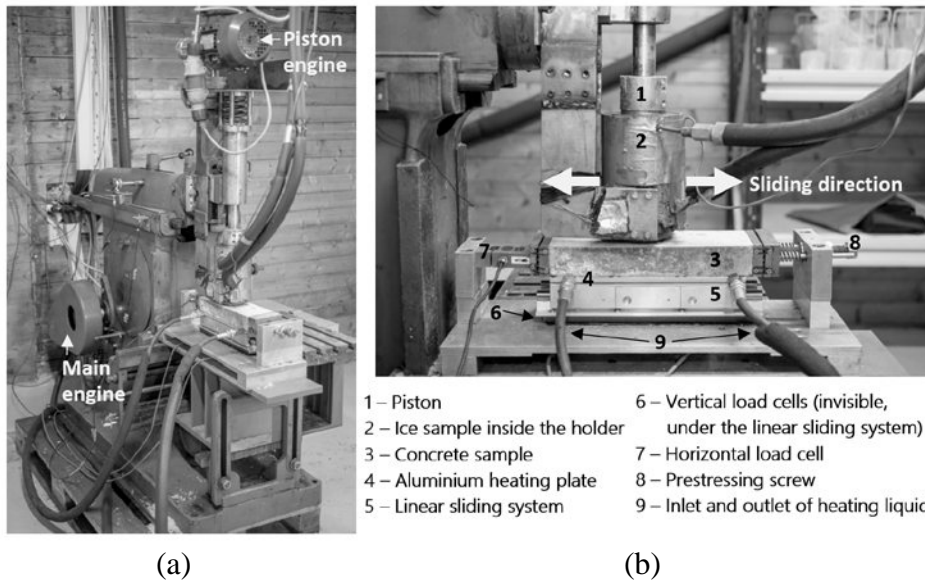
Figure 2 – The concrete-ice abrasion machine photographs: (a) side view; (b) close view of parts.

(a)   (b)
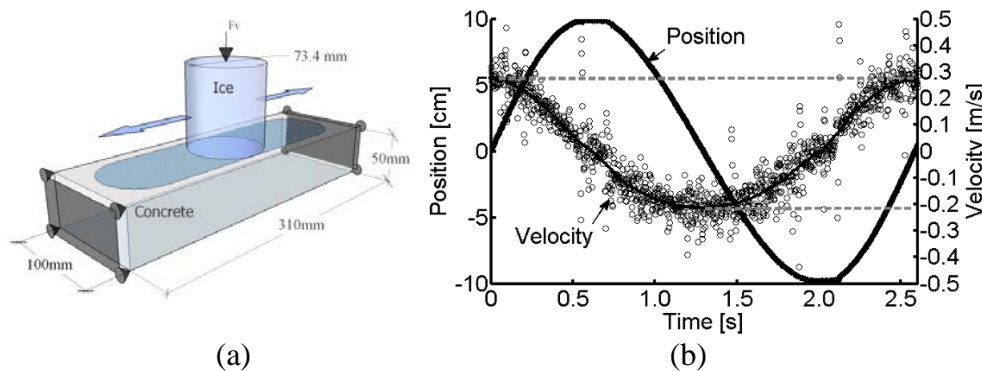
Figure 3 – (a) Simplified principle of concrete ice abrasion test; (b) Position plot showing sinusoidal motion and velocity of ice (average velocity is 0.16 m/s).

Cooling and heating

The temperature in the concrete-ice abrasion lab is kept at a constant temperature of −10 °C. The cooling system is installed in the roof of the lab and generates cold air. The control unit maintains the target temperature.

Møen et al. [5] reported the importance of an ice-free surface of the concrete sample during the test, since icing on concrete surface prevents concrete degradation due to interaction with ice. So we prevented the freezing of concrete sample surface by heating it up from the bottom. The concrete specimen temperature control goes through an aluminium heating plate that is attached to the sliding bearing system below the sample (Figure 2(b) no.4). The plate has a channel inside, connected to a controlled temperature liquid (alcohol) circulator. The temperature of the concrete surface in the concrete-ice abrasion zone, before the test, was adjusted to +2°C (measured with an infrared thermometer). A supplementary numerical analysis of temperature distribution within concrete was conducted solving the heat transfer equation (Fourier`s law) in STAR-CCM+. The thermal properties of the concrete and the effective heat transfer coefficient were set equivalent to those provided in [5]. The numerical solution returns +2.8°C as the steady-state temperature at the point where the experimental measurement was done; hence the numerical results are within the interval of instrumental uncertainty.

Feedback system, load control

There is a feedback and logging system, programmed with National Instruments *LabVIEW* with hardware interface. This system enables control of the vertical and horizontal load with response logging up to 500 Hz, previously the rig had a much lower logging frequency of 10 Hz.

The feedback system records the fluctuation of loading during ice movement back and forth, and maintains the target ice pressure. A horizontal screw (Figure 2(b) no. 8) fixes the concrete sample against a horizontal load cell. The pre-stressing value is 4200 N, which keeps the sample fixed in a horizontal direction during the test.

Data acquisition

The concrete-ice abrasion rig is operated with software specially developed and written at the Department of Structural Engineering, NTNU. The output is two text files. The first includes friction parameters (time, position, horizontal and vertical load responses) logged at 500 Hz, and the second file logs the total sliding distance, vertical position of the piston, number of cycles, and temperature at 0.17 Hz frequency.

2.2.   Laser Scanner

A review of the literature shows a variety of equipment used for concrete surface examination, including a digital indicator [2, 5], an optical microscope [4], a structural light scanner [20], a calliper and surface roughness measurement device (up to 160 µm) [21]. The digital indicator and calliper have to be adjusted manually for each measuring point, which decreases the accuracy of measurement even though the accuracy of the device itself is high. Moreover, it is hard to get a sufficient number of measuring points in a reasonable period of time. The classical optical microscopy technique allows observation of the surface, but gives no quantitative characteristics. In contrast, a structured light scanner gives a fine triangular mesh in a few seconds, but depends on surface colour and cannot detect black aggregates or dark shadows inside air voids.

Based on the literature review and experiences with structured light scanning [22], we decided to build a non-contact Laser Scanning device, which allowed us to scan the concrete surface with an accuracy of 10 µm in a reasonable time independent from the surface colour. The components of the laser scanner are listed and described below.

Linear Motion System

The measuring equipment is based on a laser that is fixed on a linear motion system (Figure 4(a)). The laser moves continuously along the sample according predefined "snaking" path. The control panel determines the dimensions of the measuring area, the velocity of the laser in the Y direction (Figure 4(b)), and the step size in the X direction (Figure 4(b)). To achieve measurements in a coordinate system for the continuous movement, the laser velocity and logging frequency were adjusted and synchronized. To complete the measurements in a reasonable time, the following parameters were chosen: the measuring point distance is approximately 50 µm in the Y direction, and the step size in the X direction is 1mm (Figure 4(b)). The movement speed of the laser sensor was set to 10 mm/sec.

The measuring area exceeds the sample surface to ignore the acceleration and deceleration region of the laser at its turning points.
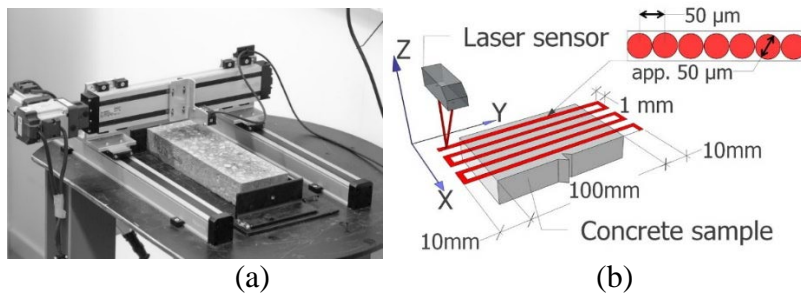
Figure 4 – Laser scanner: (a) photo; (b) simplified schematic of measurement process (not to scale).

Laser

The measuring part of the equipment is a micro laser distance sensor. The repeatability is 10 µm, the measuring centre distance is 30 mm, and the measurement range is ±5 mm from there. The laser beam diameter is approximately 50 µm. The response speed of the laser was set to 5 ms (200 Hz) to synchronize the laser with the motion system and the computer logging frequency.

Data control and acquisition

Data are logged to the computer using laboratory software at a logging frequency of 200 Hz. The measurement output comprises the surface heights in the Z direction, along the scanning path.

The measurements made outside the surface sample (Figure 4(b)) are ignored. The rest of the data is transformed to a matrix of surface heights, with dimensions of 1900x300 points.

2.3.   Ice

Our abrasion machine is designed for fresh-water cylindrical ice samples. This simplification, from sea-water ice to fresh-water ice, was made for two reasons. Firstly, sea-water ice has complicated mechanical properties and can involve extra parameters to the main physical mechanism. Secondly, fresh-water ice increases the service life of the machine. And thirdly fresh ice samples have been used in several earlier studies with sliding tests [4-6]. The fresh-water ice quality in these studies include frozen tap water [5], artificially grown polycrystalline and anisotropic ice [6], and artificially grown columnar ice [4].We used a simplified method to grow ice unidirectionally from tap water.

The ice samples for the test have a cylindrical shape with a diameter of 73.4 mm and 160 mm high. An ice mould made of polyoxymethylene (POM) 13.3 mm thick and 370 mm high (Figure 5(a)) and covered with thermo-insulation on the sides and the bottom is filled with tap water and put in a freezer at −20 °C for 48-72 hours. The freezing of the water starts at the top of the mould progressing downwards, but later it also takes place from the bottom (Figure 5(b)). Therefore, the top part of the ice-sample is frozen unidirectionally whereas the bottom part contains unfrozen water and results in a more porous ice with air voids. The upper part of the ice sample (160 mm) was hence unidirectionally grown ice without visible air voids and was used for the test (Figure 5(c)). The test ice samples are cured in plastic bags before the test to avoid sublimation.
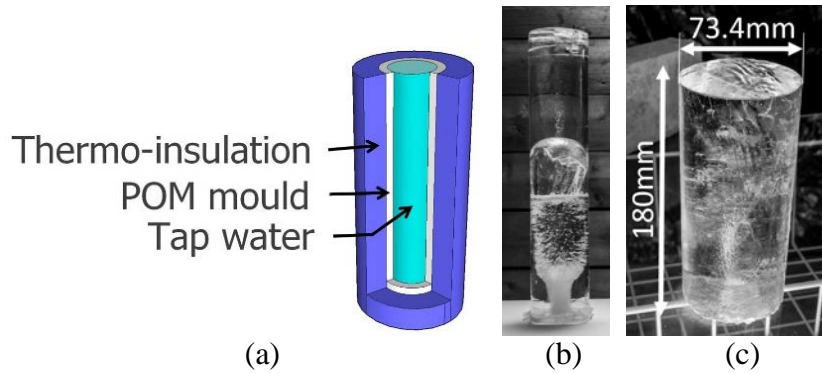
Figure 5 – (a) Schematic of ice production; (b) ice sample after 48 hours; (c) ice sample for the test.

2.4.   Concrete

The tests were carried out with a concrete sample made of Norcem Anlegg (CEM I) cement (with 2% Elkem silica fume substitution) and mixed natural and crushed granitic aggregate fromÅrdal (sand, 0-8 mm and coarse 8 – 16 mm grain size). The mix was made using the following proportions: W/(C+2S)=0.42, where W, C and S are the weight of water, cement and silica fume powder, respectively. The cement paste volume fraction was 29.5%. Superplasticizing additive Dynamon SX-23 from Mapei was used to achieve the target workability.

The fresh concrete properties were determined in accordance with EN 12350 [23], part 2 (slump measure), part 6 (density) and part 7 (air content), approximately 10 min after water addition. The slump spread was measured as the diameter of the collapsed slump cone. The results are given in Table 1.

The compressive strength of the concrete was 90 MPa (measured on 3 parallel cube samples at 28 days). The samples were classified as B75 according to NS-EN 206:2013+NA:2014 [24]. Samples for the concrete-ice abrasion testing were sawn and cured in water at +20°C for 11 months before the experiments. Some calcium leaching presumably took place in this period, though similar for all specimens and it could also reflect some kind of field leaching. The development of the concrete compressive strength over the curing time is plotted in Figure 6.

The concrete sample used for the concrete-ice abrasion test was a miniature slab measuring 100x310 mm and 50 mm high (Figure 3(a)).

Table 1 –Fresh concrete properties of tested mix

Density, kg/m^3	2455
Air content, %	0.9
Slump measure, mm	200
Slump spread measure, mm	420
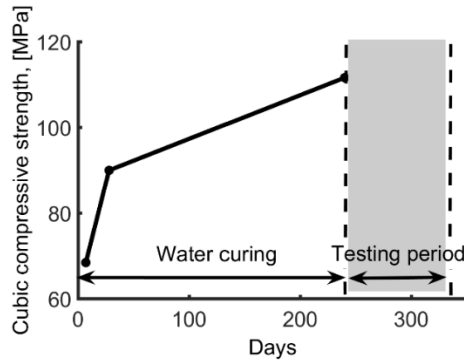
Figure 6 – The development of concrete compressive strength over curing time.

2.5. Abrasion test set-up

The main variables in sliding concrete-ice abrasion testing are usually ice pressure, sliding velocity, temperature, ice and concrete properties. The ice pressure and concrete strength are normally viewed as the most significant parameters, which cause increasing abrasion depth at increased pressure and reduced strength in line with Archard's law and tribology [25, 26]. In earlier studies, ice pressure varied from 0.05 MPa [4] to 3 MPa [2, 19]. The temperature of the ice can give different results. Most researchers report an increasing ice abrasion rate with decreasing ice temperature [19, 27], but not Bekker et al. [28]. Jacobsen et al. [8] suggest that high sliding velocity (10 times higher than in other tests) might have caused the difference. Studies of the effect of ice temperature on the coefficient of friction (COF) concluded that the COF increases with decreasing temperature in sea ice [17] and fresh ice [5].

This research presents two different experimental conditions: concrete-ice abrasion sliding test and concrete-ice abrasion sliding test with ice spallation. In order to simulate these two different types of sliding we varied the thickness of the concrete sample (Figure 7), all other parameters were constant. The ice pressure (average pressure on apparent contact zone) was 1 MPa, as the most appropriate for our laboratory equipment. The temperature effect was outside of the scope of this research, thus the temperature during the test was constantly $- 10°C$.

All samples were from one concrete mix. As mentioned above, these experiments studied abrasion on a sawn concrete surface, as recommended in literature [3], where three different phases are presented: cement paste (with air voids), interfacial transition zone (ITZ), and aggregates.

(a)   (b)
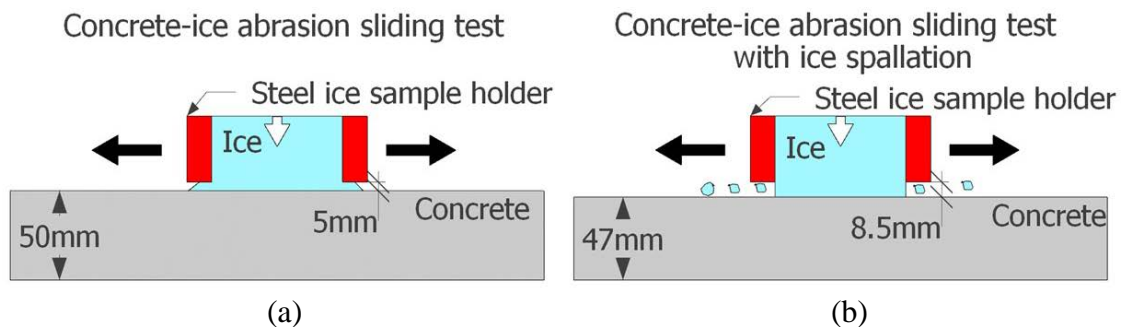
Figure 7 – Abrasion test set-up: (a) concrete-ice abrasion sliding test; (b) concrete-ice abrasion sliding test with ice spallation. (Also see Figure 10)

3. RESULTS AND DISCUSSION

The results include typical examples of vertical and horizontal load cell responses, various ice consumption, calculated coefficient of friction, and abrasion measurements.

3.1. Vertical load response

Figure 8 shows the vertical load cell response with the position of the ice specimen for both sliding and sliding-spallation. The plots represent the accumulated data from 1km of effective sliding distance. Figure 8 reveals a limited asymmetry of the machine. The ice pressure varies with the position of ice specimen and is on average higher on the right hand side, though the distribution functions seem fairly narrow and symmetric and with peak value very close to 1.0 MPa.

Figure 8(b) shows higher scatter of data with an occasionally decreasing ice pressure, that was caused by ice spallation during the test. The plotted frequency distributions of the ice pressure demonstrate that 96.7% of data are in range of 0.9 – 1.1 MPa. The distribution functions are only a bit less symmetric, though somewhat broader with spallation than with sliding, and still with peak value very close to 1.0 MPa.

Figure 9 shows a few typical time series with variations in vertical load cell response and corresponding ice consumption during sliding-spallation test over 2000 seconds. The time series in these experiments is limited by the consumption of the ice specimen. Figure 9 (a) shows a gradual spallation of the ice sample during the test where the ice pressure remained constant during the test. The corresponding ice consumption (Figure 9 (a) right) shows a gradual decrease of the ice specimen length. Ice fragments were observed on the concrete surface during the test. Figure 9 (b) shows that the time series is shorter with two sharp decreases in loading and a corresponding high consumption of ice in the same period of time. The sharp decrease in loading we call "pulverization", because at this moment during the test we observed the rapid appearance of small ice fragments in the interaction zone (Figure 10(b)). The ice pressure recovered directly afterwards, with the piston pushing the ice sample against the concrete surface. The ice fragments that could not withstand the load were extruded away from the ice sample holder.

(a)
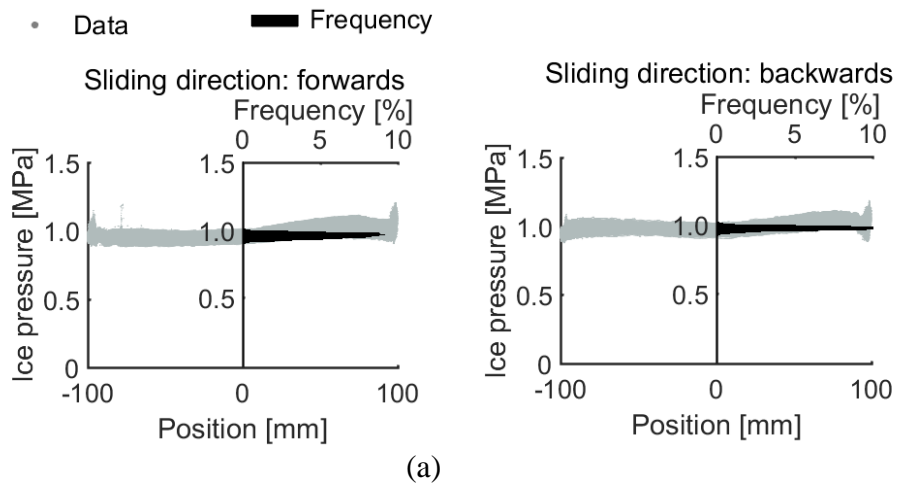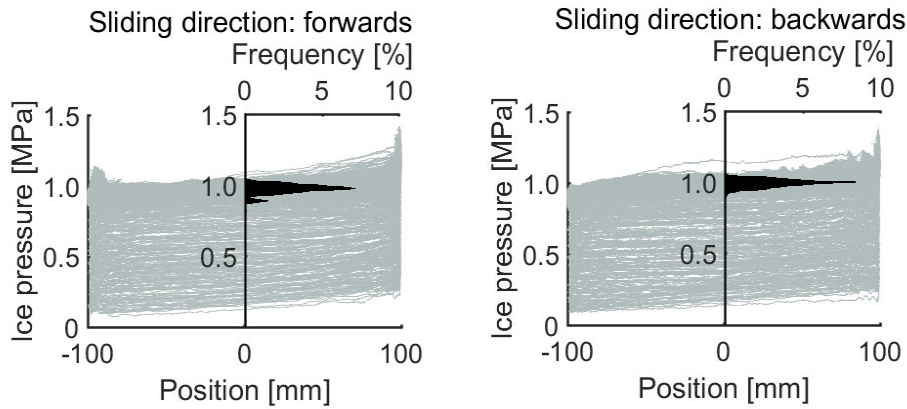
(b)

Figure 8 – The vertical load cells' response with the position of the ice specimen, and frequency distribution of ice pressure at position-0: (a) sliding test, (b) sliding test with ice spallation. The data were logged at 500Hz during app. 5 hours of sliding tests (1km of effective sliding distance).
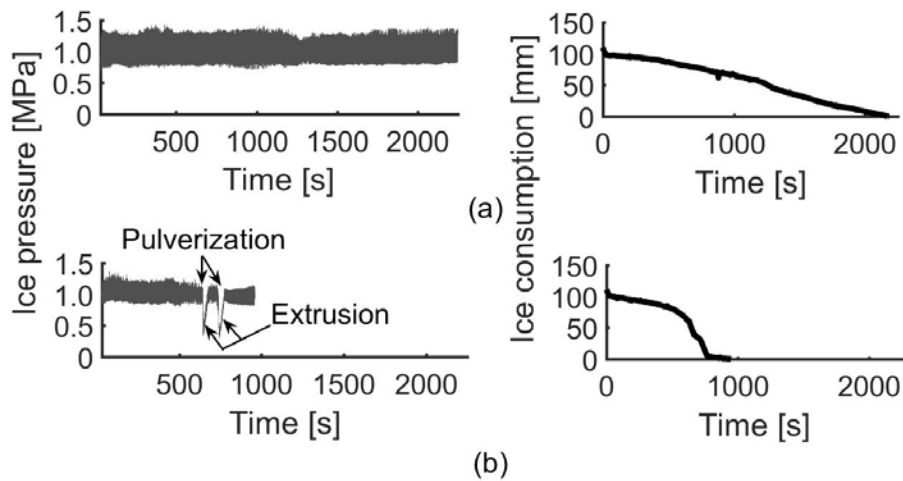
Figure 9 – Typical time series of the vertical load cell response and corresponding ice consumption, during sliding test with ice spallation: a) gradual spallation b) spallation with pulverisation.

Figure 10 shows the difference between two types of sliding during the test. Where thin film of water on the concrete surface can be observed during sliding test (Figure 10 (a)), and ice fragments and ice slush during sliding-spallation (Figure 10 (b)).

Figure 10 – Photos of concrete surface during two types of test: (a) sliding; (b) sliding-spallation.

3.2. Horizontal load response

The type of experimental conditions, sliding and sliding with ice spallation, did not effect on the horizontal load cell response. Figure 11 shows typical time series of the horizontal load cell response. The measurements show a descending trend at the beginning of each test series. The horizontal response of the pre-stressed sample (without ice sliding) shows the same trend. This trend is addressed to the stress relaxation of the pre-stressing screw (Figure 2(b) no.8). The trend was removed using a Savitzky-Golay FIR (finite impulse response) smoothing filter with a linear polynom. The time series was divided into three time intervals. The first time interval is characterized by the beginning of sliding; it lasts for approximately 90 seconds and shows an unstable horizontal response. The second interval is characterized by the stabilization of the horizontal response. The third interval shows a stabilized horizontal response. Hence the horizontal load is considered stable.
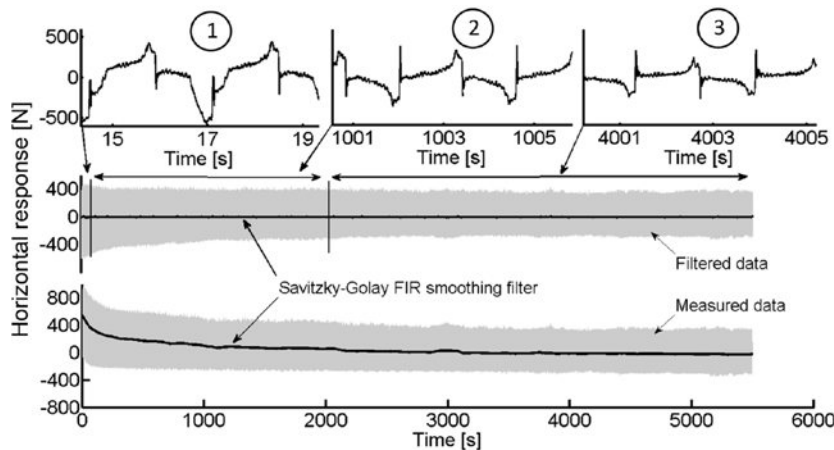
Figure 11 – Typical time series of the horizontal load cell response.

3.3. Ice consumption

Figure 12 shows the typical ice consumption for two experimental conditions per km of effective sliding distance. The apparent sliding distance is 200 mm per half-cycle, but the effective sliding distance is limited by the diameter of the ice sample (73.4 mm), due to the cylindrical shape of the ice samples. This means that 1 km of effective sliding distance (sliding felt on a point on the concrete surface) can be achieved through 2.7 km of apparent sliding distance of the ice specimen (see insert in Figure 12). Figure 12 shows that there are large differences in ice consumption between the different between two experimental conditions. From tribology [29] we know that both quality and consumption of mating material (ice) can be of importance.
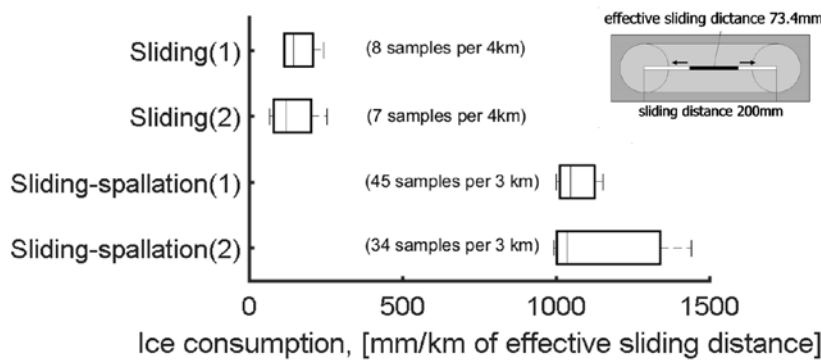
Figure 12 – Box plot of ice consumption per km of effective sliding distance (see insert), for two types of sliding. Information in brackets shows ice samples consumption.

Figure 13 shows the difference between the ice samples after the concrete-ice abrasion sliding test with the formation of a flat ice top after contact with the concrete (a), and after sliding-spallation with the fragments of ice removed (b). In case of a sliding test, the ice sample is always flat and smooth in the contact with concrete. However, in a sliding-spallation test, ice fragments were constantly removed from the contact zone and the ice sample had irregular shape in the contact zone with concrete. Since factors like roughness (like the number and shape of asperities) and the contact area are important parameters in wear, we registered these features and will analyse and discuss their significance in more detail further below and in later parts of this work.

(a)   (b)
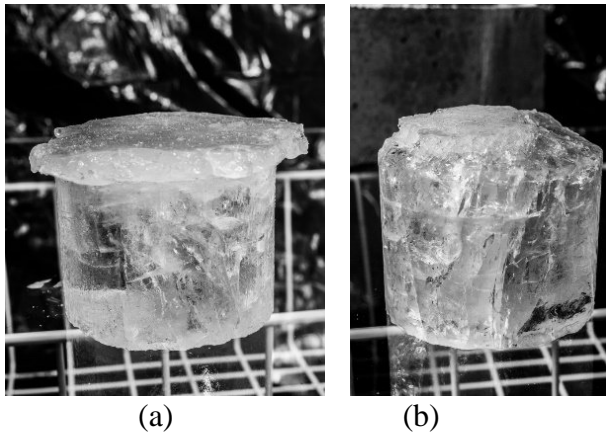
Figure 13 – Ice samples after concrete-ice abrasion test: a) sliding; b) sliding-spallation. The concrete was in contact with the top surface (i.e. the ice is upside-down on the photos).

Since the highest consumption of the ice corresponded to sliding-spallation test, the ice specimen was observed after 5 minutes of the sliding test (Figure 14). Compared to the crack free sample in Figure 5 it is possible to see that macro cracks propagated through the sample, while there were micro cracks close to the contact zone. The sharp edges in the contact zone show where ice fragments were pulled out.
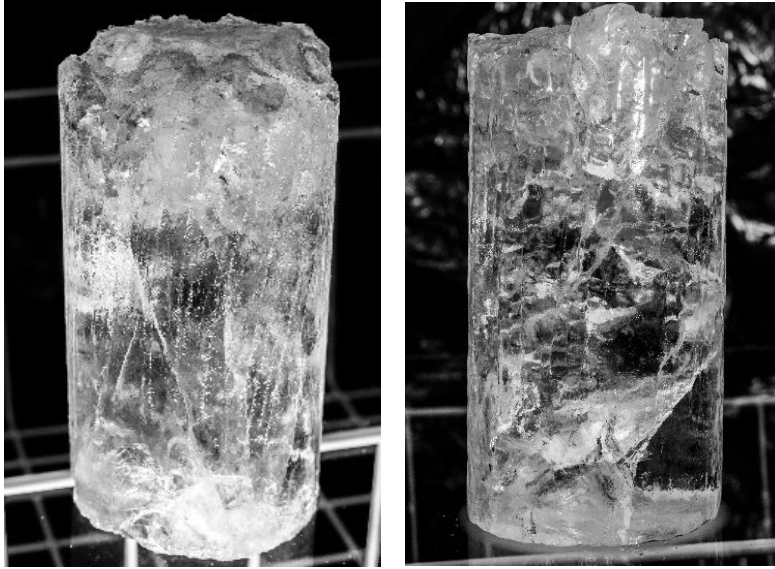
Figure 14 – Ice sample after 5 minutes of sliding-spallation test. The concrete was in contact with the top surface (i.e. the ice is upside-down on the photos).

3.4. Coefficient of friction

The coefficient of friction for two types of sliding is plotted in Figure 15 together with the sinusoidal movement of the ice specimen back and forth on the concrete surface. Comparing the COF plot with the position plot shows that at the turning points of the ice specimen where there is a full stop, the COF is higher. We can hence distinguish the coefficient of kinetic friction during sliding interaction, and the coefficient of static friction at turning points. The coefficient of kinetic friction varied in a range from 0 to 0.04, whereas the coefficient of static friction varied from 0.075 to 0.125. Figure 15 shows that sliding resulted in the smallest COF and sliding-spallation the highest COF. These data demonstrate the influence of experimental conditions on value of coefficient of static and kinetic friction. The increased friction during the spallation exposure will be later addressed to higher abrasion of concrete (Section 3.5).
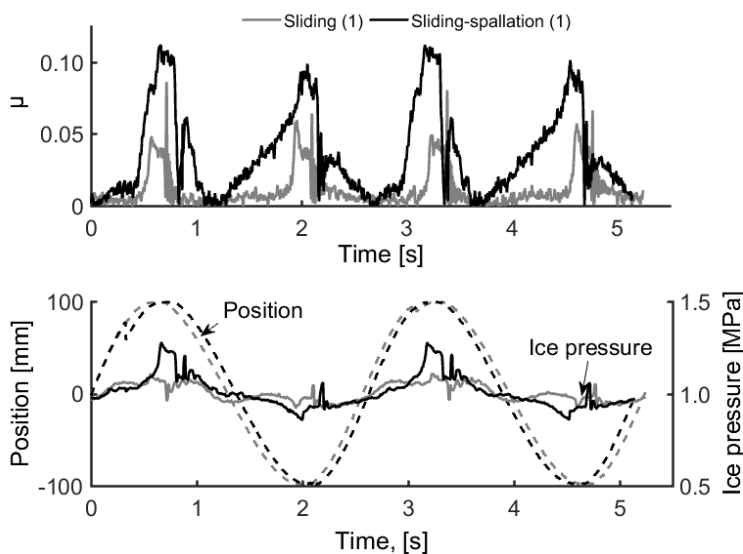
Figure 15 – Coefficient of friction for two types of sliding and the corresponding ice pressure distributions on the position plot.

Figure 16 shows the distribution of the signed COF and the ice velocity depending on the position of the ice specimen during sliding-spallation test. The negative sign of the COF indicates the negative horizontal response when sliding backward. The results demonstrate the effect of the sinusoidal ice motion (as described in section 2.1) on the coefficient of friction. The central part of the concrete sample is subjected to kinetic friction, and the right and left sides are more linked to the static coefficient of friction.
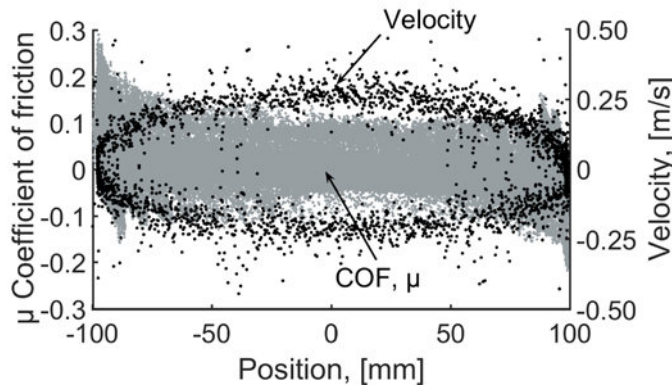
Figure 16 – Signed COF and ice velocity with the position of the ice specimen during sliding-spallation test.

3.5. Concrete-ice abrasion

Figure 17 shows the concrete surface before and after the three-kilometre of concrete-ice abrasion test under sliding-spallation condition. The aggregates protruded visibly during the test. This observation is important, since it indicates that the "classical" protruding aggregate concrete-ice abrasion model by Huovinen [1] also appears to hold for our test with a high strength concrete (HSC) and with sawn surfaces.

(a)   (b)
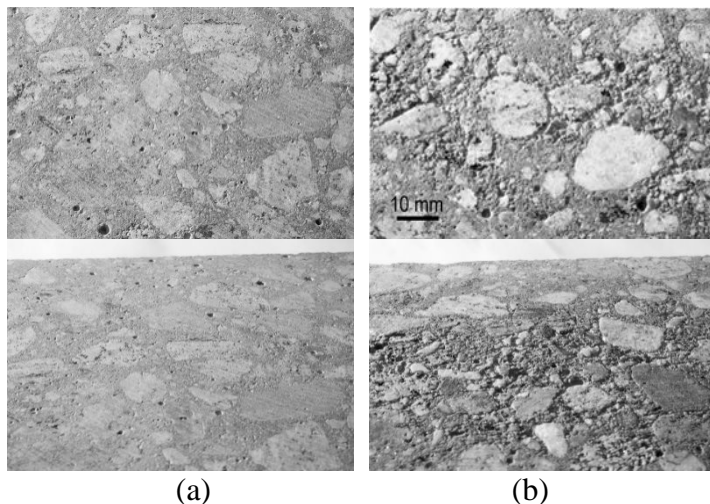
Figure 17 – Sawn concrete surface: (a) before concrete-ice abrasion test, (b) after 3 km of effective sliding distance (sliding-spallation test). Top view (top row) and perspective view (bottom).

Based on the surface measurements, abrasion was found as difference between the unabraded zone on the edges of the concrete sample and an abraded central band of 10 mm wide, same

method as used with the mechanical measurements in [5]. However, a much higher number of data points was collected with the laser scanner, so the calculation here was done for each millimeter of concrete sample length. Figure 18 (a) shows the average profile of the abraded central band (10 mm wide) along the sample length, shed and solid lines shows the abrasion. Figure 18 (b) shows average abrasion of the central band (between length positions 87 mm and 163 mm) with effective sliding distance. The results were compared with previous research [5], gray lines in Figure 18 (b) based on average abrasion rate reported in [5].

Beside the wear rate, the roughness of the concrete surface and along profiles is in the focus of our interest and being investigated in further work. Figure 18 also points out a scatter between individual samples.

(a)

(b)
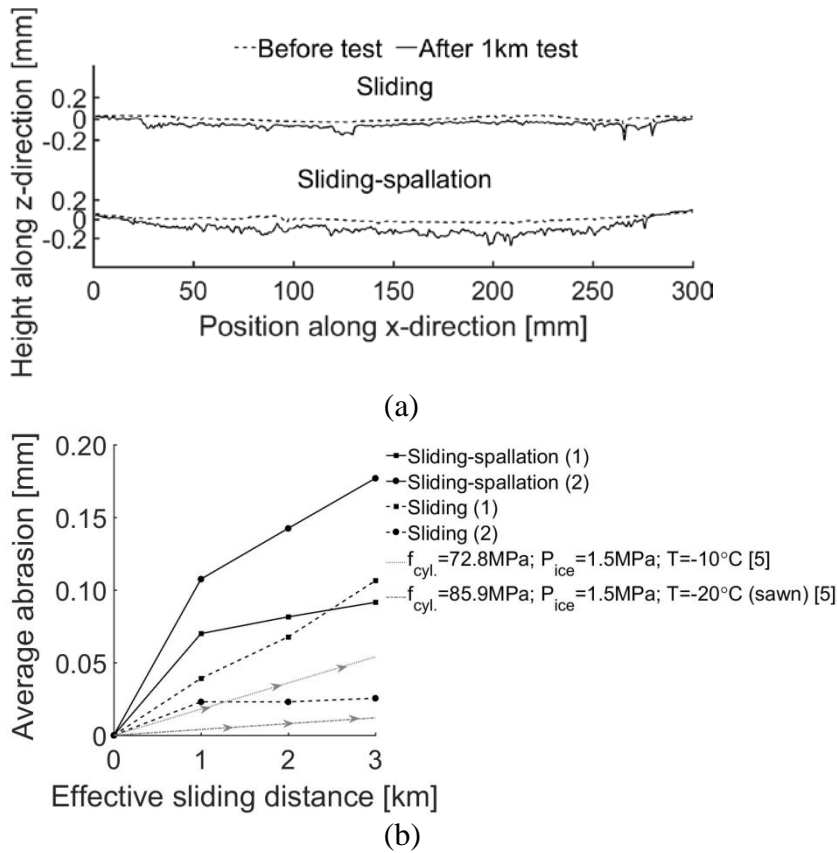
F*igure 18 – (a) Average profiles, of the central abraded band (10 mm wide, between position 87 and 163), of sawn concrete surface along the sample length before and after 1 km abrasion test; (b) average abrasion of the central band with effective sliding distance.*

3.6.   Abrasion, friction, previous HSC tests, ice cracking and sliding vs spallation

The COFs measured are of the same magnitude as the test results of other concrete-ice abrasion tests with the same sliding speed (0.16 m/s): 0.00 – 0.01 and 0.06 respectively [5, 19]. Whereas Itoh et al. [19] had an ice pressure 0.2 MPa, which is five times smaller than in our test. Comparison of our results with other research [30] in which the sliding speed was lower (in the range from $1.67 \cdot 10^{-6}$ to $1.67 \cdot 10^{-4}$ m/s) shows that our measurements of friction are lower. This is in line with earlier findings of decreasing COF with increasing velocity [31].

The abrasion depth results for sliding test were similar to those of Møen et al. [5], where concrete samples with cylindrical compressive strength 72.8 and 85.9 MPa under similar experimental conditions had an average abrasion rate of 0.018 and 0.004 mm/km of ice sliding (respectively). On the other hand, sliding-spallation shows an average abrasion rate 0.045 mm/km. The results for two parallel samples (1) and (2) have a large spread. However, comparing Figures 12 and 18(b), shows that although the results from the two parallel samples are scattered, there is a relation between ice consumption and abrasion of concrete. Concrete-ice abrasion is higher for higher ice consumption.

Based on our results and observations we distinguished two types of sliding: sliding and sliding-spallation. The first type, corresponds to abrasion set-up on Figure 7(a). As mentioned earlier, the heating plate heated the concrete sample from the bottom. It gave a temperature at the concrete sample surface of +2°C at the start of the test. During sliding interaction with ice, the concrete surface was cooled down, and its temperature fluctuated between −1.8 and −2.6 °C. After less than approx. one hundred cycles of ice movement, the ice samples had many cracks close to the contact zone. These cracks caused ice degradation during further sliding. Broken-off ice fragments started to deposit on the edge of the ice sample holder (see Figure 13(a)). There was a constant thin film of water on the concrete surface with minor icing spots during the test.

The second type of concrete-ice abrasion sliding test is sliding with ice spallation (Figure 7(b)). The concrete surface temperature was identical to the sliding case. The critical parameter causing the transition from sliding to sliding-spallation was the height of the concrete sample (or i.e. the gap between the ice sample holder and the concrete surface). As mentioned above, ice became stuck between the ice sample holder and the concrete surface during sliding test, whereas during the sliding-spallation test, as soon as the coalescence of cracks caused ice degradation, the fragments of ice escaped from the contact zone through the gap.

The sliding-spallation had a particular case, when the amount of micro cracking in the ice sample reached some limit and caused the rapid pulverization of ice (Figure 9(b)). The extrusion of pulverized ice took only a few seconds before loading was recovered. Rapid pulverization was observed to occur randomly for some ice samples during the tests.

An effect of the width of the gap between the ice sample holder and the concrete surface was found in tests with identical temperature, loading, and ice and concrete quality parameters. Tests where the gap width was 8 mm resulted in sliding-spallation type, while tests with a gap width smaller than 5 mm resulted in sliding. The sliding-spallation test caused more abrasion than the sliding type at the same ice pressure. The sliding-spallation produced more ice debris as seen from the increased ice consumption rate and large amount of ice slush debris (Figure 10(b)). This highlights, that sharp ice fragments play an important role in concrete-ice abrasion, and hence it will be of importance to look closer at concrete surface roughness, shape and size of ice- and concrete wear debris. Size of concrete wear debris should be compared to the depth of simulated surface cracks [32] to improve our understanding of concrete ice abrasion mechanisms.

4.   CONCLUSIONS

We distinguished two sliding interactions between the concrete surface and ice during concrete-ice abrasion laboratory experiments: sliding and sliding-spallation. Our experimental concrete-ice abrasion set-up enables to simulate them through the variation of concrete sample height,

thus varying the open height of ice in the gap between the ice sample holder and the concrete surface.

The results show higher abrasion and higher friction during sliding-spallation tests, than during sliding, under otherwise identical experimental conditions. We therefore believe that the sliding-spallation test highlights an important aspect of concrete-ice abrasion; that sharp ice fragments play an important role when ice is wearing on the concrete surface.

Further research of concrete-ice abrasion at our laboratory will include:

- investigation of different types of concrete, including light weight concrete and repair mortar;
- investigation of sliding and impact effect on concrete-ice abrasion depth;
- studying of initial concrete surface topography on resulting concrete-ice abrasion;
- studying of concrete-ice abrasion in combination with frost deterioration on air and non-air entrained samples.

ACKNOWLEDGMENT

REFERENCES

1. Huovinen, S., Abrasion of concrete structures by ice. Cement and Concrete Research, 1993. 23(1): p. 69-82.
2. Bekker, A.T., et al. Experimental study of concrete resistance to ice abrasion. in Proceedings of the 21st International Offshore and Polar Engineering Conference. 2011.
3. Hanada, M., et al. Abrasion rate of various materials due to the movement of ice sheets. in Proceedings of the 6th International Offshore and Polar Engineering Conference. 1996.
4. Fiorio, B., Wear characterisation and degradation mechanisms of a concrete surface under ice friction. Construction and Building Materials, 2005. 19(5): p. 366-375.
5. Møen, E., et al., Experimental study of concrete abrasion due to ice friction - Part I: Set-up, ice abrasion vs. material properties and exposure conditions. Cold Regions Science and Technology, 2015. 110: p. 183-201.
6. Tijsen, J., S. Bruneau, and B. Colbourne. Laboratory examination of ice loads and effects on concrete surfaces from bi-axial collision and adhesion events. in Proceedings of the International Conference on Port and Ocean Engineering under Arctic Conditions, POAC. 2015.

7.   Itoh, Y., et al., Abrasion depth distribution of a cylindrical concrete structure due to sea ice movement. International Journal of Offshore and Polar Engineering, 1996. 6(2): p. 144-151.

8.   Jacobsen, S., G.W. Scherer, and E.M. Schulson, Concrete-ice abrasion mechanics. Cement and Concrete Research, 2015. 73: p. 79-95.

9.   Løset, S., K. Shkhinek, and K.V. Høyland, Ice Physics and Mechanics. 1998: NTNU.

10.   Timco, G.W., Indentation and Penetration of Edge-Loaded Freshwater Ice Sheets in the Brittle Range. Journal of Offshore Mechanics and Arctic Engineering, 1987. 109(3): p. 287-294.

11.   Sodhi, D.S., Crushing failure during ice-structure interaction. Engineering Fracture Mechanics, 2001. 68(17-18): p. 1889-1921.

12.   Browne, T., et al., Small-scale ice indentation tests with variable structural compliance. Cold Regions Science and Technology, 2013. 88: p. 2-9.

13.   Jacobsen, S., L.V. Kim, and E.E. Pomnikov. Concrete destructure due to ice-indentation pore pressure. in Proceedings of the 22nd International Offshore and Polar Engineering Conference. 2012.

14.   Hara, F., et al., Prediction of the Degree of Abrasion of Bridge Piers by Fresh Water Ice and the Protective Measures, in Concrete Under Severe Conditions Environment and Loading. 1995. p. 482-494.

15.   Møen, E., et al., Experimental study of concrete abrasion due to ice friction - Part II: Statistical representation of abrasion rates and simple, linear models for estimation. Cold Regions Science and Technology, 2015. 110: p. 202-214.

16.   Hara, F., Y. Takahashi, and H. Saeki, Evaluation of test methods of abrasion by ice movements on the surface of reinforced concrete structures, in Concrete Under Severe Conditions Environment and Loading. 1995. p. 475-484.

17.   Saeki, H., et al., Coefficient of Friction Between Sea Ice And Various Materials Used in Offshore Structures. Journal of Energy Resources Technology, Transactions of the ASME, 1986. 108(1): p. 65-71.

18.   Hoff, G.C. Evaluation of ice abrasion of high-strength lightweight concretes for arctic applications. in Proceedings of the 8th International Conference on Offshore Mechanics and Arctic Engineering. 1989.

19.   Itoh, Y., et al., An experimental study on abrasion of concrete due to sea ice. In: Otc 88 Proceedings 20th Annual Offshore Technology Conference, 1988: p. 61-68.

20.   Kirkhaug, J.R., Ice Abrasion and Bond Testing of Repair Mortars and High Performance Concrete. 2013, Norwegian Univercity of Science and Technology. p. 114.

21.   Tijsen, J.N.W., Experimental study on the development of abrasion at offshore concrete structures in ice conditions. 2015, Delft University of Technology. p. 133.

22.   Shamsutdinova, G., M. Hendriks, and S. Jacobsen. Concrete-Ice Abrasion: Surface Roughness and Measurement Method. in The 5th International Conference on Construction Materials: Performance, Innovations and Structural Implications. 2015. University of British Columbia Vancouver.

23.   12350-1, E., Testing fresh concrete. Sampling. 2009.

24.   NS-EN 206:2013+NA:2014, Concrete -Specification, perfomance, production and conformity. National annex. 2014.

25.   Archard, J.F., Contact and rubbing of flat surfaces. Journal of Applied Physics, 1953. 24(8): p. 981-988.

26.   Basu, B. and M. Kalin, Tribology of Ceramics and Composites : Materials Science Perspective. Tribology properties of ceramics and composites. 2011, Hoboken: Wiley.

27. Itoh, Y., Y. Tanaka, and H. Saeki. Estimation method for abrasion of concrete structures due to sea ice movement. in Proceedings of the 4th International Offshore and Polar Engineering Conference. 1994.
28. Bekker, A.T., T.E. Uvarova, and E.E. Pomnikov. Calculation of ice abrasion for the lighthouses installed in the Gulf of Bothnia. in Proceedings of the 21st International Conference on Port and Ocean Engineering under Arctic Conditions, POAC. 2011.
29. Stachowiak, G.W., Wear : materials, mechanisms and practice. 2005.
30. Fiorio, B., J. Meyssonnier, and M. Boulon, Experimental study of the friction of ice over concrete under simplified ice-structure interaction conditions. Canadian Journal of Civil Engineering, 2002. 29(3): p. 347-359.
31. Schulson, E.M., Low-speed friction and brittle compressive failure of ice: Fundamental processes in ice mechanics. International Materials Reviews, 2015. 60(8): p. 451-478.
32. Ramos, N., et al., Lattice modelling of the onset of concrete-ice abrasion, in 8th International Conference on Concrete under Severe Conditions - Environment and Loading. 2016. p. 351-358

Behaviour and Capacity of Lightweight Aggregate Concrete Beams with and without Shear Reinforcement

Jelena Zivkovic, Ph.D Student
Department of Structural Engineering
Faculty of Engineering Science
Norwegian University of Science and Technology
7491 Trondheim, Norway
E-mail: jelena.zivkovic@ntnu.no

Jan Arve Øverli
Professor, Ph.D
Department of Structural Engineering
Faculty of Engineering Science
Norwegian University of Science and Technology
7491 Trondheim, Norway
E-mail: jan.overli@ntnu.no

ABSTRACT

The main disadvantages of lightweight aggregate compared with normal weight concrete are its brittleness at the material level in compression and uncontrolled crack propagation. This experimental investigation consists of five beams with lightweight concrete with Stalite as aggregate. Main goals were to investigate behaviour and capacity of the beams with and without shear reinforcement subjected to four-point bending test and compare those results with previous experimental work. The main test parameters were the shear span ratio (a/d) and amount of the shear reinforcement. Existing standards underestimate shear capacity because they do not differ between shear span (a). Tested beams were more ductile than expected, and cracking was similar as for normal weight concrete beams. According to this experimental investigation, the shear capacity in beams without shear reinforcement should be based on inclined cracking loads.

Keywords: Lightweight aggregate concrete, testing, shear reinforcement, bending, ductility.

1.   INTRODUCTION

This investigation is part of the ongoing research programme, "Durable advanced concrete structures (DACS)". One part of this programme is to investigate the structural behaviour of lightweight aggregate concretes (LWAC), i.e. concretes with an oven-dry density below 2000 kg/m^3. A general characteristic of LWAC is its very high degree of brittleness at the material level and especially in compression, which results in sensitivity to stress concentrations and rapid crack/fracture development. This influences the behaviour of concrete where its tensile strength is important, as for instance with its shear and bond strength. To investigate the behaviour of LWAC, beams with and without shear reinforcement were subjected to a four-point bending test. The main test parameters were the shear span length to effective height ratio (a/d) and amount of shear reinforcement. For all beams, the shear loads at diagonal cracking and at failure were plotted as a function of the a/d ratio and compared with previous experimental work. For comparison, tested beams were of the same size and with the same area of compression and tension reinforcement as in earlier shear tests on other normal density (ND)

and lightweight aggregate (LWA) concrete beams [1,2]. In addition small specimens were used to find the compressive strength [3, 4], splitting tensile strength [5], Young's modulus [6, 7], and fracture energy [8].

To produce the concrete, a lightweight aggregate Stalite was used to achieve an oven-dry density of about 1850 kg/m^3 and a compressive strength of about 65 MPa. Agreggate Stalite is the argillite slate, laminated, fine-grained siltstone of clastic rock. The foothills region of North Carolina is the only place where slate is exhausted as raw material to produce Stalite. The bulk density ranges from 720-1120 kg/m^3 for both coarse and fine aggregate and the hardness of the material is equivalent to that of the quartz [9, 10].

2.   EXPERIMENTAL TEST PROGRAM AND RESULTS

2.1   Test specimens

Five reinforced LWA concrete beams with and without shear reinforcement were tested in a four point bending test. The loading system was designed to produce a constant moment in the middle part of the beam. The cross section (*bxh*) of the beams was 150x250 mm and the length 2900 mm. The main test parameters that were warried in this test were the shear span length to effective height ratio (*a/d*) and amount of shear reinforcement. In the ratio *a/d*, *a* is the shear span (the length between loading point and support) and *d* the effective height of the cross section (the distance from the top surface to the centre of the tensile reinforcement), which in this case is 219 mm. Two pairs of beams without shear reinforcement each with shear span ratio *a/d*=2.3 and *a/d*=4.0 were tested. In addition one beam, which contained shear reinforcement distributed between the support and loading point and with shear ratio *a/d* =3.43 was tested. An overview of the test programme is shown in Table 1.

Table 1-The main test parameters

Beam	*a* [mm]	*d* [mm]	*a/d* [-]	A_c [cm^2]	A_t [cm^2]	*s* [mm]	$f_{lc,cyl}$ [MPa]	A_t / (*bxd*) [%]
1	504	219	2.3	1.57	6.03	-	67.5	1.83
2	504	219	2.3	1.57	6.03	-	67.5	1.83
3	876	219	4	1.57	6.03	-	67.5	1.83
4	876	219	4	1.57	6.03	-	67.5	1.83
5	750	219	3.43	1.57	6.28	100	67.5	1.91

Where a is shear span; d is effective hight; a/d is shear span ratio; A_c – area of compresive reinforcement; A_t – area of tensile reinforcement; s is stirrup spaceing; f_{lc,cyl}-compressive cylinder strength.

All the beams had three ø8 mm stirrups in each anchorage zone (behind the supports). Beams without shear reinforcement had just two stirrups in the constant moment region below applied forces, while there were no stirrups in the shear spans. One of the tested beams contained shear reinforcement distributed along the shear span. Reinforcement on the tension side consisted of three ø16 mm bars in beams with shear span ratio *a/d* =2.3 and 4.0 and beam with *a/d* =3.43 had two ø20 mm bars. As compressive reinforcement, two ø10 mm bars were used in all the beams. Longitudinal and cross section details of the beam specimens are shown in Figure 1.

All the beams and small samples, cubes and cylinders, were cast from the same concrete batch. The beams were demoulded 24 hours after casting and further cured in the laboratory under wet burlaps covered with a plastic sheet. Two days before the testing beams were taken out and

prepared for instrumentation. Finally, the beams were painted white for easier detection of cracks.

Small samples, which were cast in order to identify the mechanical properties of the LWAC, included 12 cubes (with dimensions 100x100x100 mm), 15 cylinders (ø100x200mm) and 3 small beams (100x100x1200mm). From mentioned samples, the authors derived the stress-strain diagram, compressive strength for cube and cylinder, tensile strength, Young's modulus of elasticity and fracture energy. All small specimens were demolded after 24 hours and kept in water until testing day. Compression test on cubes and cylinders were carried out in the start, middle and last day of beam testing.
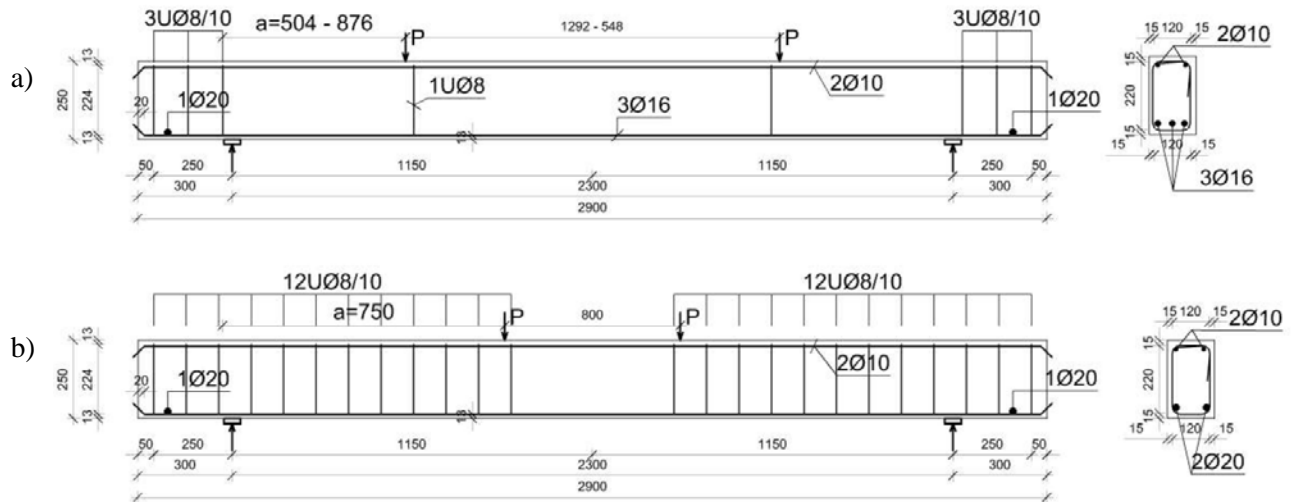
Figure 1 – Reinforcement and cross section details for the beams a) without and b) with shear reinforcement

2.2 Material and mix properties

The concrete mixture was prepared from one batch. The lightweight aggregate was the ½" fraction from Stalite [11]. The moisture content and the absorbed water in the Stalite were measured, which was necessary input when designing the concrete mix [12, 13]. The moisture content was 8.2%, and the absorption after 24 hour and 100 hours was 6 % and 8.5%, respectively. Table 2 gives the concrete mixture.

Table 2 – Concrete mixture for LWAC 65

Constituent	Weight [kg/m^3]
Cement (Norcem Anlegg)	398.21
Silica fume (Elkem Microsilica)	19.62
Water (free+absorbed 24 hour)	93.87+40.12=134
Sand (Årdal (NSBR) 0/8 mm)	745.56
Aggregate (Stalite 1/2")	618.79
Superplasticiser (Sika ViscoCrete RMC-420)	3.20

The mixing was done using a 0.8 m^3 laboratory mixer. First cement, silica fume, Stalite and sand were mixed for approximately 2 min. Water and superplasticiser were continuously added and adjusted during mixing, until the desired workability of the concrete was achieved.

Characteristics of the fresh concrete were: density 1990 kg/m^3, air content 2.6 % [14] and slump 140 mm [15]. The reinforcement was of the type B500NC [16]. The yielding stress of the reinforcement assumed in calculation is approximately 560 MPa.

2.3 Test Setup and procedure

The load was applied with a mechanical screw jack and was transferred to the test beam through a steel spreader beam, which was supported, on two steel rollers covering the entire width of the beam. The loading point has free rotation transversal to the beam. Between jacks and the beam surface, it was used 50 mm wide steel plates and a 15 mm thick fibreboard with the same width. The supports were both free for rotation and displacement in the longitudinal direction. At the supports, only steel plate was between the support and the beam. The supports were placed 300 mm from the beam-ends. To avoid anchorage problems, short ø20 mm reinforcement bars were welded to the tensile reinforcement in this region. The load was measured using electrical load cell under the screw jack of maximum capacity 1000 kN. Instrumentation set-up differs between beams with and without shear reinforcement. Figure 2 shows the layout of the test set-up for the beams with and without shear reinforcement and view from the laboratory.
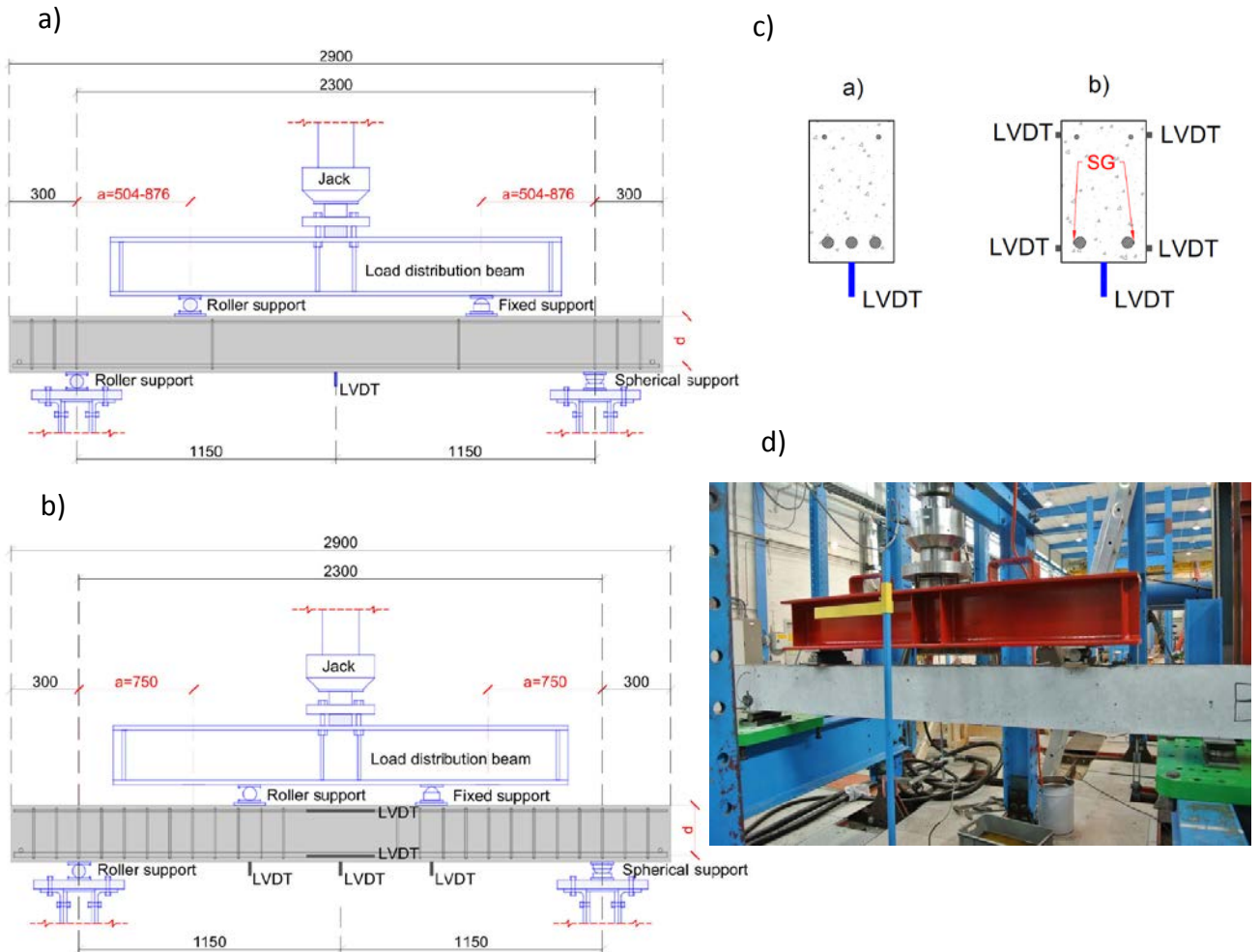
Figure 2 – Test set-up off beams a) without shear reinforcement; b) with shear reinforcement; c) detail middle cross section for beam without and with shear reinforcement; d) view from the laboratory.

For observation of beam with shear reinforcement, more instrumentation was used. Linear Variable Displacement Transducers (LVDT) measured the deflections in the middle of the beam span in all the beams. In beam with shear reinforcement additional LVDT were used for measuring deformations under the loading points and over the middle cross section. Length of LVDT for observation of middle section was 200 mm. In addition, in this beam strain gauges (SG, type FLA-6-11-5L with gauge resistance of 119,5±0.5Ω) were inserted on the tensile reinforcement inside of the middle cross section. All measuring devices (LVDTs and SGs) together with the load cell were connected to HBM eight channel spider to record the data. From here, data were sent to computer using a specific software program, where they are processed and stored in a text file.

The load was applied stepwise in increment of 20 kN for the beams without shear reinforcement until failure. For the beam 5, with shear reinforcement, an increment of 40 kN was used since calculated capacity was doubled. The first tested beam was beam 1, one of two beams with shear span ratio 2.3. This beam was tested with loading steps of 10 kN. Since there was too many steps and testing takes, more than 2 hours loading steps were increased on 20 kN for the next beam with 2.3 ratio and for the two beams with 4.0 ratio. This is displacement control test with loading rate 0.5 mm/minute for the beams without shear reinforcement and 1 mm/minute for beam with shear reinforcement. The deflection measurements were carried out as a control. At each step, deflections in the middle section and under the loading points were measured. The loading time for each step takes about 10 minutes, from what 5 minutes was break and mainly used to draw the crack progression with dark pen. The output data were recorded by the data acquisition system. Pictures were taken after each step and failure.

3.   EXPERIMENTAL RESULTS

3.1   Results for small specimens

Concrete class measured from small samples was LC65 and that actually represents high strength lightweight concrete. The compressive failures of cubes and cylinders were very explosive which is typical for high strength and lightweight concrete.

Small specimens were tested after 28 days for determination of compressive strength, 29 days for tensile strength and Young's modulus. Small beams for fracture energy were tested after 36 days. A brief summary of the small scale test results is given in Table 3.

<p align="center">Table 3 – Mechanical properties for LWAC</p>

Saturated density	$\rho_{cs} = 1980$ kg/m3
Oven dry density	$\rho_{cv} = 1850$ kg/m^3
Compression cube after 7 days	$f_{lcm,7} = 57{,}3$ N/mm^2
Compression cube after 28 days	$f_{lcm,28} = 73{,}8$ N/mm^2
Compression cylinder	$f_{lcm} = 67{,}5$ N/mm^2
Tensile strength	$f_{lctm} = 4{,}05$ N/mm^2
Modulus of elasticity	$E_{lcm} = 24175$ N/mm^2
Fracture energy	$G_F = 76{,}7$ Nm/m^2

3.2 Capacity of the beams

Table 4 shows the results of the tested beams. In the table, the following forces are plotted: the forces when the first bending crack occurred (P_{fcr}), force of diagonal cracking (P_{cr}) and failure force (P_u). The shear capacity ($P_{calc}=V_{Rd,c}$) for both pairs of the beams without shear reinforcement was calculated according to Eurocode 2 [17, 18, 19] and Norwegian standard NS 3473 [20, 21] and those values were 42.8 kN and 44.6 kN, respectively. Calculation of shear capacity according to both standards was influenced by external load but position of the load was not taken into account, which resulted with the same capacity for the beams with shear span ratio 2.3 and 4. Calculated shear capacity for all the tested beams plotted in the table 4 was according to Eurocode 2 [17, 18, 19]. Shear capacity according to Eurocode 2 for the beam 5 which contain shear reinforcement was almost doubled and that value is 92.85 kN. Shear capacity for beam with ratio 2.3 and 4 was also calculated according to Norwegian standard NS 3473 and that value was plotted in table 5. Reason for this is that all previous results for comparison were calculated by using the same standard NS 3473. Tensile strength used in this calculation is obtained from small scale testing [5] and later interpolated according to NS 3473. For lightweight concrete the values are multiplied by a reduction factor $(0,30+0,70\rho/\rho_1)$, where ρ is the dry density of the lightweight concrete and $\rho_1=2400$ kg/m^3. Hence, with a dry density of 1850 kg/m^3 the reduction factor was 0,839.

The beams were tested 30 days (beam 1_ with shear ratio 2.3), 31 days (2_2.3), 34 days (3_4.0 and 4_4.0) and 35 days (5_3.43) after casting.

Table 4-Test parameters and results of first cracking, diagonal cracking, failure loads and calculated shear capacity in accordance with EC2[17,18]

Beam	a [mm]	d [mm]	a/d	P_{fcr} [kN]	P_{cr} [kN]	P_u [kN]	P_{calc} [kN]	P_{cr}/P_{calc}	P_u/P_{calc}
1	504	219	2.3	25	45	92.3	42.8	1.05	2.15
2	504	219	2.3	22.5	44.5	127.2	42.8	1.04	2.97
3	876	219	4	21	36.8	44.4	42.8	0.86	1.04
4	876	219	4	21	33	62	42.8	0.77	1.44
5	750	219	3.43	25	40	91.4	92.85	0.43	0.98

In all the beams first cracking started for approximately, same load level of 21-25 kN. Formation of the first shear diagonal cracks depend and differs from the shear span ratio. So in the beams with higher shear span ratio shear cracks formed for lower load level, while by reducing shear span (a), distance between loading point and support , shear capacity increased.

3.3 Load-deformation relationship

The load–deformation relationship was followed during the entire test. Figure 3 shows the load-deformation relationship for the centre point of the cross section at middle span for all the five beams. As expected, beams that do not contain shear reinforcement along the shear span and with low shear span ratio 2.3, had higher capacity. Beam 2, with shear span ratio 2.3 had even higher capacity than the beam 5 that contain shear reinforcement. The resemblance between two identical beams is quite good before failure. As expected, the response depends on the shear span ratio. With a low ratio a concrete strut forms making a direct load transfer of the point load to the support. The load and deformation can increase several times the shear cracking load.

However, the ultimate load is more unpredictable in this case. For a high shear span ratio, pure shear governs the failure mode. The failure loads for these two beams can be defined to be the same. Beam 4 with shear span ratio 4.0 was able to sustain a higher load after significant deformations, but it is not possible to rely on such deformations in a design situation. As expected the beam with shear reinforcement showed significant ductility, deflections are doubled for the same load level and before failure this beam were able to sustain even increase of loading. In addition, one of the beam with shear span ratio 2.3 showed very ductile behaviour. In general, all the tested beams are in the very good agreement considering the main test parameter shear span ratio.
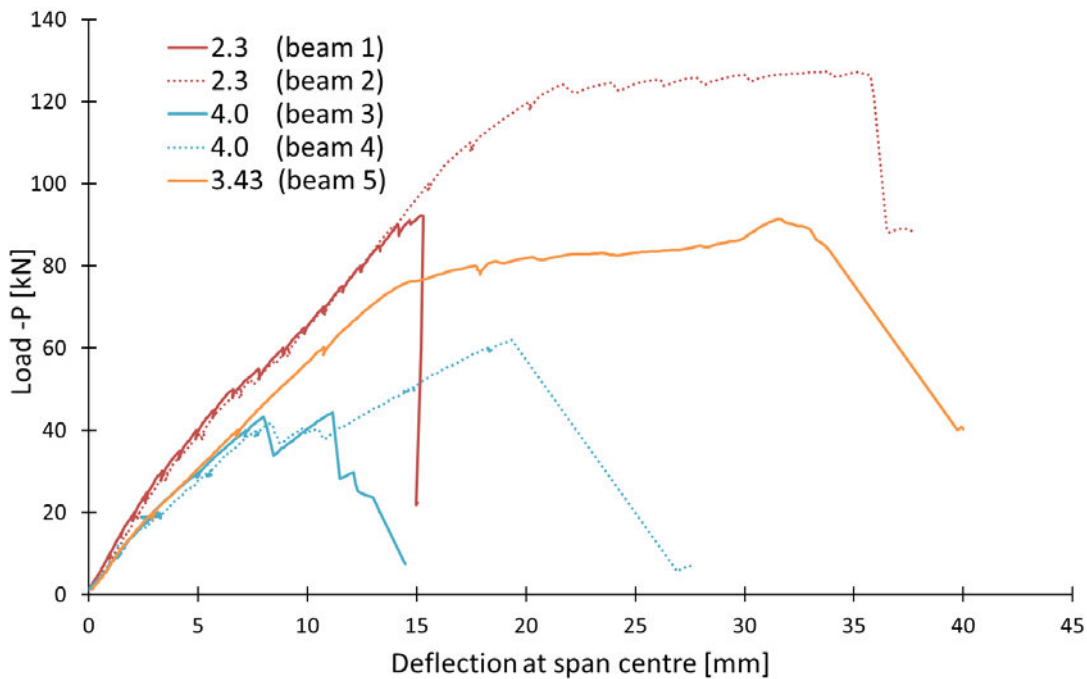
Figure 3 – Load deflection curves for all the tested beams

Results of strain distribution were observed and recorded over the middle cross section just in beam 5 with shear ratio 3.43. Since those results cannot be compared with first four tested beams 1-4. they are not plotted here.

4.   DISCUSSION

4.1   Failure modes, cracking patterns and capacity of the beams

The first cracks in all beams started to develop in the constant moment region, between the loading points, on the tension side for load levels between 20 and 40 kN, depending on the *a/d* ratio. As load increased cracks formed along the entire length of the constant moment region and wider. When flexural bending cracks stopped to develop, suddenly, the diagonal shear cracks occurred, but the beams did not fail immediately. The beams with *a/d* ratio of 2.3 formed directly the diagonal inclined shear crack. These cracks appeared suddenly developing from the tension side of the beam towards the compression side near the point loads. For beams with ratio 2.3 diagonal cracks formed at higher load levels than for beams with ratio 4.0. For beams with ratio 4.0 the diagonal shear cracks propagated from one of the flexural bending cracks at the

(a) Shear span ratio 2.3 - beam 1
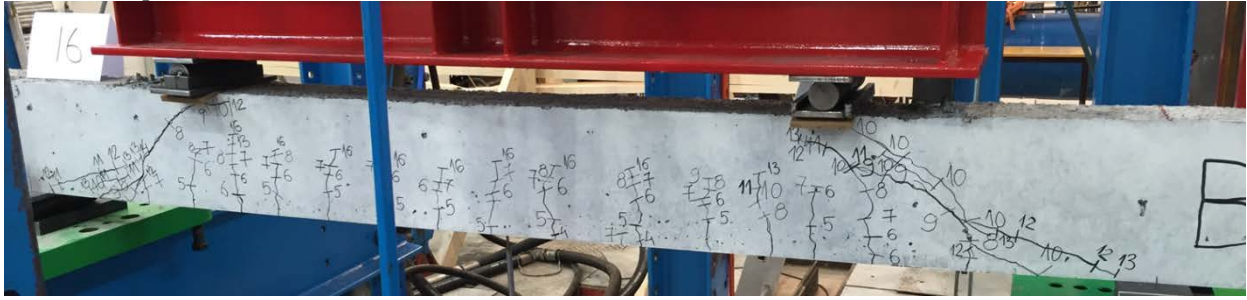
(b) Shear span ratio 2.3 - beam 2
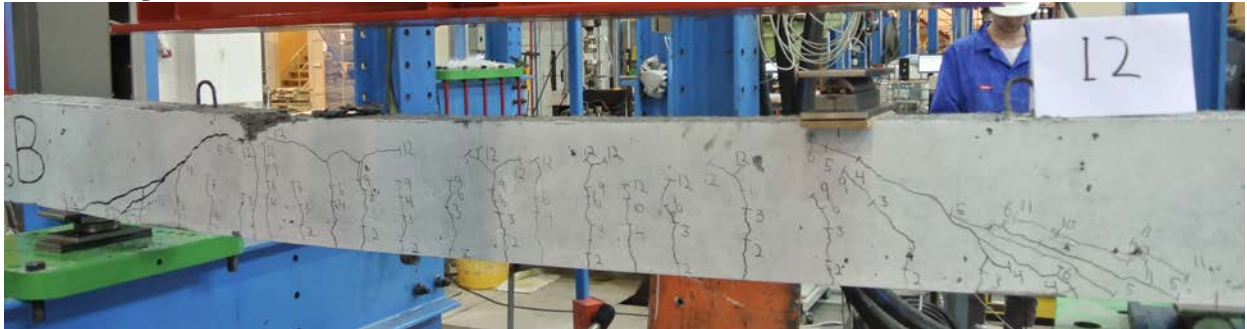
(c) Shear span ratio 4.0 - beam 3

(d) Shear span ratio 4.0 - beam 4

(d) Shear span ratio 3.43 – beam 5

Figure 4 – Final failure state for beams (a) 2.3-1; (b) 2.3-2; (c) 4.0-3; (d) 4.0-4 and (e) 3.43-5

tension side. For beams with shear reinforcement and shear span ratio 3.43 cracking started from the tension side. Location of cracks depends from reinforcement layout. Flexural bending cracks start to form between stirrups. Later diagonal shear cracks propagated from flexural bending cracks. For a certain load level propagation of diagonal cracks was stopped due to shear reinforcement while propagation of bending cracks were continued. At the end, bending cracks led to failure in beam with shear reinforcement, while in beams without shear reinforcement diagonal shear cracks lead to failure. Figure 4 showed the final failure state of all the tested beams.

In general, beams with lowest shear span ratio had higher capacity, see Table 4. Formation of cracks for beams with ratios 4.0 and 3.43 was equal in both shear spans. For beams with ratio 4.0 failure happened suddenly in one of the shear span, while beam with ratio 3.43 failed in compression between the loading points. In the beams with ratio 2.3 shear cracking was more non-symmetrical, with more and larger cracks at one end of the beam, and beams failed at the shear span.

Failure that happened between support and the loading point, shear zone, is defined as shear tension failure or shear compression failure depending which zone cracked [22, 23]. Here we can notice that beams with ratio 2.3 in the final failure phase cracked always under the loading points so they had shear compression failure. In beams with ratio 4.0 development of cracks on a tension shear zone were wide, cracks followed tensile reinforcement, and they even continued in anchorage area, so they had shear tension failure.

Behavior of beam with ratio 3.43 in beginning matches well with beams with ratio 4.0. However, due to shear reinforcement this beam had approximately double jump in capacity and at the end cracking of compression zone between loading point happened. This type of failure can be defined as bending compression failure [22, 23].

In general, cracking and failure mechanism for beams without web shear reinforcement, which is typical for NWC, is that crack will appear in the shear span by increasing the load. Owing to the presence of the shear stresses, they bend towards the axis of the beam. Other secondary cracks due to stress redistribution may also appear. The development of the diagonal cracks stops at a certain load level, while the crack propagating into the compression zone. The beam either collapses simultaneously with the appearance of this diagonal crack or continue to sustain higher load until crushing the concrete in the compression zone. The term diagonal crack load is in this work defined as the load when the formation of the specific shear crack happened, which later develops into shear failure. The load for which the testing beam collapses is the ultimate load or load carrying capacity [24, 25, 26].

Due to the brittle nature for LWAC it is typical that diagonal cracking load is equal to ultimate load. However, after formation of diagonal cracks in this experiment beams were able to carry an increase the loading [26, 27]. The cracks propagated almost horizontally along the tensile reinforcement and diagonally into the compression zone. In some cases the cracks even passed the loading point and into the constant moment region. In the final stage, the shear cracks opened widely together with sliding along of the diagonal cracks and resulted in crushing of the concrete close to the loading point, see Figure 4. In the beam that contained shear reinforcement formation of cracks have determined by reinforcement layout and for the certain load level development of shear cracks is limited and stopped with shear reinforcement. This resulted in significant increase in capacity and contribute to ductile behavior of the beam. Even this as all

the tested beams are from lightweight aggregate concrete, this beam was able to withstand increase of loading in final failure phase.

4.2   Comparison with previous experimental work

Similar tests have earlier been carried out for higher strength concrete classes of normal density and lightweight aggregate concretes. Table 5 shows a comparison of these tests with the present investigation tests with $a/d = 2.3$ and with $a/d = 4.0$ for the beams without shear reinforcement. Beam with shear span ratio 3.43 is out of the comparison since this beam contained shear reinforcement. In all previous investigation the tests conditions were the same, including the rig, the cross section and the amount and distribution of reinforcement [1,2]. Shear capacity for all the previously tested beams were calculated according to Norwegian standard NS 3473 [20, 21]. Because of the comparison shear capacity for the beams with shear span ratio 2.3 and 4 was also calculated according to the same standard and that value was 44.6 kN. Again all the beams without shear reinforcement have the same capacity since standard in calculation of the shear capacity do not include the load position.

The concrete types compared with previous investigations are ND65, ND95, LWA75, LWA40 and LWAC_Leca. The ND65 and ND95 concretes had normal density aggregates from Årdal with maximum aggregate size 16 mm. The mean cylinder strengths of these concretes were 54 and 78 MPa and the dry density was between 2300 and 2350 kg/m^3.

The LWA75 concrete had natural sand (0-4 mm) and Liapor 8 (lightweight aggregate [28, 29]) in the coarse fraction from 4 to16 mm. The mean cylinder strength of this concrete was 58 MPa and the dry density about 1900 kg/m^3. The LWA40 had natural sand (0-4 mm) and Leca 700 aggregate (4-16 mm), while LWAC_Leca also had Leca but several fractions (Leca sand (0-4 mm, crushed), Leca sand (2-4 mm, round), Leca 7 (4-8 mm) and Leca 7 (8-12 mm)). The mean cylinder strengths of these concretes were 37 and 42,7 MPa, and the dry densities about 1600 and 1320 kg/m^3, respectively [1]. For all of these concretes capacity was calculated according to NS3473 (P_{calc}).

The results of main interest for this comparison is the ratio between the observed shear diagonal cracking load and calculated capacity and also ratio between obtained failure load and capacity.

Table 5 - Comparison of the shear strengths for beams with a/d = 2.3 and 4.0, shear capacity is calculated in accordance with NS3473[20]

Beam/Aggregate	a/d	$f_{lc,cyl}$ [MPa]	P_{cr} [kN]	P_u [kN]	P_{calc} [kN]	P_{cr} / P_{calc}	P_u / P_{calc}
1/Stalite	2.3	67.5	45	92.3	44.6	1.01	2.07
2/Stalite	2.3	67.5	44.5	127.2	44.6	1.00	2.85
ND65/Årdal	2.3	54	62.2	71.6	55.1	1.13	1.30
ND95/Årdal	2.3	78	66.7	103.5	57.3	1.16	1.81
LWA75/Liapor 8	2.3	58	47.1	126.1	52.0	0.91	2.43
LWA40/Leca	2.3	37	46.6	77.9	39.3	1.19	1.98
LWA_Leca_mix	2.3	42.7	34.3	102.9	42.1	0.81	2.44
3/Stalite	4	67.5	36.8	44.4	44.6	0.82	0.99
4/Stalite	4	67.5	35	62	44.6	0.78	1.39
LWA40/Leca	4	37	38.2	38.2	39.30	0.97	0.97
LWA_Leca_mix	4	42.7	29.4	44.1	42.10	0.70	1.05

where a/d is shear span ratio; $f_{lc,cyl}$-compressive cylinder strength; P_{cr} – load level for first shear crack; P_u – load level of maximum load; P_{calc}– calculated shear capacity acoording to Norwegian standard NS3473 [20].

For beams with a/d = 2.3, the ratio between shear diagonal cracking load and calculated load was larger or equal to 1.0 for all concretes except LWA75 and LWA_Leca_mix. This indicates that they are on the conservative side. For LWA75 and LWAC_Leca_mix, this ratio was less than 1.0, indicating a higher drop in shear strength than predicted by NS 3473. The ratio between ultimate load and calculated one for all LWA concretes was almost 2 or higher, which shows that LWA concretes in general can withstand more loading than predicted by standards. For normal density concretes, this ratio was lower. In general, it is obvious that shear capacity calculated by standards is significantly underestimated compared with experimental results.

It can be observed that the ultimate load capacity for the beams 1and 2 with shear span ratio 2.3 was slightly higher than for the beams with normal weight concretes ND65 and ND95. This result was expected because LWAC concrete with Stalite as aggregate have the same behaviour as normal weight concrete. Slightly higher ultimate load than for normal weight concrete might be result of stronger transition zone between the aggregate and the matrix, which result in cracking development around and trough lightweight aggregate.

The ND65, ND95 and LWA75 concretes were not tested with ratio *a/d* = 4.0. For beams with *a/d* = 4.0, the ratio between shear diagonal cracking load and calculated load for both concretes tested was below 1.0 – indicating that beams with *a/d* = 4.0 had a certain drop in capacity [1,12]. The ratio between ultimate load and calculated one for all the beams is around or higher than 1.0 – indicating that standards are applicable for larger shear span ratios. In general, calculation by standards matches well with experimental results for the beams with ratio 4.0. The same can be noted from the Table 4 for the beam 5 with ratio *a/d* = 3.43, where the ultimate capacity predicted by standard matches well with experimental one.

For tested LWA concrete with Stalite as aggregate, the diagonal cracking load was close to other lightweight aggregate concretes, while the failure load was higher, especially in the case of *a/d* = 4.0.

In comparison with normal density concretes ND65 and ND95, the diagonal cracking load for normal concretes was approximately 30% higher, while failure load for LWAC with Stalite was significantly higher.

Actually, from this experimental investigation from high importance is the fact that after shear diagonal crack were formed beams can withstand increase of load from 30 to 50 %, which is of great importance having in mind that here is tested lightweight aggregate concrete. In addition, by introducing the shear reinforcement in beams with very similar shear span ratio, 4.0 and 3.43, ultimate capacity will increase and nature of failure differ from shear failure to bending failure.

5. CONCLUSIONS

For all tested beams in this experiment, the shear stress at inclined cracking of the beams decreased with an increase in the shear span to effective height ratio (*a/d*). Cracking propagation in the tested beams showed that they were more ductile than expected, which should promote increased investigation and structural use of this type of LWAC. Beam with shear reinforcement showed significant ductility compared to other tested beams.

For beams with larger shear span ratio (3.43 and 4.0) calculations predicted by standards, match well with experimental results, while standards underestimate a lot ultimate capacity in beams with lower sheer span ratio (2.3). Calculation of the shear capacity according to existing standards do not take into account position of the load, shear span a. Standards just differ between the beams congaing or not shear reinforcement. According to this experimental investigation, the design strength for shear in beams and slabs without shear reinforcement should be based on inclined cracking loads.

Comparison with similar tests on other types of lightweight concretes and normal density concretes showed the same that the shear stress at inclined cracking of the beams decreased with an increase in shear span ratio (*a/d*). For concretes tested in this experiment and in previous investigation ratio between the load observed at diagonal cracking and the predicted strengths was in the same range. However, the ratio between observed load at failure and the strengths predicted was significantly higher for the lightweight concrete used in this investigation.

6. FURTHER RESEARCH

During this experimental work was observed that the load-carrying capacity of LWAC members is very similar to that of corresponding ND concrete members. The high strength-to-weight ratio of LWAC compared to ND concrete means that increased use of the material in structural applications would be both economical and environmentally friendly. In the continuation of this project, a better understanding of the ultimate behaviour of LWAC in compression and bending by varying different reinforcement detailing will be of main interest.

ACKNOWLEDGMENT

REFERENCES

1. Thorenfeldt E & Stemland H: "Shear capacity of lightweight concrete beams without shear reinforcement". *Proceedings,* International Symposium on Structural Lightweight Aggregate Concrete, Sandefjord, Norway, 20-24 June 1995, pp. 244-245.
2. Zivkovic J & Øverli J A: "Shear capacity of lightweight concrete beams without shear reinforcement". *Proceedings*, Eleventh High Performance Concrete & Second Concrete Innovation Conference, Tromsø, Norway, 2017.
3. NS-EN 12390-3:2009. "Testing hardened concrete - Part 3: Compressive strength of test specimens". Standard Norge, Lysaker, Norway, 2009.
4. Watanabe K, Niwa J, Yokota H & Iwanami M: "Experimental Study on Stress Strain Curve of Concrete Considering Localized Failure in Compression". *Journal of Advanced Concrete Technology*, Vol. 2, No.3, 2004, pp. 395-407.
5. NS-EN 12390-6:2009. Testing hardened concrete - Part 6: Tensile strength of test specimens. Standard Norge, Lysaker, Norway, 2009.
6. Skjølsvold O, Bakken N & Johansen E: "KS 14-05-04-122: Bestemmelse av E-modul iht NS3676 Losenhausen 5000kN trykkpresse." SINTEF Byggforsk: Betong og natursteinslaboratooriene; Trondheim, Norway, 2007.
7. NS 3676. "Concrete testing - Hardened concrete - Modules of elasticity in compression". Standard Norge, Lysaker, Norway, 1987.
8. Hillerborg A; "The theoretical basis of a method to determine the fracture energy GF of concrete",RILEM Technical Committees, *Materials and Structures*, Vol. 18, No. 4, July 1985, pp. 291-296.
9. Castrodale R W, Zivkovic J & Valum R: "Material Properties of High Performance Structural Lightweight Concrete". *Proceedings*, Eleventh High Performance Concrete & Second Concrete Innovation Conference, Tromsø, Norway, 2017.
10. EuroLightCon. "LWAC Material Properties". Document BE96-3942/R2, December 1998.
11. TEC Services. Interim report of ASTM c330 Carolina Stalite 0, 5 inch coarse lightweight aggregate. TEC Services Project No: 04-0514, TEC Services Sample ID: 14-999, 2015.
12. ACI Committee 213. "Guide for Structural Lightweight Aggregate Concrete" (ACI 213R-03). American Concrete Institute. Farmington Hills, MI, USA, 2003.
13. Yong G E, Kong L, Zhang B & Jie Y: "Effect of Lightweight Aggregate Pre-wetting on Microstructure and Permeability of Mixed Aggregate Concrete". *Journal of Wuhan University of Technology-Mater*. Sci. Ed. Vol 24, No. 5, October 2009, pp. 838-842.
14. NS-EN 12390-7:2009. "Testing hardened concrete - Part 7: Density of hardened concrete". Standard Norge, Lysaker, Norway, 2009.
15. Methods for Testing Fresh Lightweight Aggregate Concrete (Document BE96-3942/R4, December 1999).
16. NS 3576-3:2012. "Armeringsstål - mål og egenskaper - del 3: Kamstål B500NC". Standard Norge, Lysaker, Norway, 2012.

17. EN 1992-1-1 (2004). "Eurocode 2: Design of concrete structures – Part 1 -1: General rules and rules for buildings".
18. NS-EN 1992-1-1:2004+NA: 2008. "Eurocode 2: Design of concrete structures – General rules and rules for buildings". Standard Norge, Lysaker, Norway, 2008.
19. Sørensen S I: "Betongkonstruksjoner, Beregning og dimensjonering etter Eurokode 2, 2.utgave", Akademika, Oslo, Norway, 2013.
20. NS 3473. "Concrete structures – Design and detailing rules". Standard Norge, Lysaker, Norway, 2003.
21. NS-EN 206:2013+NA: 2014 (2014): "Betong, Spesifikasjon, egenskaper, framstilling og samsvar", Standard Norge, Lysaker, Norway, 2014.
22. ACI-ASCE Committee 426, "The Shear Strength of Reinforced Concrete Members". ACI Structural Division, *Proceeding of ASCE*, Vol. 99, No. ST6, June 1973, pp.1091-1187.
23. Van Den Berg F J: "Shear Strength of Reinforced Concrete Beams Without Web Reinforcement, Part 2". *ACI Journal Proceeding*, Vol. 59, No. 11, 1962, pp.1587-1600.
24. Zhang J P: "Diagonal cracking and shear strength of reinforced concrete beams". *Magazine of Concrete Research*, Vol. 49, No. 178, Mar. 1997, pp. 55-65.
25. Zararis P & Papadakis G: "Diagonal Shear Failure and Size Effect in RC Beams without Web Reinforcement." *J. Struct. Eng*., 10.1061/ (ASCE) 0733-9445(2001)127:7(733), pp. 733-742.
26. Jensen T M & Øverli J A: "Experimental study on flexural ductility in over-reinforced lightweight aggregate concrete beams". COIN Project Report No. 47-2013. Norway, 2013.
27. Ahmad S H, Xie Y & Yu T: "Shear Ductility of Reinforced Lightweight Concrete Beams of Normal Strength and High Strength Concrete". *Cement & Concrete Composites*, Vol. 17, 1995, pp. 147- 159.
28. "Properties of lightweight concretes containing". Lytag and Liapor (Document BE96-3942/R8, March 2000).
29. Lo T Y, Tang W C & Cui H Z: "The effects of aggregate properties on lightweight concrete". *Building and Environment*, Vol. 42, 2007, pp. 3025-3029.

Experimental Study on Anchorage in Textile Reinforced Reactive Powder Concrete

Natalie Williams Portal
M.Sc., Ph.D., researcher
RISE Research Institutes of Sweden, Mechanics Research
Box 857 SE-501 15 Borås, Sweden
E-mail: Natalie.williamsportal@ri.se

Mathias Flansbjer
M.Sc., Ph.D., Adj. Prof., researcher
RISE Research Institutes of Sweden, Mechanics Research
Box 857 SE-501 15 Borås, Sweden
E-mail: Mathias.flansbjer@ri.se

Urs Mueller
M.Sc., Ph.D., senior researcher
RISE Research Institutes of Sweden, CBI Swedish Cement and
Concrete Research Institute
Box 857 SE-501 15 Borås, Sweden
E-mail: Urs.mueller@ri.se

ABSTRACT

The EC funded project SESBE (Smart Elements for Sustainable Building Envelopes) focused on utilizing new types of cementitious materials for reducing the mass and thickness of façade elements while increasing their thermal performance. A method enabling the quantification and verification of the required anchorage length for a given textile reinforced reactive powder concrete (TRRPC) is presented. At the material level, tensile tests were conducted to determine the tensile properties of the reinforcement. Pull-out tests were applied to quantify the required anchorage length, while uniaxial tensile tests were performed to quantify the ultimate strength and verify the suitability of the anchorage length at the composite level. The combination of these methods was deemed useful to determine the overlapping length required for large scale façade applications.

Key words: reactive powder concrete, textile reinforcement, anchorage, testing.

1. INTRODUCTION

Within the scope of SESBE (Smart Elements for Sustainable Building Envelopes), funded by the European Commission, smart façade elements were developed with the goal of being lighter,

thinner and more adaptive than existing solutions through the utilization of nanomaterials and nanotechnology [1]. One of the materials developed was a reactive powder concrete (RPC) formulation with higher amounts of supplementary cementitious materials (SCMs) which was combined with carbon textile reinforcement for use in prefabricated concrete façades. Increasing amounts of RPC, often synonymous to ultra-high performance concrete (UHPC), has been used as a façade material as a result of its inherent high strength and durability [2]. The addition of textile reinforcement to such a high performance matrix, designated as textile reinforced reactive powder concrete (TRRPC), enables the drastic reduction of the thickness and weight of precast façade elements, all while improving the post-cracking behaviour of RPC [3].

This paper aims to present the outcome of an experimental study enabling the quantification and verification of the required anchorage length for a given TRRPC prescribed for thin façade elements. The different test methods applied in this study are summarized in Figure 1 along with their corresponding result output. The tensile properties of the textile reinforcement were firstly established by means of tensile tests of individual rovings. The required anchorage length for the composite was quantified using pull-out tests developed specifically for TRRPC. The required anchorage length for the composite was evaluated according to its ability to reach the tensile capacity of the roving. Upon determining a suitable anchorage length from these tests, uniaxial tensile tests were performed to verify the required anchorage length for the composite. The deformations and crack development were captured during tensile testing of the composite by means of an optical full-field deformation measurement system based on Digital Image Correlation (DIC).
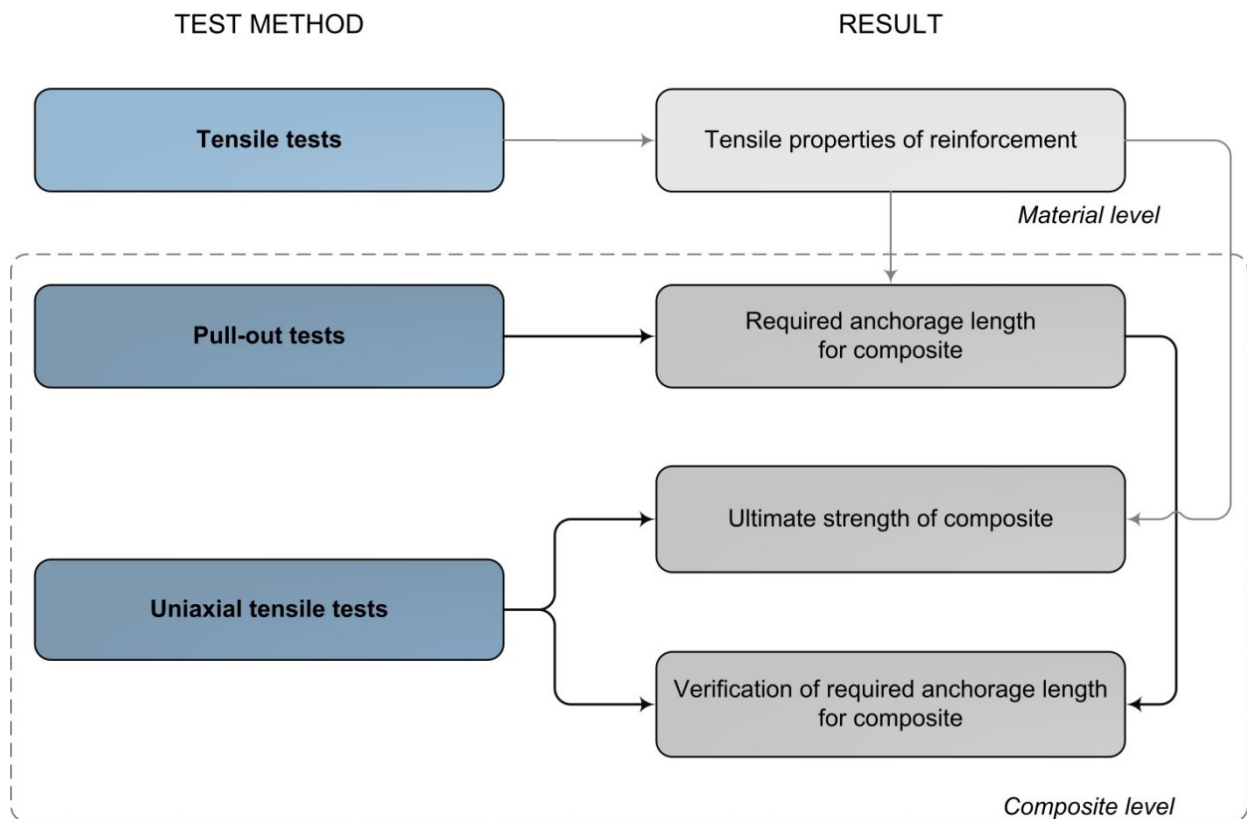
Figure 1 –Flow chart of the experimental study.

## 2.	MATERIALS

### 2.1	Reactive Powder Concrete (RPC)

RPC is a variant of ultra-high performance concrete (UHPC) which has a maximum aggregate size of 2 mm or smaller. It is characterized as having a compressive strength above 120 MPa and a very low amount of capillary pores. The volume proportions of the RPC mix compared to common standard concrete and UHPC mixes are exemplified in Figure 2. The complexity of the RPC mix is such that it consists of six to eight different components; thus, potentially rendering this mix sensitive to proportioning errors. A summary of the mechanical strength properties experimentally quantified for the developed RPC mix applied in this study is provided in Table 1. The compressive strength presented is the average of three test specimens, while the other compressive properties (E-modulus, ultimate strain and Poisson's ratio) were evaluated directly from stress-strain relations pertaining to four test specimens. The tensile strength provided corresponds to the average of eight specimens tested according to direct tensile testing. Additional details concerning the development of the RPC mix can be found in [3].
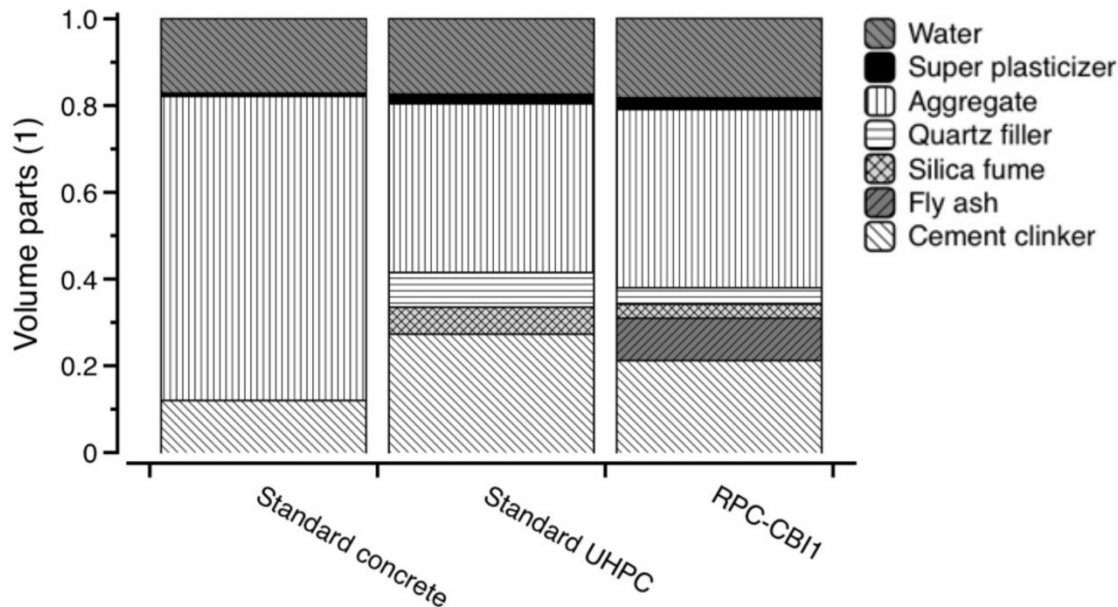
Figure 2 – Volume proportions of the reactive powder concrete mix compared to a standard concrete and UHPC. The illustrated fly ash content of mix RPC-CBI1 includes also the fly ash from the cement.

Table 1 – Summary of average mechanical strength properties (28 days) for RPC-CBI1 (std. dev. in parentheses).

Compressive strength	E-modulus	Ultimate strain	Poisson's ratio	Tensile strength
[MPa]	[GPa]	[‰]	[-]	[MPa]
147.2 (2.3)	49.7 (1.7)	3.89 (0.16)	0.216 (0.021)	5.14 (0.48)

2.2   **Textile reinforcement**

The inherent high strength of RPC however causes it to be extremely brittle upon cracking due to a higher amount of stored elastic energy. To mitigate this brittle behaviour for use in façade elements, textile reinforcement has been incorporated into the matrix to allow for a ductile post-cracking behaviour marked by closely spaced fine cracks. The textile reinforcement applied is an epoxy impregnated carbon textile reinforcement grid (Solidian GRID Q85/85-CCE-21), as illustrated in Figure 3. Within this project, epoxy coating was found to significantly increase the bond between the carbon textile and the given matrix.
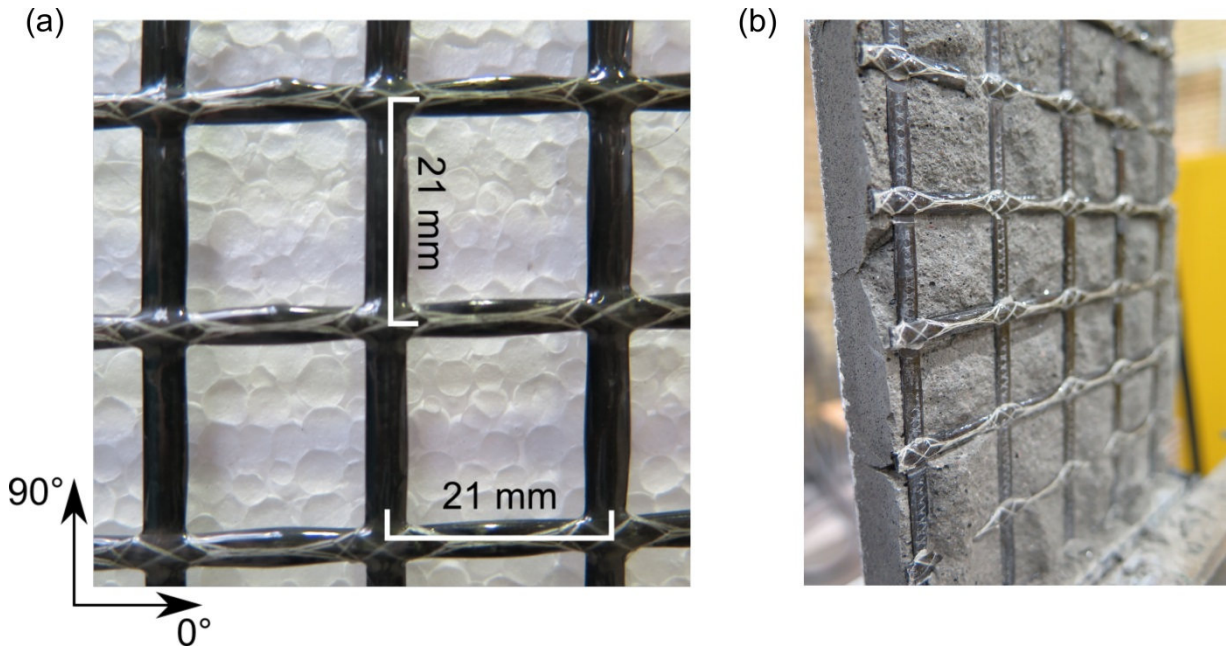
Figure 3 – Orientation of the carbon textile reinforcement (Solidian GRID Q85/85-CCE-21) (a) and textile reinforcement embedded in concrete matrix (b).

Tensile tests were applied to quantify the tensile properties of the textile reinforcement, so-to-say tensile strength, modulus of elasticity and ultimate strain. It is important to quantify the fundamental mechanical properties of the textile reinforcement to be able to further characterize the composite behaviour at different levels. The tests were performed according to ISO 10406-1 [4]. The tensile properties were determined for rovings in the longitudinal direction (90°) and the transversal direction (0°) of the carbon grid panel, as per Figure 3. A total of seven specimens, configured according to Figure 4 (a), were tested for each orientation to obtain a representative average behaviour.
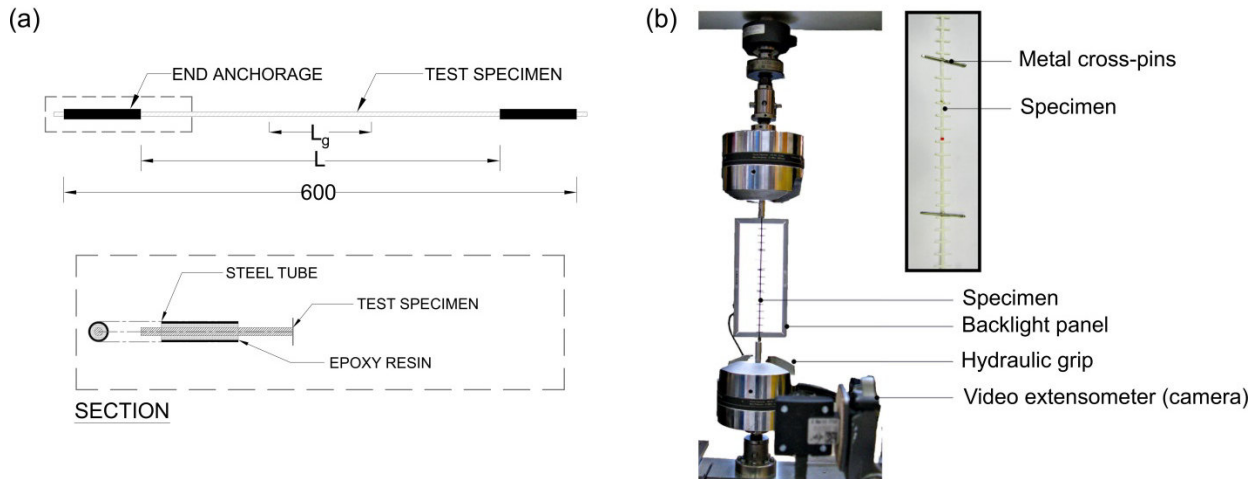
Figure 4 – Tensile test specimen configuration (a) and overview of tensile test setup (b).

The tensile tests were carried out in an electro-mechanical testing machine (Sintech 20/D) and the deformation was measured by a video extensometer (Messphysik ME46) with backlight technique as illustrated in Figure 4 (b). The load was introduced to the free end of the roving by gripping the end anchorage (100 mm steel tube filled with epoxy) in the conventional hydraulic grip of the testing machine. The free length of the specimen, *L*, was 400 mm and the measurement length, L_g, was 100 mm. The tests were controlled by the cross-head displacement of 3 mm/min.

The tensile strength, f_u, and Young's modulus, *E*, were evaluated from the test results, assuming the nominal roving area to be equal to that specified by the producer of $A_{roving} = 1.81$ mm^2. Furthermore, Young's modulus was calculated from the stress-strain relation as the secant modulus between the load level at 20 % and 50 % of the tensile capacity. A summary of the average mechanical tensile properties is given in Table 2.

Table 2 – Summary of average tensile properties of the carbon textile grid (std. dev. in parentheses).

Textile roving direction	Roving area	Tensile strength	Ultimate strain	Young's modulus
[°]	A_{roving} [mm^2]	f_u [MPa]	ε_u [%]	*E* [GPa]
90	1.81	3433 (212)	1.44 (0.10)	233 (15)
0	1.81	3878 (212)	1.52 (0.06)	248 (5)

## 3.	PULL-OUT TESTS

### 3.1	General

Pull-out tests are commonly applied to determine the bond behaviour between reinforcement and a concrete matrix, as well as to quantify required anchorage length (overlapping length) which are relevant for upscaling of textile reinforced concrete. Characterizing the bond behaviour is critical to be able to understand the complex composite behaviour of this composite material. In principle, force transfer between the textile reinforcement and concrete is effectuated by adhesion and friction. In addition, there will be force transfer due to mechanical locking at the intersection between longitudinal and transversal rovings. The load transfer

between the filaments enclosed in the roving will occur either based on adhesion or friction depending on the quality of the bond or so-called *fill-in zone* of concrete within the reinforcement roving. The *fill-in zone* can be defined as the depth at which adhesive load transfer can take place between the filaments and the matrix. The inner zone, i.e. core, is defined as the filaments having less contact with the matrix but assuming that frictional load transfer between the filaments remains possible [5]. In this particular case, there is an epoxy coating surrounding the carbon roving which appears to solely cover the outer edge of the roving which does not particularly allow for concrete penetration into the roving. Furthermore it is presumed that this coating slightly increases the cross-section of the roving but not necessarily the contact of fibres within the roving.

To simplify the understanding and analysis of the pull-out test results, three main stages of stress transfer occurring between the concrete matrix and textile reinforcement are characterized after Mobasher [6] and Richter, Lepenies, et al. [7], see Figure 5. Stage I (Elastic) corresponds to the linear response thus signifying perfect bond between reinforcement and matrix (i.e. adhesive bond). Stage II (Non-linear) takes into consideration the pre-peak zone which consists of the initial partial debonding (external filaments) and spreading of debonding along the embedded length. This stage also includes the post-peak zone which is marked by the successive debonding until the entire embedded length is debonded. Stage III (Dynamic) refers to the individual filaments sliding out dynamically (i.e. due to frictional bond).
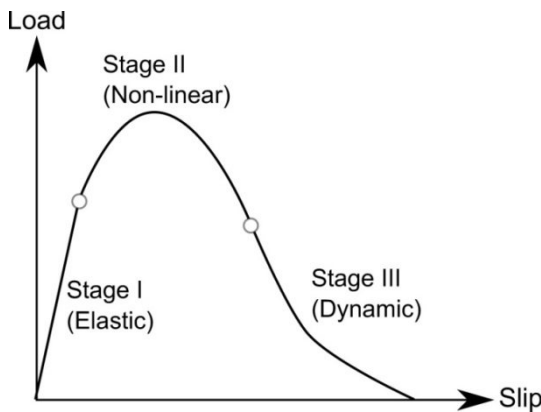
Figure 5 – Idealized pull-out load-slip response of embedded textile reinforcement in concrete (Adopted from [6]).

3.2 Test description

Single sided pull-out tests were performed on rectangular specimens reinforced by one layer of textile reinforcement according to that illustrated in Figure 6. The embedment length, L_e, was demarcated by cutting away the centrally located roving submitted to pull-out at the edge the anchorage length, L_a. Accordingly, the total length of the specimen was dependent on the prescribed embedment length. The anchorage length and the free end length, L_r, remained constant in all specimens. In this study, the variation of the embedment length was selected based on the centre-to-centre grid spacing of 21 mm. Three specimens were tested for each embedment length variation studied: 1) "2G", L_e = 42 mm, 2) "3G", L_e = 63 mm and 3) "4G", L_e = 84 mm. The test specimens were cast in plywood formwork which allowed for the centric positioning of the carbon textile grid within the cross-section. The specimens were covered by plastic and demoulded after 24 hours. The specimens were cured in a climate room (20°C, 60 %

RH) for approximately 21 days and then placed in an indoor laboratory environment to conduct further test preparations.
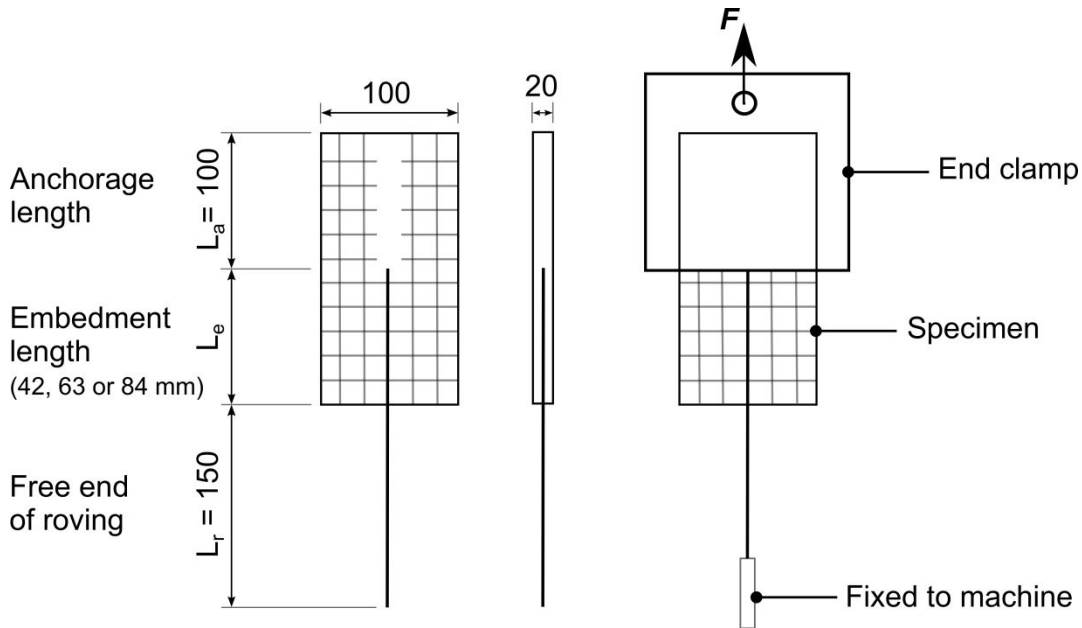

Figure 6 – Single sided pull-out test specimen geometry and configuration (dimensions in mm).

The pull-out tests were carried out using an electro-mechanical universal testing machine (Sintech 20/D) shown in Figure 7 (a). The load was introduced to the free end of the roving by gripping the end anchorage (100 mm aluminium tube filled with epoxy) in the conventional hydraulic grip of the testing machine. The anchorage length of the specimen was clamped between two stiff steel plates of clamping devices attached to the testing machine. The tests were controlled by the cross-head displacement of 1 mm/min with a data sampling rate of 10 Hz. A video extensometer (VE) technique (Messphysik Video Extensometer ME46 with pattern recognition) was used to measure the active end-slip of the reinforcement relative to the concrete end, as exemplified in Figure 7 (b).
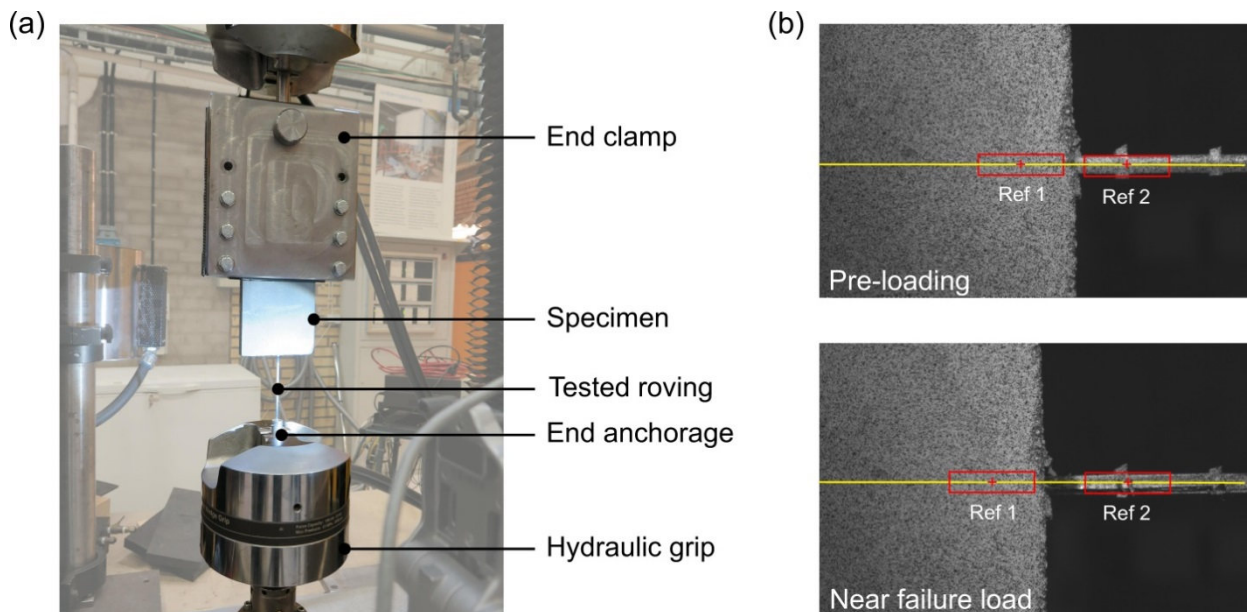
Figure 7 – Pull-out test setup (a) and images of active end-slip measured by a video extensometer technique with indicated references points (Ref 1 and Ref 2)(b).

3.3   Results

To analyse the pull-out test results, the maximum load is plotted against the embedment length in Figure 8. It can be observed that a distinct increase in the maximum load was observed as the embedment length increased. As well, the failure mechanism also transitioned from pull-out to textile rupture. Textile rupture generally occurred when the maximum load exceeded that of the tensile capacity of the carbon roving to be approximately 6.21 kN (std dev, $\sigma = 0.38$) in the orientation of 90°. The maximum load for two grid spacings (2G) was 3.87 kN (std dev, $\sigma = 0.37$), 5.13 kN (std dev, $\sigma = 0.37$) for three grid spacings (3G) and 6.05 kN (std dev, $\sigma = 0.81$) for four grid spacings (4G). It is thought that the deviation in results and failure mode noted for the 4G specimens could have been caused by material variability or underlying load eccentricity. Overall, the embedment length corresponding to the 4G specimens was found to be a suitable anchorage length since textile rupture was generally achieved.
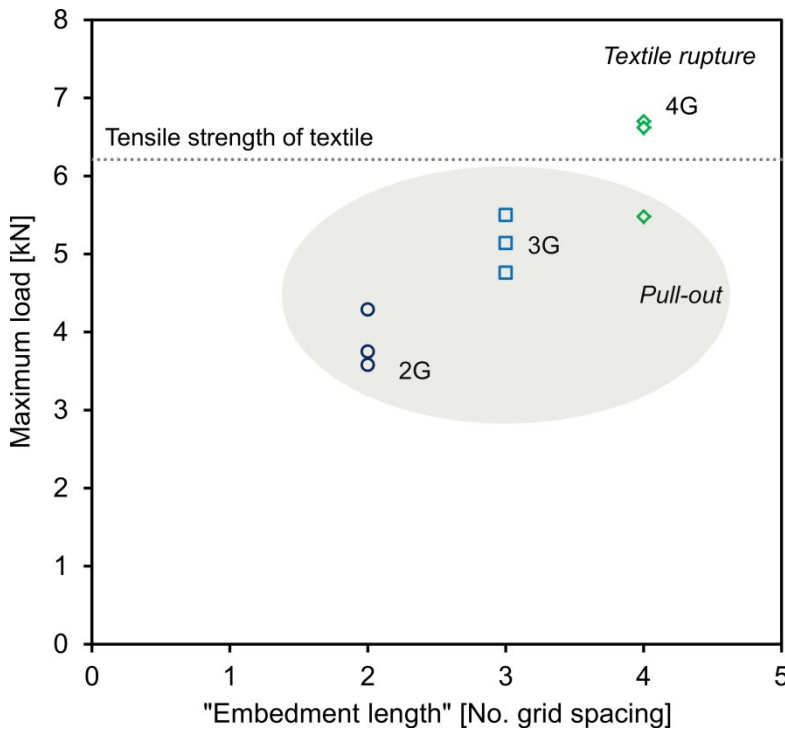
Figure 8 –Failure mechanisms observed with respect to maximum load and embedment length.

Moreover, the results from the VE measurements were analysed to capture the stress in the pulled roving as well as its active end-slip. The VE measurements for each specimen variation are depicted in Figure 9. The reinforcement stress was calculated by dividing the force by the cross-sectional area of one roving. The active end slip of the roving being pulled-out of the specimen was measured between two predefined reference points along the exposed roving (measurement length = 15 mm). It can be seen that the elastic part of the curve, denoted by Stage I, has a relatively similar slope for all cases. At the end of Stage II, the so-called post-peak region, the slope of the curve increases as the overlap increased from two to four grid spacings. This phenomenon could be explained by the fact that the successive debonding of the roving occurred at a faster rate due to a presence of higher bond stresses, which in turn also resulted in less roving pull-out and/or rupture in Stage III.
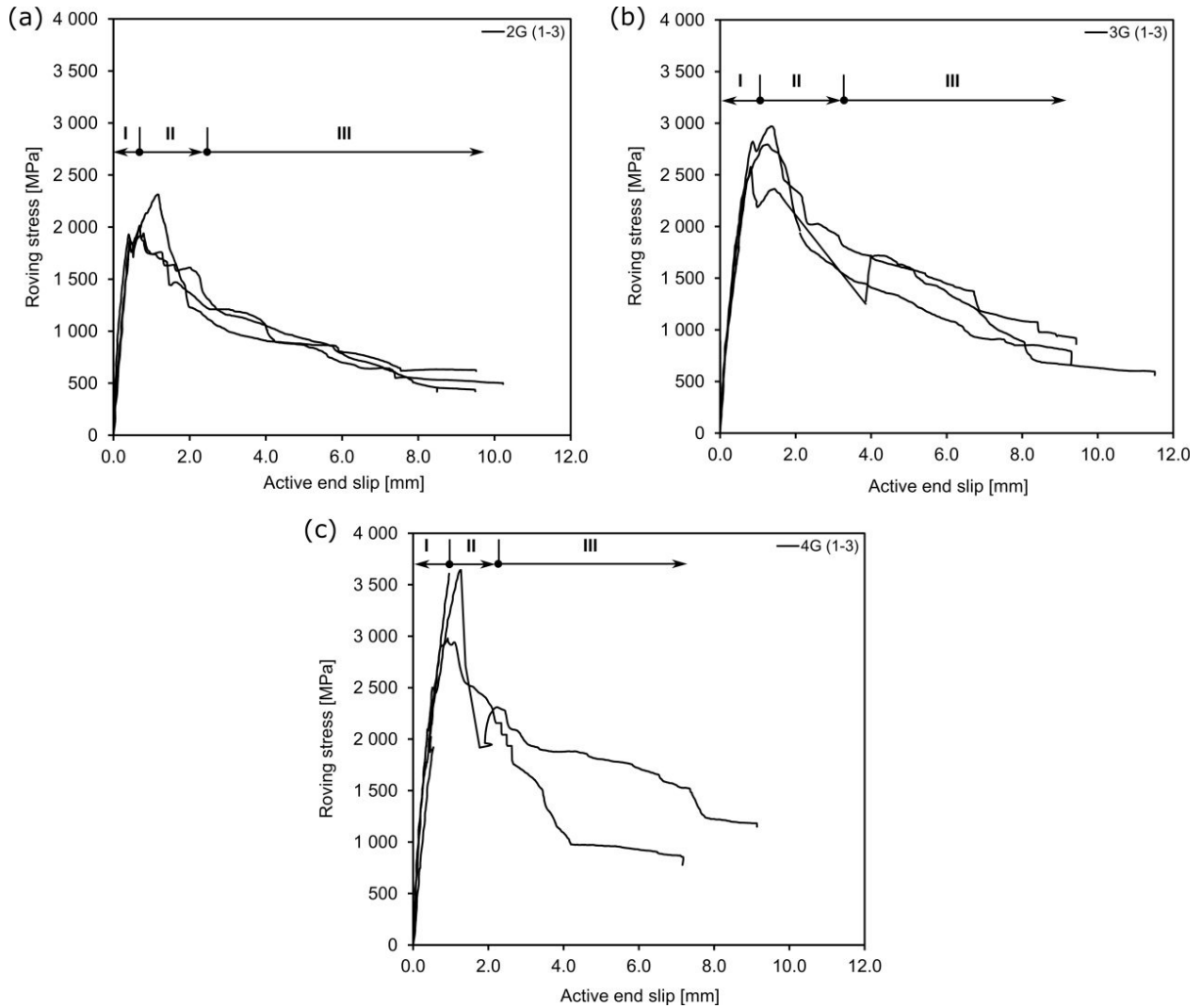
Figure 9 – Roving stress versus active end-slip based on VE measurements with indicated stages for 2 grid spacings (a), 3 grid spacings (b) and 4 grid spacings (c).

4.   UNIAXIAL TENSILE TESTS

4.1   General

To illustrate the possible enhancements of the tensile behaviour of RPC by incorporating textile reinforcement, a parallel is drawn between the tensile behaviours of concrete/mortar and textile reinforced concrete in Figure 10. The brittle behaviour of the concrete/mortar succeeding first cracking (Stage I) is eliminated in the case of TRC due to the fact that the tensile stresses are transferred to the textile reinforcement. The initial stress transfer from the matrix to the textile causes a series of load jumps marked by a minimal increase in stress level (Stage IIa). The stabilization of cracking eventually takes place in Stage IIb, whereby a so-called strain hardening phenomenon causes a notable stress and strain increase until reaching a form of failure mechanism, i.e. rupture of roving, pull-out or a combination (Stage III).
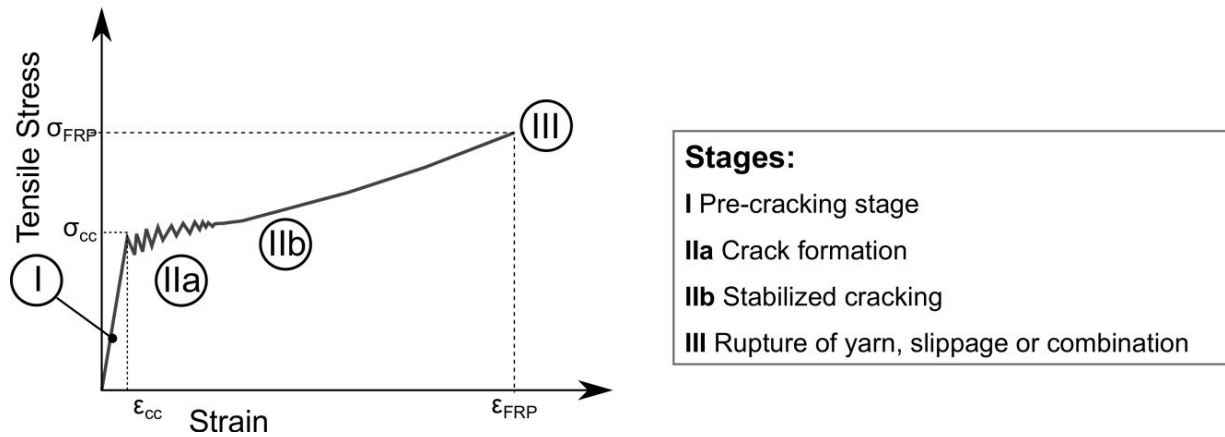
Figure 10 – Expected tensile behaviour of textile reinforced concrete.

4.2 Test description

The tensile behaviour of thin textile reinforced RPC panels was characterized using uniaxial tensile tests in accordance with the recommendation of RILEM TC 232-TDT [8] along with Digital Image Correlation (DIC) measurements. Rectangular panel specimens (700 x 100 x 25 mm) reinforced by two layers of textile reinforcement were tested with and without a centrically placed overlap splice in the reinforcement grids as per Figure 11. The overlap was prescribed according to the most suitable anchorage length determined by the pull-out tests (4G). Three specimens were tested for each variation, denoted RPC-(1-3) for reference samples and RPCO-(1-3) for overlap samples. The panels were cast in plywood formwork, covered by plastic and demoulded after 24 hours. Thereafter, the specimens were cured in a climate room (20°C, 60 % RH) until a few days prior to testing in order to allow for surface preparation.
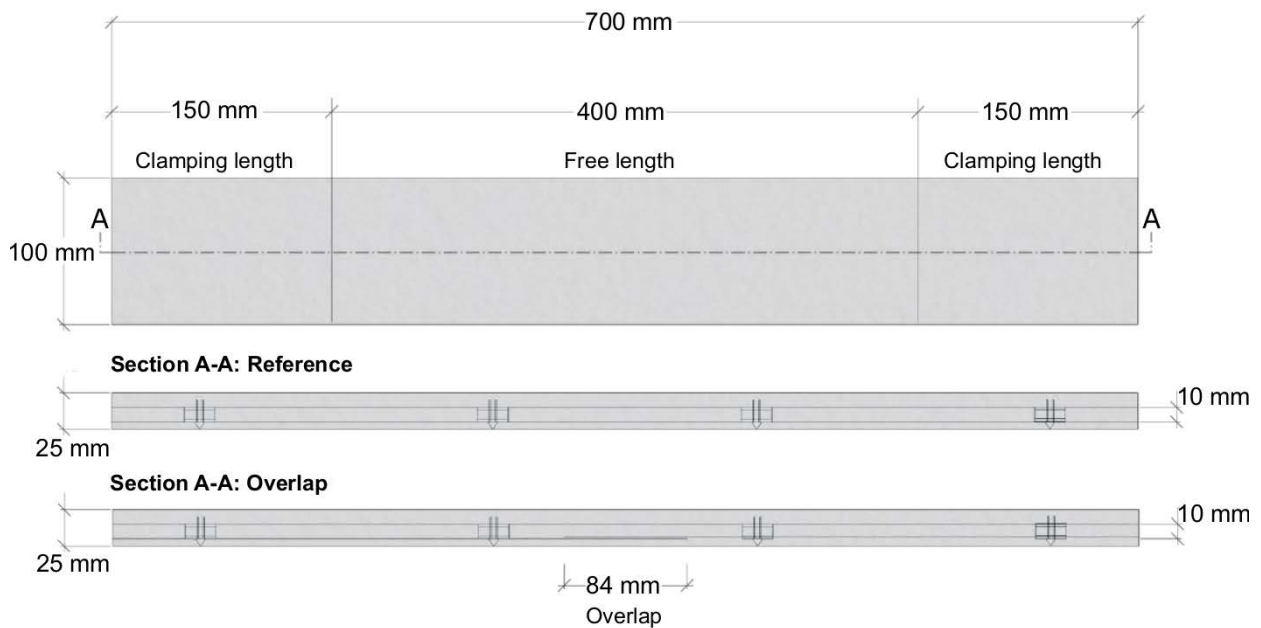
Figure 11 –Specimen configuration with reinforcement placement and prescribed overlap in cross-section.

The ends of the specimen were clamped between two stiff steel plates, shown in Figure 12 (a), within the clamping length before testing in an alignment frame to ensure centric loading. Thin neoprene rubber sheets were used in the contact areas to avoid local stress concentrations. All overlapping concrete edges and local unevenness in the contact area were removed with a grinder before clamping. The clamping length was set to 150 mm and the clamp bolts were tightened with a torque of 20 Nm. The free length between the two clamping devices was set to approximately 400 mm. The clamping devices were thereafter hinged connected to the testing machine, as per Figure 12 (b). These tests were carried out using the same testing machine as applied for the pull-out tests, and were controlled by the cross-head displacement of 0.5 mm/min until reaching approximately 25 % of the maximum load which generally took place at the fringe of the crack stabilization phase. The loading scheme was then adjusted to 1.0 mm/min until approximately 40 % of the maximum load and thereafter to 2.0 mm/min for the remaining of the test. The load and cross-head displacement were recorded in a data acquisition system with a sampling rate of 25 Hz.
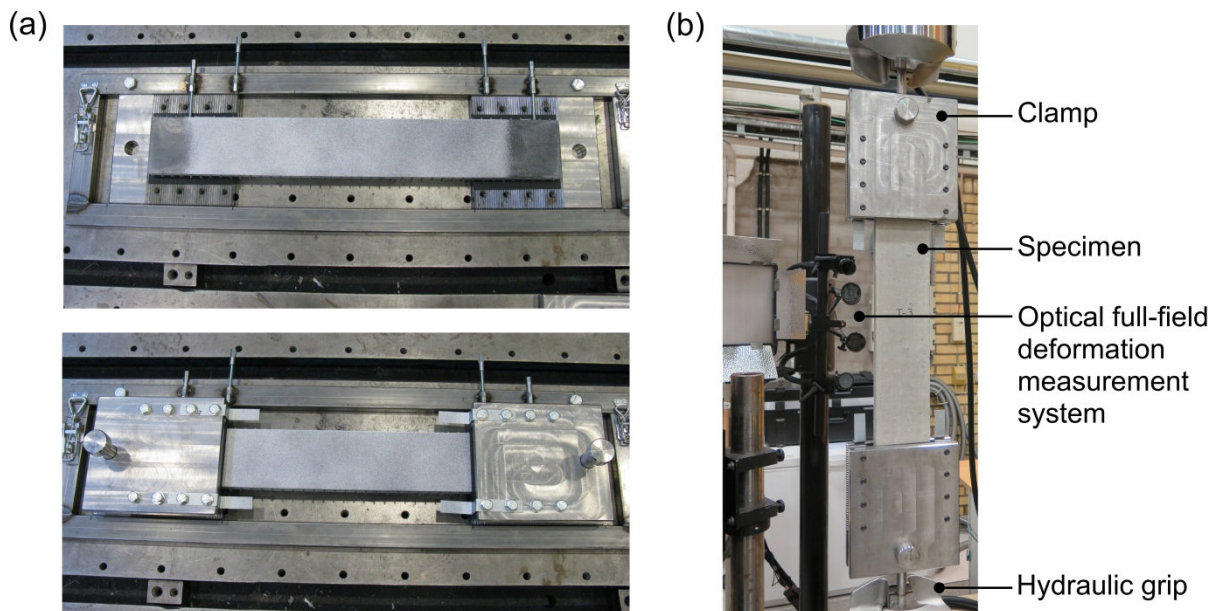
Figure 12 – Alignment frame for the panels (a) and uniaxial tensile test setup (b).

The deformations and crack development were recorded on one side of the specimen during testing by the use of the optical full-field deformation measurement system ARAMIS$_{TM}$ 12M by GOM [9]. The system uses a measurement technique based on DIC with a stereoscopic camera setup, consisting of two CCD-cameras with 12 Mega pixel resolutions. In this study, the system was calibrated for a measurement volume of approximately 400 x 300 x 300 mm^3. The speckle pattern was achieved by first applying white retro-reflective paint as a background on the sample followed by applying lightly speckled black stains using a spray-paint. To obtain high contrast levels, the specimen was also illuminated by a white LED light panel during testing. An image captured frequency of 1 Hz was used while the load and displacement from the testing machine were simultaneously recorded in the ARAMIS system. A facet size of 30 x 30 pixels and a ten-pixel overlap along the circumference of each facet were chosen. For the system setup employed, this corresponds to a spatial resolution of approximately 3 x 3 mm. The coordinate measurement accuracy was better than 1 μm.

4.3 Experimental results

Load versus global displacement relationships obtained from the uniaxial tensile tests are presented in Figure 13 for RPC and RPCO specimens, respectively. In this case, the global displacement represents the displacement of the cross-head. The tensile results are summarized in terms of first cracking and maximum load properties for all tested specimens in Table 3, while the roving stress was based on the singular roving area multiplied by the number of rovings in the cross-section.

Table 3 – Summary of uniaxial tensile test results

Specimen ID	1st crack		Max. load	Roving stress at max. load
	$P_{cr,1}$ [kN]	$\sigma_{cr,1}$ [MPa]	P_{max} [kN]	$\sigma_{roving,max}$ [MPa]
RPC-1	5.6	2.4	64.4	3560
RPC-2	6.0	2.5	58.0	3202
RPC-3	8.3	3.7	63.4	3503
Avg. (std. dev.)	6.6 (1.5)	2.9 (0.7)	61.9 (3.5)	3422 (193)
RPCO-1	6.2	2.9	51.0	2815
RPCO-2	4.5	2.0	46.3	2555
RPCO-3	4.9	2.3	53.4	2949
Avg. (std. dev.)	5.2 (0.4)	2.4 (0.4)	50.2 (3.6)	2773 (200)
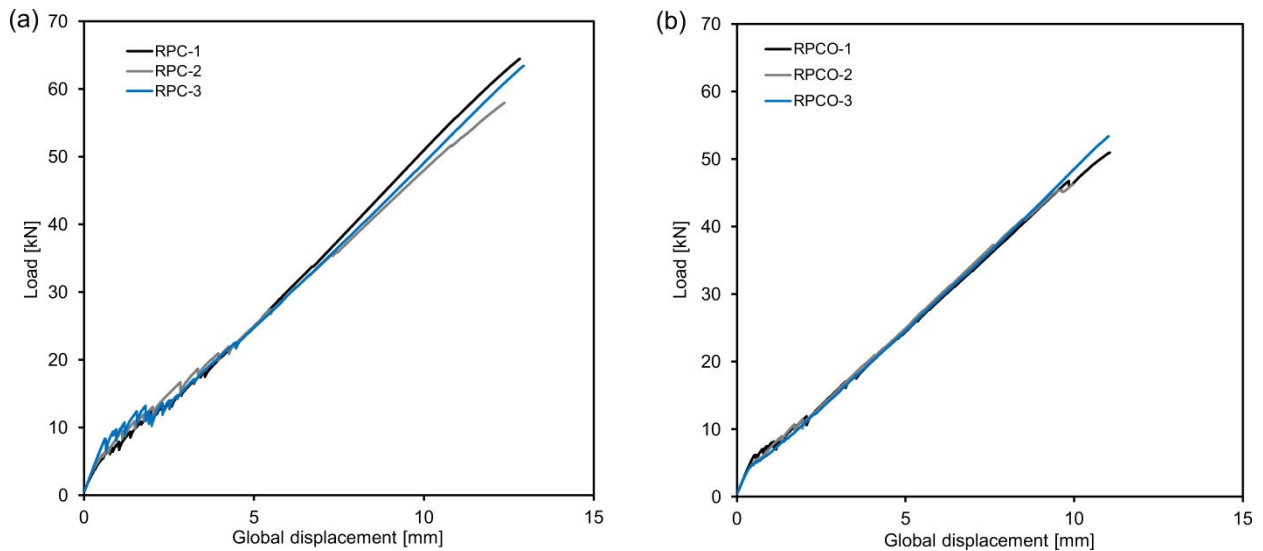
Figure 13 – Tensile load versus global displacement for reference RPC panels without overlap (a) and RPCO panels with overlap (b).

The uncracked specimen has a relatively stiff and linear behaviour up until first cracking which is assumed to have taken place upon reaching the tensile strength of the concrete at an average load of 6.6 kN amounting to a tensile strength of 2.9 MPa. After first cracking, multiple-cracking marked by a series of load jumps with minimal load increase took place. The crack initiation generally occurred at the location of a lateral roving which introduced a stress concentration in the cross-section. It can also be noted that the size of the load jumps during the initial multiple-cracking phase are smaller for RPCO specimens, which could partly signify that there was a superior bond between the matrix and the textile or could be a result of the

additional overlap reinforcement. The crack formation eventually stabilized and was marked by a noticeable gain of stiffness said to be governed by the properties of the textile reinforcement; which is often described as a form of strain hardening.

The maximum load, P_{max}, was approximately 19 % lower for the RPCO specimens because the stress in the reinforcement never reached the tensile strength of the carbon textile grid. Instead, failure was generally marked by concrete spalling in the central zone of the specimen at the location of the overlap. The RPCO specimens were found to be more susceptible to spalling particularly in the overlap region due to the fact that the localized cover thickness was minimized as a result of the inclusion of a slightly greater amount of reinforcement in the overlap. Nevertheless, the overall tensile behaviour of the RPCO specimens is highly comparable to that of the reference RPC specimens in terms of stiffness, bond strength and the extent of crack formation.

4.4 Optical deformation measurements

The load versus global displacement relationship along with DIC measurements obtained from the uniaxial tensile tests is typified in Figure 14 for two specimens, RPC-1 (reference) and RPCO-1 (overlap). From this figure, it is possible to follow the formation of individual cracks represented as major strain overlays from the DIC measurements. Both specimens achieved comparable ultimate strength values and multiple cracking across the free zone of the specimens. Since cracks propagated within the overlap region for RPCO-1, this is an indication that the prescribed overlap of 4G (L_e = 84 mm) is suitable when introduced in the composite.
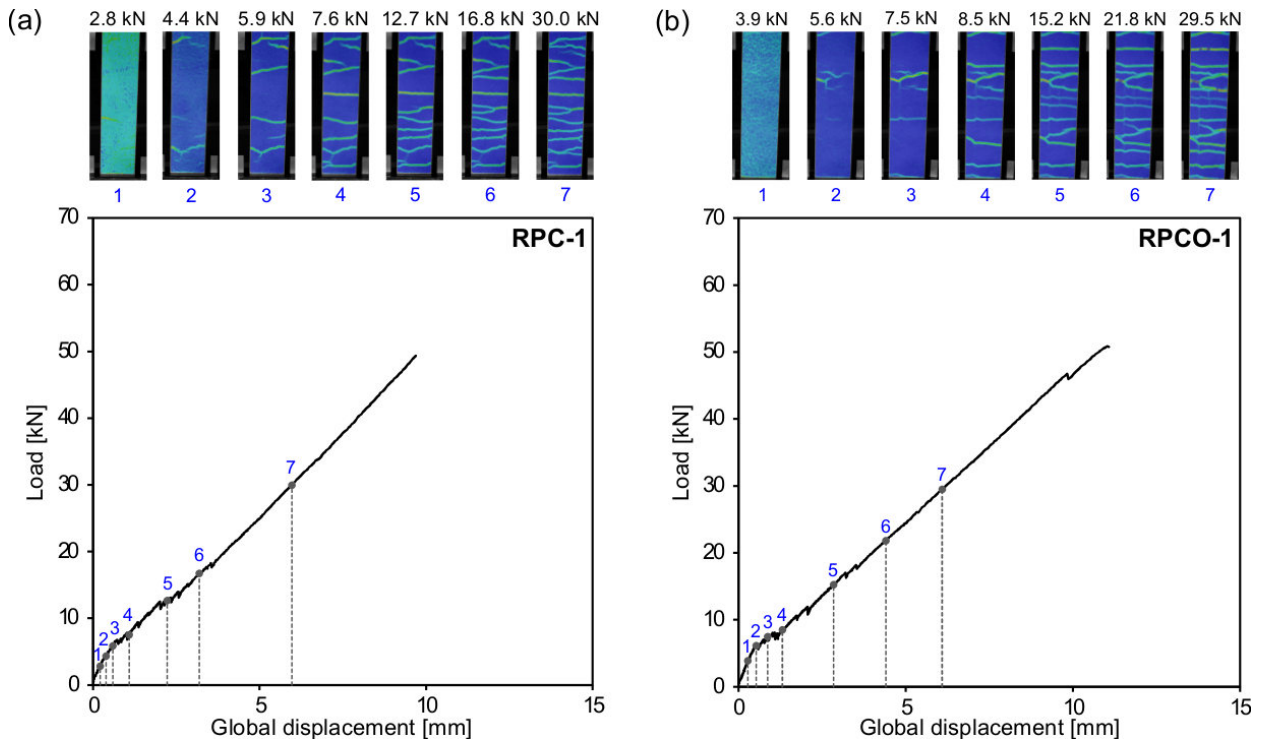
Figure 14 – Tensile load versus global displacement for RPC-1 reference panel (a) and RPCO-1 overlap panel (b). The crack propagation is presented above the graphs by means of major strain overlays from the DIC measurements.

Strain fields can clearly highlight even small discontinuities at the surface of the specimen and it can be noted that multiple fine cracks propagated across the sample's free zone during loading. The free zone is measured from the bottom of the specimen above the clamp (position of 0 mm) to the top of the specimen below the clamp (position of 400 mm), as illustrated in Figure 11. However, in reality the strains across a strong discontinuity related to a crack are infinite, which means that a crack cannot be properly described in terms of strain. Instead, the crack opening and crack path can be quantified by analysing the displacement discontinuities associated with a crack. Contour plots of the longitudinal displacement after formation of all main cracks at a load level of 20 kN are shown in Figure 15. Furthermore, details pertaining to the displacement profile along the specimens (highlighted sections lines) are shown in the accompanying displacement versus position diagrams. The crack opening displacement can be defined as the displacement difference between the two crack faces, which approximately corresponds to the displacement jumps in the section line profiles. The position of the crack is defined by the mid-point between the crack faces. From the displacement profiles shown in Figure 15, it can be noted that the crack development was similar for all specimens. The main cracks appeared at an average spacing between 25 and 35 mm and that the crack opening displacement at 20 kN was in the range of 0.05 mm to 0.2 mm. According to this observed crack pattern, it can be stated that there is good bond strength between the textile and the matrix such that the stress transfer length is minimal and somewhat related to the textile grid spacing.
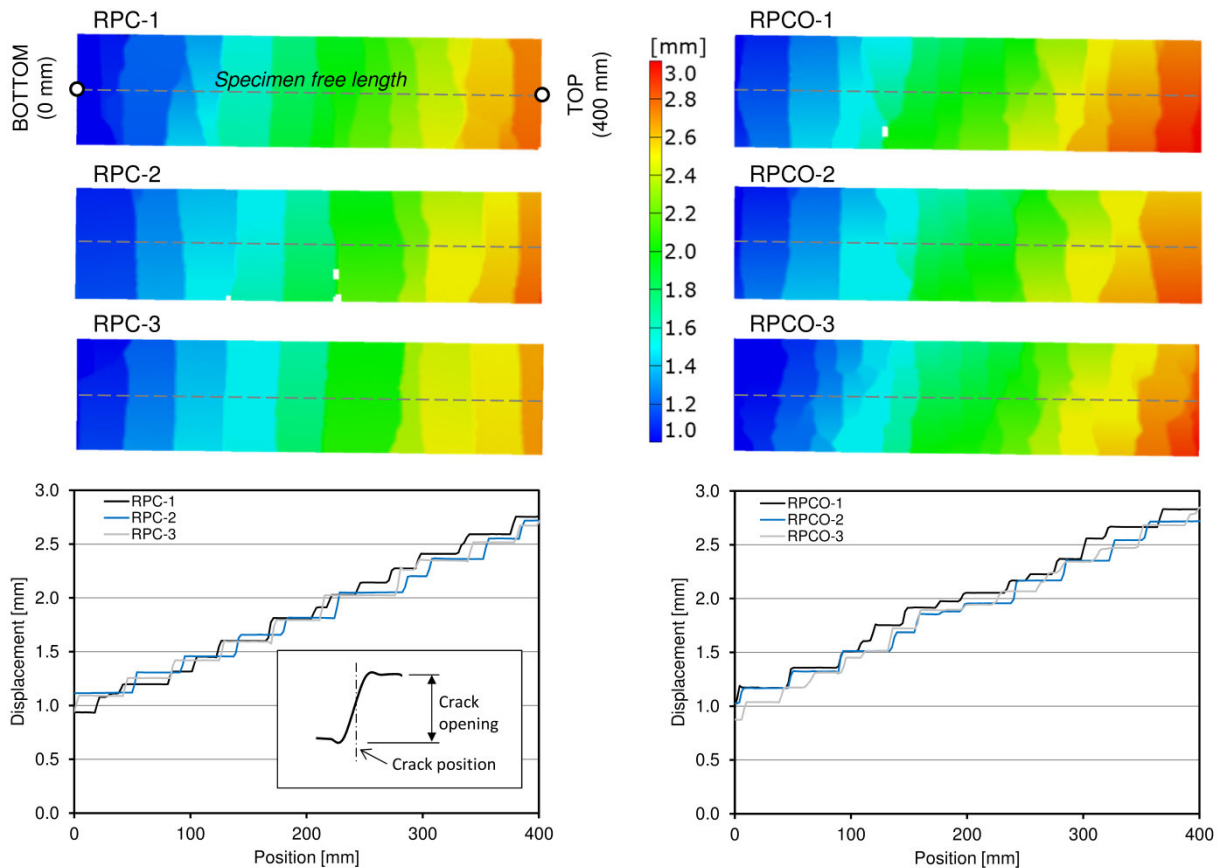
Figure 15 – Contour plots of the longitudinal displacement and displacement profile along the free length of the specimens at a load level of 20 kN.

5.　　　CONCLUDING REMARKS

Linking test methods on the material and composite levels has been shown to adequately quantify and verify the anchorage length required for the developed TRRPC material. An anchorage length amounting to four grid spaces (84 mm) was found to be suitable for the given composite to achieve adequate load transfer across a reinforcement overlap splice. Optical deformation measurements via DIC proved to be an advantageous method to follow the individual crack formation and quantify comprehensive displacement measurements during specimen loading. Ultimately, the overlapping length quantified in this work appears to be suitable for further implementation on a larger scale such as in precast concrete façade elements.

ACKNOWLEDGEMENTS

REFERENCES

1.　　SESBE Smart Elements for Sustainable Building Envelopes: http://www.sesbe.eu/, 2017.
2.　　Mueller U, Meng B, Kühne H-C, Nemecek J, Fontana P: "Micro texture and mechanical properties of heat treated and autoclaved Ultra High Performance Concrete (UHPC)," *Proceedings*, 2nd International Symposium on Ultra High Performance Concrete, Kassel, Germany, Kassel University Press, 2008, pp. 213-220.
3.　　Mueller U, Williams Portal N, Chozas V, Flansbjer M, Larazza I, da Silva N, Malaga K: "Reactive powder concrete for façade elements – A sustainable approach," *Journal of Façade Design and Engineering*, Vol. 4, 2016, pp. 53-66.
4.　　ISO 10406-1: "Fibre-reinforced polymer (FRP) reinforcement of concrete – Test methods. Part 1: FRP bars and grids". International Organization for Standardization, 2008.
5.　　Hartig J, Häußler-Combe U, Schicktanz K: "Influence of bond properties on the tensile behaviour of Textile Reinforced Concrete," *Cement and Concrete Composites*, Vol. 30, No.10, 2008, pp. 898-906.
6.　　Mobasher B: "Mechanics of fiber and textile reinforced cement composites," *CRC press,* 2012.
7.　　Richter M, Lepenies I, Zastrau B W: "On the influence of the bond behaviour between fiber and matrix on the material properties of textile reinforced concrete," *International symposium of anisotropic behaviour of damaged materials*, 2002, pp. 1-24.
8.　　RILEM TC 232-TDT (Brameshuber W): "Recommendation of RILEM TC 232-TDT: test methods and design of textile reinforced concrete – Uniaxial tensile test: test method to determine the load bearing behavior of tensile specimens made of textile reinforced concrete," Vol. 49, No.12, 2016, pp. 4923-4927.
9.　　GOM: "GOM Correlate Manual Basic, GOM optical measuring techniques," Braunschweig, Germany, 2015.

Fire Spalling of High-Performance Basalt Fibre Concrete

Ali Mohammadi Mohaghegh
Licentiate, PhD Candidate
Department of Ocean Operations and Civil Engineering
NTNU-Ålesund
P. O. Box 1517, N-6025 Ålesund
Corresponding author: ali.m.mohaghegh@outlook.com

Johan Silfwerbrand
Professor
Department of Civil and Architectural Engineering
KTH Royal Institute of Technology,
SE-100 44 Stockholm

Vemund Årskog
Associate Professor
Department of Ocean Operations and Civil Engineering
NTNU-Ålesund
P. O. Box 1517, N-6025 Ålesund

Robert Jansson McNamee
PhD
Research and Development Manager at
Brandskyddslaget AB
Långholmsgatan 27,
SE -117 33 Stockholm

ABSTRACT

The use of Macro Basalt Fibre Concrete (MBFC) for structural purposes is increasing in the Norwegian market. However, findings on properties related to fire spalling are scarce in the literature. Motivated by this, the authors present the results of a pilot experimental study on fire spalling properties of two types of basalt fibre concrete. The study results show that basalt fibres cannot prevent high-performance concrete (HPC) from fire spalling. Nonetheless, the comparison of the average spalling values indicates that use of basalt fibres probably does not increase the spalling propensity of the tested materials.

Keywords: Macro basalt fibres, chopped basalt fibres, high-performance concrete (HPC), fire spalling.

1. INTRODUCTION

Basalt fibre concrete has been considered as an interesting alternative for marine concrete structures. The reason is its unique combination of good mechanical and durability properties [1-4]. Mechanically, macro basalt fibre concrete works as steel fibre concrete by providing load-carrying capacity after cracking, ductility and crack control. One shortcoming regarding steel fibres are that they corrode in harsh marine environments. Basalt fibres have, however, proved to be resistant to degradation in marine environments [1, 4].

When micro-cracks appear on the concrete surface due to fire exposure, followed by explosive flaking of materials from the concrete surface, the concrete loses its strength and integrity [5-7]. This phenomenon that occurs due to continuous heating is called fire spalling [6, 7]. Dependent on the intensity of the fire and the exposure time, the spalling can reduce the cross section of a concrete element and may lead to a structural collapse [8, 9].

Dense concrete may spall in moist conditions if subjected to fire [10-13]. Furthermore, external forces can also increase the fire spalling tendency of concrete [5, 9, 14]. Fibres have shown to be effective in reducing or even preventing spalling, but the effect is dependent on the fibre material [15]. Whereas steel fibres have demonstrated only a minor influence on spalling, polypropylene fibres have shown a significant effect [16-18]. The difference is due to the fibre behaviour at different fire temperatures. There are different arguments pertaining to the effect of steel fibres on fire spalling of high-performance concrete [17]. However, in the majority of studies, the addition of steel fibres shows only a minor beneficial effect on fire spalling of concrete [19, 20]. Polypropylene fibres melt in the interval from 160°C to 170°C, which has very beneficial effects on the spalling behaviour when the temperature continues to rise [17, 21]. In the literature, it seems that the mechanism of fire spalling is not entirely understood [22, 23]. Several theories are discussed by the research community, but the simplest explanation is that the melting polypropylene fibres are absorbed by the cement matrix provide channels in which the overpressure of the heated vapour can escape [24-26]. The overpressure is regarded as the main course of spalling [14].

Swedish Concrete Association developed a design guideline to prevent civil engineering concrete structures from fire spalling. This guideline has been developed based on the studies performed during 2004-2008 [12]. The guideline recommends the use of polypropylene fibres as an economical solution to prevent the concrete structures from fire spalling. The amount of recommended polypropylene fibres depends on the risk of fire, the economic and social effect of the fire, water-binder ratio, and the powder content of concrete mixes [12]. Thereby, the recommended content of polypropylene fibres varies between 1 and 1.4 kg/m^3 [12]. Other European countries also developed their national guidelines to ensure the structural performance of concrete in fire [27]. For the structural protection of road tunnel lining during a fire, German guideline recommends using a volume content of 2 kg/m^3, 16-20 μm polypropylene fibres [27].

There are only limited studies that have been performed on the behaviour of basalt fibre composites exposed to fire. Bhat et al. [28] performed a comparative investigation on the effect of direct fire exposure on basalt and E-glass fibre vinyl ester composites. They found that the degradation starts with softening of vinyl ester at its glass transition temperature of 120°C. Then the process continues with the decomposition of the matrix at a temperature of 350°C-450°C. Finally, fibre softening leads to tensile failure of composites.

The macro basalt fibre is a two-component product where the basalt material is encapsulated by a vinyl ester resin [29]. Based on the study performed by Bhat et al. [28], the basalt vinyl ester

composites show degradation through a softening and decomposition process when it is exposed to direct fire. However, the behaviour of basalt fibre composite in a concrete matrix when it is indirectly subject to fire is not known. The softening and decomposition of the composite may enable the fibres to improve the fire resistance of concrete analogous behaviour to that the melting of polypropylene fibres does. Another beneficial effect might be that the fibres keep cracked parts stay in place acting as a thermal shield.

As indicated above, the current application of basalt fibre concrete is marine structures. They are subjected to a very harsh environment. In order to resist the harsh environment, the concrete should be dense which in turn implies a low water-binder ratio. In this pilot study, fire tests were carried out on basalt fibre concrete designed for marine environments. Previous fire tests have shown that the spalling increases with decreasing water-binder ratios and that the demands on measures to prevent spalling will be more challenging [6, 9]. Consequently, any beneficial effect of basalt fibres may be more difficult to identify in low water-binder ratio concrete than in normal grade concrete mixes. This is, however, outside the scope of this paper.

2. RESEARCH SIGNIFICANCE, AIMS AND SCOPE

The benefit of using polypropylene fibres to reduce fire spalling is a well-established approach [5, 30]. The research and development of new construction materials is an ongoing process. The use of recently developed macro basalt fibres for structural applications is growing. However, based on our knowledge, the behaviour of basalt fibre concrete during fire exposure has not been subject to intensive study. Motivated by this insight, the aim of this work is to investigate the fire spalling behaviour of high-performance basalt fibre concrete. The study, presented in this paper, includes an experimental approach to assess the fire-spalling behaviour. Considering the limited budget of our study, it can be labelled a pilot study.

3. EXPERIMENTAL WORK

3.1 Materials, mix proportioning and mixing process

FA-cement (CEM II/B-M 42.5 R) produced by Norcem Company, and un-densified micro silica (Elkem micro silica Grade 940) were used as the main binder. The Mapei Dynamon SX-23 superplasticizer was used as the only additive in the mix (air entraining agent was not used). 12.7 mm chopped basalt fibres and 43 mm macro basalt fibres produced by ReforceTech Company were used. Three sizes of aggregates from a granite source were used in the concrete mixture; Figure 1 shows the proportion of used aggregates. Table 1 shows the composition of the concrete mixtures. As can be seen, the water-binder ratio was 0.34. The reference sample (MIX-0-R) is without fibres and the samples MIX-0.5-C and MIX-0.5-M contain a 0.5-volume percentage of chopped fibres and macro fibres, respectively. A laboratory pan mixer with a maximum capacity of 50 litres was used for the mixing procedure.
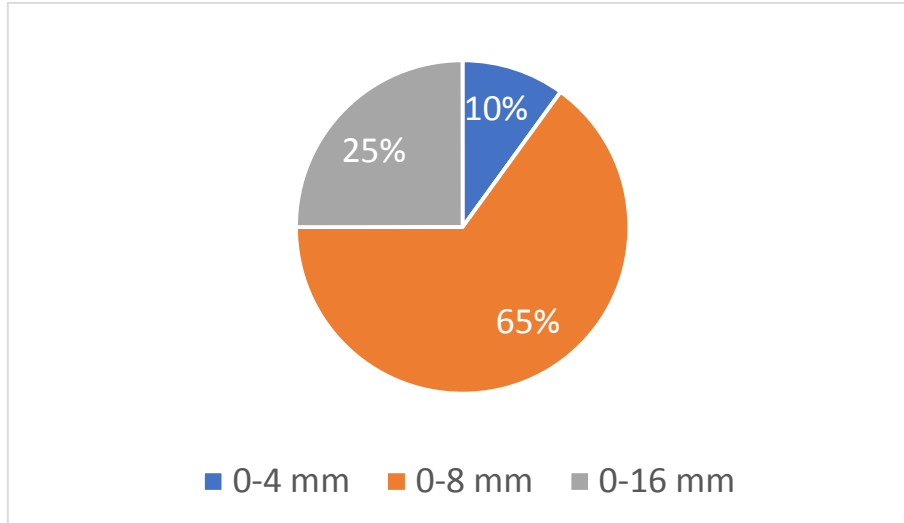
Figure 1 - Proportions of used aggregates.

Table 1 - Concrete mix proportions.

Specimen Code	Cement (kg/m^3)	Silica (kg/m^3)	Filler (kg/m^3)	Sand (kg/m^3)	Gravel (kg/m^3)	Water (litres)	Super plasticizer (kg/m^3)	Fibre (kg/m^3) [%]	W/B[1]
MIX-0-R	495.63	63.19	161.1	1066.61	419.32	190	7.91	[0]	0.34
MIX-0.5-C	495.63	63.19	159.73	1057.73	415.83	190	7.91	10.5 [0.5]	0.34
MIX-0.5-M	495.63	63.19	159.73	1057.73	415.83	190	7.91	10.5 [0.5]	0.34

[1] B is the abbreviation for the binder content of the mix including FA-cement and silica.

3.2 Testing procedure

The experimental programme consisted of three concrete slabs including one reference sample without fibres and two specimens with 0.5 percent of macro and chopped basalt fibres, respectively.

Based on the size of the furnace, three samples with the dimension of 500×600×200 mm including a ring of reinforcement located in the cold rim of the specimen to reduce the cracking were cast. Figure 2 shows the reinforcement mesh and the rebars sizes; it ought to be mentioned that the rebars of the steel reinforcement ring were welded. Furthermore, to measure the compressive strength of concrete, five standard cube samples with side length 100×100×100 mm for each concrete recipe were cast. According to earlier studies [6], it is worth mentioning that the results of this small-scale testing only give an indication of the fire spalling of other types of concrete cross-sections. The results could, therefore, be different from more realistic sample sizes and loading conditions [6].

Before conducting the fire test, all the samples were stored for 28 days in water and 37 days outside of water at room temperature (approx. 18°C), see Figure 3. The temperature of the water was also approximately 18°C. To evaluate the compressive strength, three cube specimens for each concrete type were tested at the age of 28 and 65 days.
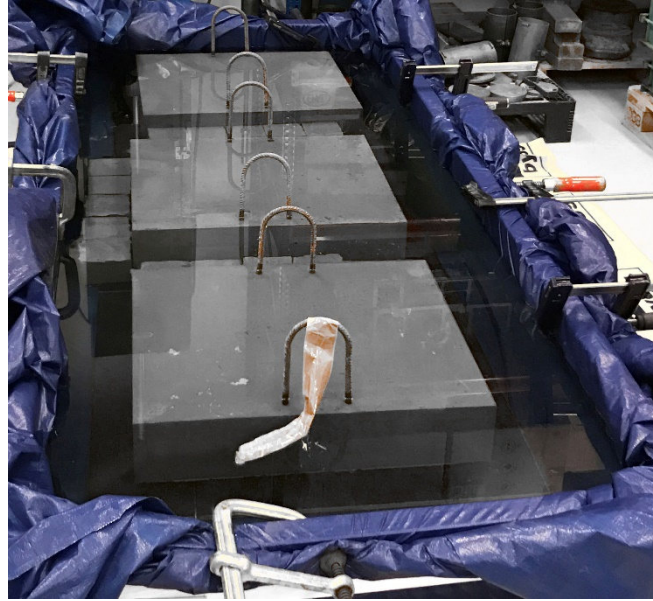
Φ 10

Φ 16

200

150

30

500

Section B-B

Φ 10

Φ 16

200

150

30

600

Secsion A-A

A

45

3 Φ 16

Φ 10

600

510

410

45

B

B

A

500
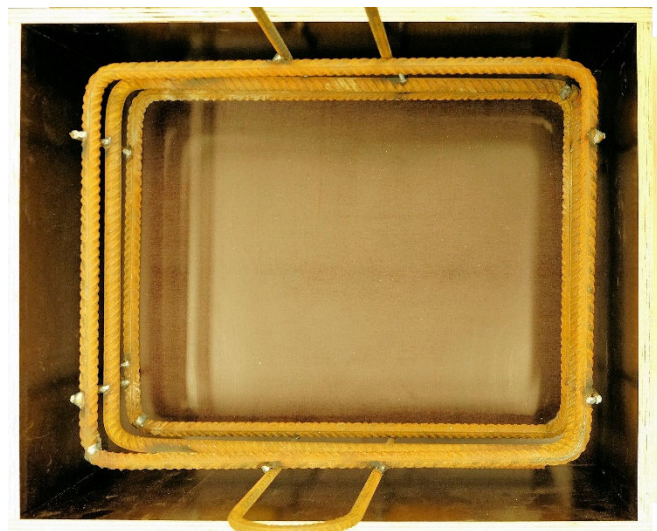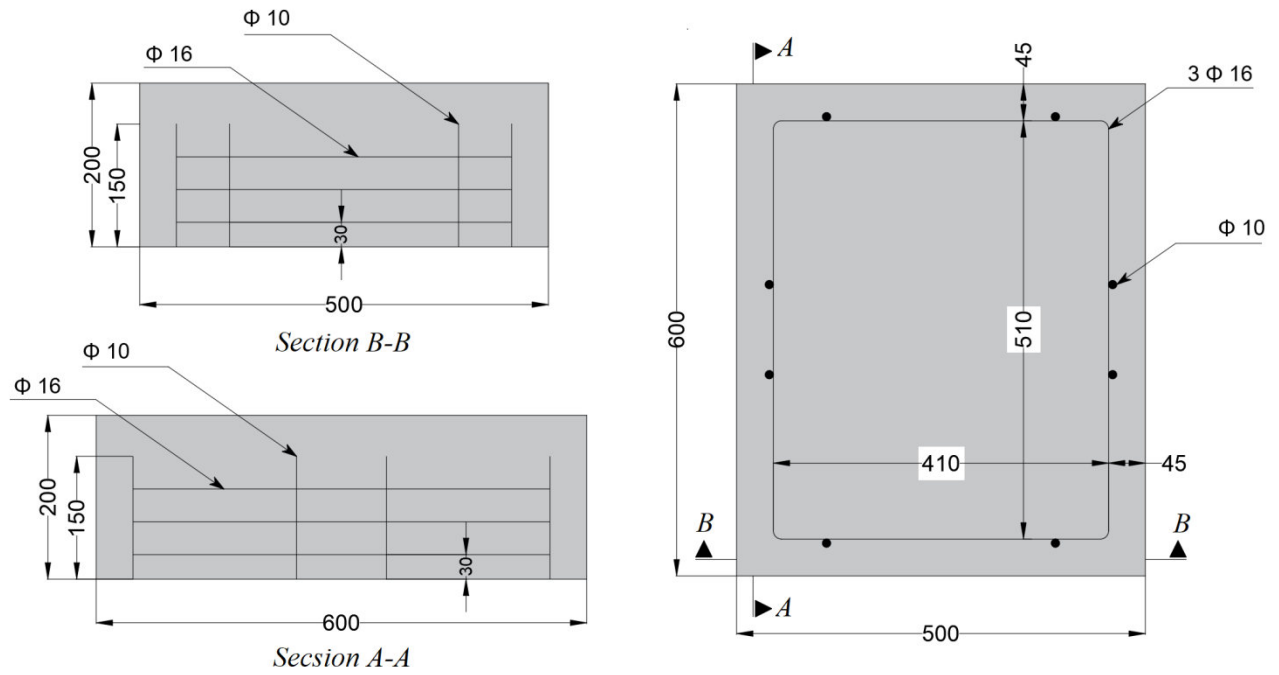
Figure 2 - Geometry of concrete specimens.

Figure 3 - Samples stored in water.

The furnace has an internal space of 500×400×525 mm and an opening area of 500×400 mm, see Figure 4 [31, 32]. The furnace temperature rise measured with a one millimeter shielded type K thermocouple was regulated using a gas flow control based on the standard time-temperature curve as described in the Eurocode [31], see Figure 6. Table 2 shows the different time-temperature fire curve equations defined in the Eurocode 1 [33]. After conducting the tests, the spalling was measured in ten points of the exposed concrete surface. The sampling area was selected in the middle part of the exposed area where the spalling was the highest. Figure 5 shows the sampling area.

Figure 4 - Testing furnace (SP-setup).
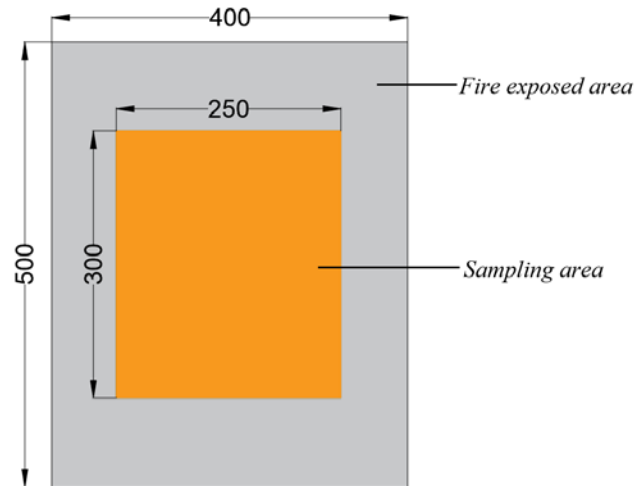
Figure 5 – Sampling area.
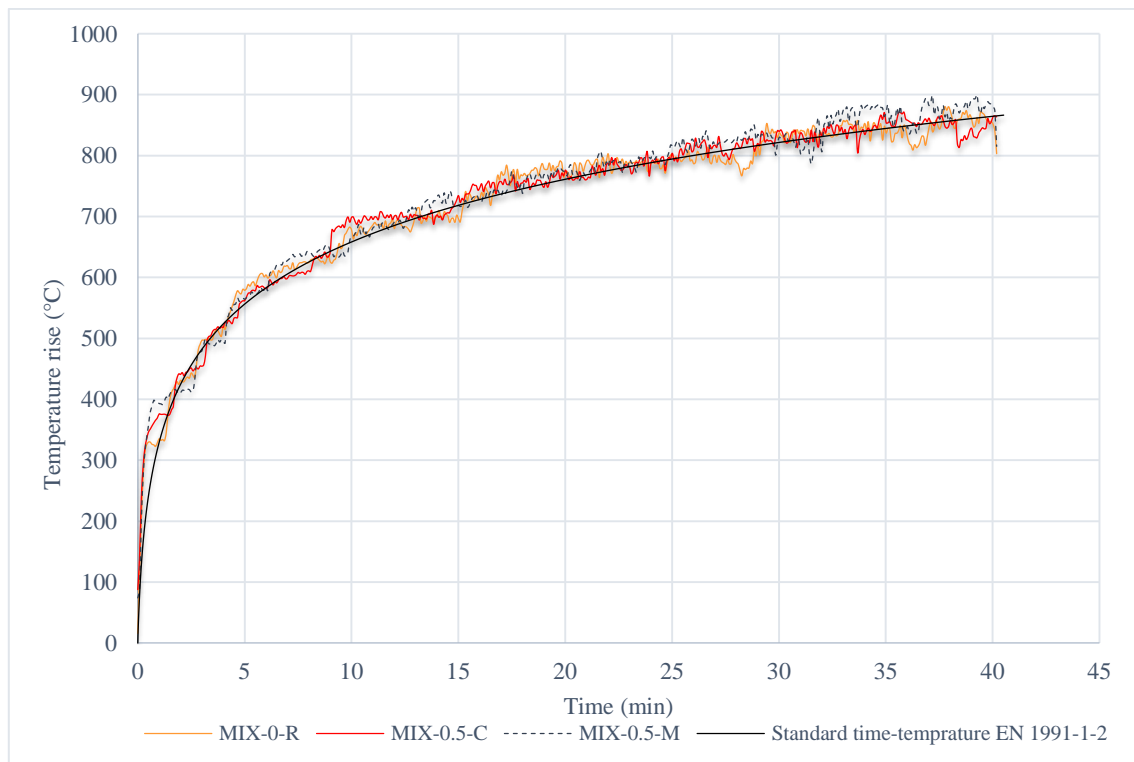
Figure 6 - Furnace temperature rises during the fire-spalling test.

Table 2 - Time-temperature fire curves, from [7, 33].

Type	Mathematical equation[1]
Standard Fire	$\Theta = \Theta_0 + 345 \log(8t + 1)$
Hydrocarbon Fire	$\Theta = \Theta_0 + 1080(1 - 0.325e^{-0.167t} - 0.675e^{-2.5t})$
External Fire	$\Theta = \Theta_0 + 660(1 - 0.687e^{-0.32t} - 0.313e^{-3.8t})$

[1] where t is time (minute), Θ_0 (°C) ambient temperature and Θ (°C) is gas temperature in furnace or close to member.

4.　　　　RESULTS AND DISCUSSION

The mechanical properties, including the average compressive strength and bulk resistivity of concrete cube samples at the age of 28 and 65 days, are presented in Table 3. The results indicate that there are only minor differences between the bulk densities of the concrete samples. The results also show that the specimens reached a compressive strength higher than 100 MPa after 65 days. The bulk resistivity of macro fibre concrete specimen (MIX-0.5-M) shows a slightly lower value. The bulk resistivity presented is an indication of concrete specimens' durability [34, 35].

Table 3 – Mechanical and physical properties of concrete mixtures.

Specimen Code	Bulk wet density (kg/m^3)	Bulk resistivity (Ω.m)	f_{cm}[1] (MPa)	f_{cm}[2] (MPa)
MIX-0-R	2416	434.3	94.9 [1.7][3]	114.5 [2.2]
MIX-0.5-C	2411	446	88.5 [4.3]	117.5 [1.7]
MIX-0.5-M	2428	380	93.2 [1.4]	121 [1.1]

[1] Average compressive strength of concrete at the age of 28 days.
[2] Average compressive strength of concrete at the age of 65 days.
[3] The values in [] show the standard deviation.

The spalling of concrete specimens started when the furnace temperature reached 500°C to 600°C. The progressive flaking of concrete continued during the experiment. The spalling depths were measured after the experiments were completed. The measured values were used as the main parameter for the comparison. The test results do not show any large effect of the basalt fibres on the degree of fire spalling. The average spalling depth was approximately equal for both basalt fibre concrete and the reference concrete mix.

However, the study on the contours of the spalled surfaces is interesting. Figure 7 shows the counter plots of concrete spalling and Figure 8 shows the boxplot diagram of the samples fire spalling depths.

We observe that the spalling seems to be less in some regions of the macro basalt fibre concrete specimen than in corresponding areas in the reference concrete slab. A comparison between the average values of spalling depth shows that the sample containing chopped basalt fibre has the highest spalling value. Figure 9 shows the specimens after fire exposure. As can be noticed, in the first two samples the steel rebars are exposed while the rebars in the third specimen are still covered by concrete. However, since only one sample of each concrete recipe was tested, it cannot be taken as a rule for the distribution of spalling areas. Figure 10 shows the concrete pieces which are connected to the concrete specimen after fire by means of macro fibres.

The visual inspection of the tested specimen shows that the effect of using macro basalt fibres on fire spalling behaviour of the specimens is not significant. The macro basalt fibres in the concrete matrix, when exposed to fire, may behave similarly to the basalt composite in the study performed by Bhat et al. [28]. However, if this assumption is correct, it means that the cement matrix cannot absorb the outcome of the decomposition process or the effect was too small to be comparable to that of the polypropylene fibres.
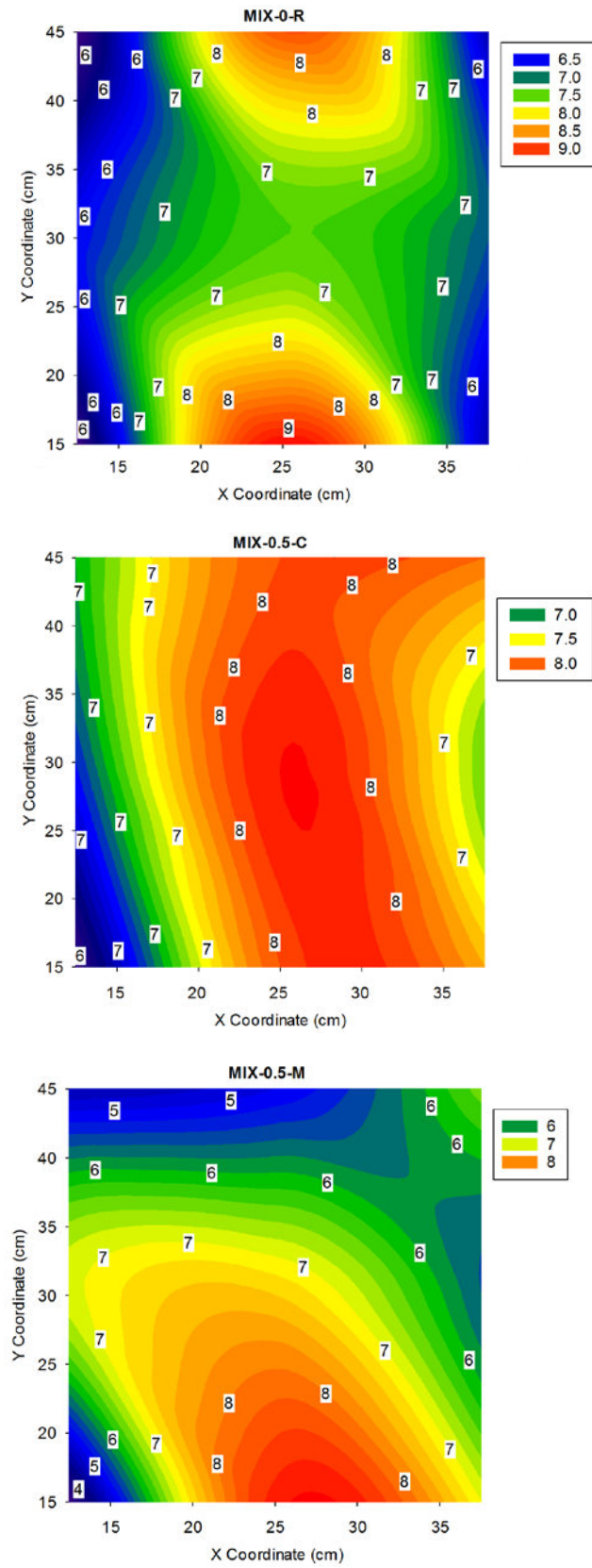
Figure 7 - Contour plot of spalling in concrete samples (in cm).
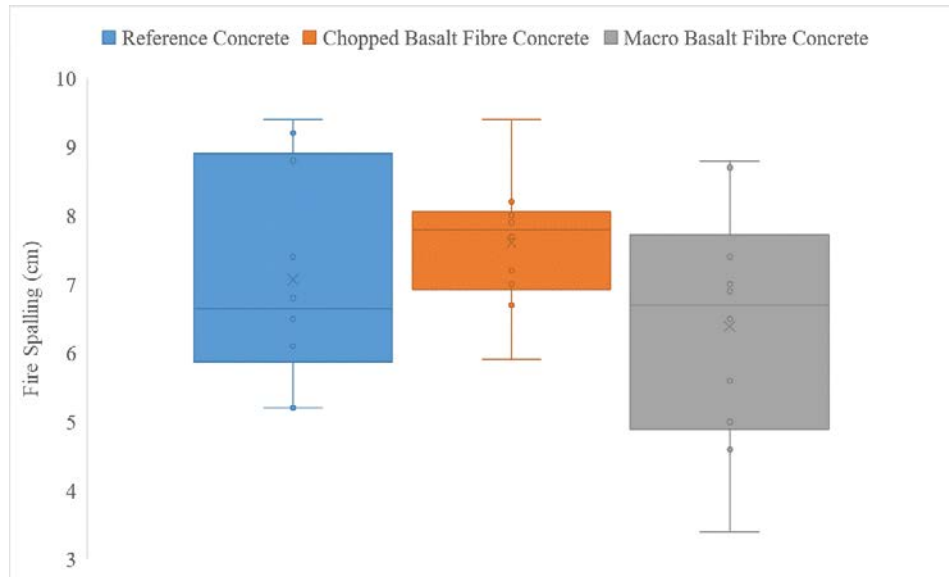
Figure 8 - Box-plot diagram of the fire spalling depth in cm.

The results were also compared via a statistical ANOVA analysis. This analysis has limitations as the natural variation from multiple tests was not investigated are not included, and the use of only 10 measurement points on the surface includes one more random factor. Despite these limitations, it is interesting to determine the differences between the test specimens. The analysis was conducted at the level of significance $\alpha = 0.05$. The result indicates that at this significance level, the difference between the spalling depth of reference specimen and basalt fibre concrete samples is negligible. As can be seen in Figure 7, only the middle section of the exposed area was used for the data sampling. This leads to a conservative statistical analysis result.

Figure 9 - The concrete samples after exposure to fire. (A) *represents MIX-0-R,* (B) *MIX-0.5-C* and (C) *MIX-0.5-M.*

Figure 10 - The concrete pieces are still connected to the main specimen via macro fibres after fire exposure.

High-performance concrete (HPC) is very dense and more prone to fire spalling than conventional concrete. The focus of this study was to characterize the fire spalling properties of high-performance basalt fibre concrete, aimed for marine structures. As stated in the introduction section, spalling increases with decreasing water-binder ratios. The test results from this concrete mix with a water-binder ratio of 0.35 might, therefore, not be representative for concrete with higher water-binder ratios. The conventional concrete is still widely used for other applications. Tests with other water-binder ratios would, therefore, be desirable.

It would also be interesting to conduct a comparative study where the fire spalling of concrete mixes with basalt fibres, steel fibres, and polypropylene fibres could be investigated.

Last but not least, it ought to be mentioned that although a clear beneficial effect of the basalt fibres was not identified, the outcome still has a positive part. Since we still do not know, exactly how concrete behaves under fire conditions, we cannot take for granted that we can mix new materials into the concrete without any detrimental effects. Despite the limited number of specimens, the authors conclude that macro basalt fibres in percentages used in this study do not have any detrimental effect on the resistance against fire spalling compared with an equivalent concrete mix without fibre addition.

5.   CONCLUSIONS AND FUTURE STUDIES

In this paper, the fire spalling properties of basalt fibre concrete were investigated via a pilot experimental program. The effect of two types of basalt fibres on the fire spalling of high-performance concrete was investigated. The experimental investigation was conducted on three concrete slabs and 15 corresponding standard cube samples. The following conclusions can be drawn from the results:

- Based on one single test and 10 measured spalling depths on each slab, a statistical analysis was performed at the level of significance $\alpha = 0.05$. The difference of spalling depth values of macro basalt fibre concrete and the reference concrete was negligible.
- The addition of a 0.5-volume percentage of chopped fibres or macro fibres, both made of basalt, are not likely to prevent the high-performance concrete from fire spalling. However, the addition of basalt fibres did not give any detrimental effect on fire spalling either.

- The good structural properties of macro basalt fibres and the effect of polypropylene fibres in reducing the fire spalling is well-known. It may be possible to enhance both structural properties and fire spalling by using a hybrid fibre reinforced concrete. Thereby, the authors suggest further investigation on fire spalling properties of hybrid fibre concrete made of macro basalt fibres and polypropylene fibres.

ACKNOWLEDGEMENT

REFERENCES

1. Dhand V, Mittal G, Rhee K Y, Park S J & Hui D: "A short review on basalt fiber reinforced polymer composites," *Composites Part B: Engineering*, Vol. 73, 2015, pp. 166-180.
2. Van de Velde K, Kiekens P & Van Langenhove L: "Basalt fibres as reinforcement for composites," *Proceedings*, 10th international conference on composites/nano engineering, University of New Orleans, New Orleans, LA, USA, 2003.
3. Sim J, Park C, & Moon D Y: "Characteristics of basalt fiber as a strengthening material for concrete structures," *Composites Part B: Engineering*, Vol. 36, No. 6-7, 2005, pp. 504-512.
4. Fiore V, Scalici T, Di Bella G & Valenza A: "A review on basalt fibre and its composit,". *Composites Part B: Engineering*, Vol. 74, 2015, pp. 74-94.
5. Jansson, R.: "Fire Spalling of Concrete - Theoretical and Experimental Studies," *Bulletin* No. 117 (Doctoral Thesis), Div. of Concrete Structures, Dept. of Civil & Architectural Engineering, KTH Royal Institute of Technology, Stockholm, 2013.
6. Jansson, R.: "Concrete fire spalling," *Build*, Vol. 142, 2014, pp. 75-76.
7. Hedayati M, Mendis P A, Sofi M & Ngo T: "Fire Spalling of Concrete Members", *Proceedings*, 6th International Conference on Structural Engineering and Construction Management, Kandy, Sri Lanka. 2015.
8. Deeny S, Stratford T, Dhakal R, Moss P, and Buchanan A: "Spalling of concrete: Implications for structural performance in fire," *Proceedings*, International Conference Applications of Structural Fire Engineering, 2009, pp. 202-207.
9. Morita T, Nishida A, Yarnazaki N, Schneider U & Diederichs U: "An Experimental Study on Spalling of High Strength Concrete Elements Under Fire Attack", *Proceedings*, Sixth International Symposium on Fire Safety Science, 2000, pp. 855-866.
10. Pimienta P, Jansson R, Boström L & aMeftah F: "Fire spalling in concrete – The moisture effect", *Proceedings*, MATEC Web of Conferences, part II, Vol. 6, 2013.
11. Jansson R & Boström L: "Fire spalling—the moisture effect," *Proceedings*, 1st International workshop on concrete fire spalling due to fire exposure, 2009.
12. Silfwerbrand J: "Swedish Recommendations for Preventing Fire Spalling in Concrete Structures for Civil Engineering Purposes," Proceedings, 2nd International RILEM Workshop on Concrete Spalling due to Fire Exposure, Delft, The Netherlands, 2011.

13. Hertz K D: "Limits of spalling of fire-exposed concrete," *Fire Safety Journal*, Vol. 38, No. 2, 2003, pp. 103-116.

14. Jansson R & Boström L: "Fire Spalling of Concrete – A Re Assessment of Test Data," *Proceeding*s, 8th International Conference on Structures in Fire, Shanghai, China, 2014.

15. Mugume R & Horiguchi T: "Prediction of fire spalling in fibre-reinforced high strength concrete," *Proceedings,* MATEC Web of Conferences, EDP Sciences, 2013.

16. Kahanji C, Ali F & Nadjai A: "Explosive spalling of ultra-high performance fibre reinforced concrete beams under fire", *Journal of Structural Fire Engineering*, Vol. 7, No. 4, 2016, pp. 328-348.

17. Yermak N P, Pliya P, Beaucour A L, Simon A & Noumowé A "Influence of steel and/or polypropylene fibres on the behaviour of concrete at high temperature: Spalling, transfer and mechanical properties", *Construction and Building Materials*, Vol. 132, 2017, pp. 240-250.

18. Hertz K D & Sørensen L S: "Test method for spalling of fire exposed concrete," *Fire Safety Journal*, Vol. 40, No. 5, 2005, pp. 466-476.

19. Serrano R A, Cobo A, Prieto M I & González M N: "Analysis of fire resistance of concrete with polypropylene or steel fibers," *Construction and Building Materials*, Vol. 122, 2016, pp. 302-309.

20. Klingsch E: "Explosive spalling of concrete in fire," *Doctoral Thesis*, Institute of Strucrtural Engineering, ETH, Zurich, Switzerland, 2014.

21. Salomao R & Pandolfelli V C: "Polypropylene fibers and their effects on processing refractory castable," *International Journal of Applied Ceramic Technology*, Vol. 4, No. 6, 2007, pp. 496-502.

22. Jansson R: "Fire spalling of concrete – A historical overview," *Proceedings*, MATEC Web of Conferences, EDP Sciences, 2013.

23. Jansson R & Boström L: "The Influence of Pressure in the Pore System on Fire Spalling of Concrete," *Fire Technology*, Vol. 46, No. 1, 2009, pp. 217-230.

24. Missemer L, Ouedraogo M Y, Rogat D & Clergue C: "Effect of polymer fibres inclusion in fire spalling of ultra-high performance concrete," *Proceedings*, Fracture Mechanics of Concrete and Concrete Structures, Korea, 2010.

25. Kalifaa P, Chéné C G, Gallé C: "High-temperature behaviour of HPC with polypropylene fibres – From spalling to microstructure," *Cement and Concrete Research*, Vol. 31, 2001, pp. 1487–1499.

26. Mitchell M: "Using fibres in concrete for fire resistance," *Concrete Engineering*, Vol. 1, No. 1, 2007.

27. Eickmeier D: "Structural fire protection with PP-fibre modified concrete in German road tunnels," Proceedings, Young Researchers Seminar, Rome, Italy, 2015.

28. Bhat T V, Chevali V, Liu X, Feih S & Mouritz A P: "Fire structural resistance of basalt fibre composite," *Composites Part A: Applied Science and Manufacturing*, Vol. 71, 2015, pp. 107-115.

29. ReforceTech. Basalt MiniBars Data Sheet. [cited 2017 12 September]; Available from: http://wpstatic.idium.no/reforcetech.com/2016/12/Basalt-MiniBars.pdf.

30. Lourenço L, Barros J & Alves J: "Fiber reinforced concrete of enhanced fire resistance for tunnel segments," *Special Publication*, American Concrete Institute, Farmington Hills, USA, Vol. 276, pp. 1-34.

31. Jansson R & Boström L: "Spalling of concrete exposed to fire," *SP Report* No. 2008:52, SP Technical Research Institute of Sweden, Borås, Sweden, 2008.

32. Jansson R: "Material properties related to fire spalling of concrete," Licentiate Thesis, Division of Building Materials, Lund Institute of Technology, Lund University, Lund, Sweden, 2008.

33. European Standard, EN 1991-1-2: 2002, Eurocode 1: Actions on structures–part 1–2: general actions–actions on structures exposed to fire. 2002.
34. Sengul O: "Use of electrical resistivity as an indicator for durability," *Construction and Building Materials*, Vol. 73, 2014, pp. 434-441.
35. Smith D: "The Development of a Rapid Test for Determining the Transport Properties of Concrete," *Master Thesis*, Unit of Civil Engineering, University of New Brunswick, New Brunswick, Canada, 2006.

Flexural Behaviour of Medium-Strength and High-Performance Macro Basalt Fibre Concrete Aimed for Marine Applications

Ali Mohammadi Mohaghegh
Licentiate, PhD Candidate
Department of Ocean Operations and Civil Engineering
NTNU-Ålesund
P. O. Box 1517, N-6025 Ålesund
Corresponding author: ali.m.mohaghegh@outlook.com

Johan Silfwerbrand
Professor
Department of Civil and Architectural Engineering
KTH Royal Institute of Technology,
SE-100 44 Stockholm

Vemund Årskog
Associate Professor
Department of Ocean Operations and Civil Engineering
NTNU-Ålesund
P. O. Box 1517, N-6025 Ålesund

ABSTRACT

This paper addresses the flexural behaviour of medium-strength, and high-performance concrete (HPC) reinforced with macro fibres made of basalt fibre reinforced polymer (BFRP) with the intended use for marine applications. Mechanical properties of the fibre concrete were studied through an experimental programme consisting of 18 beam specimens and 45-cylinder samples. In this study two types of concrete were used; medium-strength and high-performance concrete with the compressive strength of approximately 60-75 MPa and 90-105 MPa, respectively. The aspect-ratio of the used fibres were 65 and 83, respectively. The experimental results show that the post-cracking properties of macro basalt fibre concrete is a function of the fibre volume content.

Keywords: Macro basalt fibres, high-performance concrete (HPC), flexural behaviour, toughness, ductility, durability, marine structures.

1. INTRODUCTION

For more than a century concrete has been used as a construction material. However, due to its low tensile strength and brittle nature, it traditionally needs to be reinforced with steel bars to meet the structural requirements for concrete structures [1]. For several decades, fibres have

been used to enhance the structural properties of concrete [2-5]. Previous studies indicated that fibres could significantly improve the structural properties of concrete [2-8]. Fibres increase the residual tensile strength of concrete by bridging over the cracks and preventing the cracks to grow [2, 9]. Therefore, due to the enhancement of tensile capacity, fibres can be used as an alternative to rebars.

1.1 The corrosion problem

Finding environmental friendly and sustainable solutions for engineering products is the focus of many research projects in the world, also within the marine construction sector. According to Hooton and Bickley [10], expanding the durability and hence the lifetime of concrete structures is the best approach to improve their sustainability. Metallic materials including steel are prone to corrosion. The corrosion may reduce the durability of structures, thereby their sustainability [11]. Furthermore, it may have adverse economic consequences. Based on the research performed by U.S Federal Highway Administration (FHWA) [11] between 1999 and 2001, the annual cost of corrosion was estimated to be $276 billion whereby the contribution of civil engineering structures was about 8 percent. Furthermore, Zhishena et al. [12] stated that the global corrosion cost of maritime structures caused by sea water is about $700 billion annually. However, FHWA [11] found that correct corrosion control regime may reduce the corrosion cost by 25-30 percent.

In recent years different composite materials and their applications in civil engineering structures have been developed [13]. Sustainable composites, reinforced with natural fibres, such as basalt fibres may be an alternative for steel in corrosive environments [12, 14, 15]. The main objective of this study is to investigate the mechanical performance of Minibars. The Minibars are macro fibres made of basalt fibres encapsulated in a vinyl ester matrix [16].

1.2 Durability of basalt fibres

Basalt fibre (BF) with its natural volcanic origin is known as an eco-friendly, non-toxic material [14]. Russian scientists developed the continuous basalt fibres in 1953-1954 [15]. The first production line of basalt fibres was installed in Ukraine in 1985 [15]. The continuous basalt fibres having diameters of 10-20 μm are produced from the melted basalt rock by an extrusion process, which is similar to the glass fibre (GF) production line [13-15]. The basalt melting temperature is about 1500-1700°C [14]. Producing basalt fibres is cheaper than glass or carbon fibres since it uses less energy and furthermore the input material is only natural volcanic rock and no other additives are needed [15, 17]. The chemical composition of basalt and glass fibres is very similar chemically [18].

In fibre concrete, fibres are exposed to alkali environment of cementitious matrix. Furthermore, the fibres may be in contact with other severe substancies such as seawater. Therefore, fibres shall have a sufficient resistance to chemical degradation [19]. The durability of basalt fibres is under debate. Contradictory opinions are available in the literature whereby few are cited here.

Ramachandran et al. [19] report from a study whereby the durability of basalt, Cem-Fill and E-glass fibres in acidic and alkali environments were examined. Their study showed that soaking of fibres in boiling sodium hydroxide (NaOH) solution did not influence the Cem-Fill and basalt

fibres while the E-glass fibres were corroded. Furthermore, severe degradation has been observed while the basalt fibres were immersed in boiling hydrochloric acid (HCl) [19]. Shuni et al. [18] also found that basalt fibres have a higher chemical stability in alkali solutions than the E-glass fibres.

Lee et al. [20] studied the chemical stability of basalt and glass fibres in alkali solutions where the sizing layer had been removed using acetone. They found that the properties of fibres after the treatment depend on the type of alkaline medium and the immersion period. They also found that, despite substantial weight reduction of basalt fibres in calcium hydroxide $(Ca(OH)_2)$ solution, its tensile strength was reduced drastically.

Moreover, Sim et al. [21] and Scheffler et al. [22] also investigated the durability of basalt and glass fibres in alkali environments. Sim et al. [21] showed that only 20 percent of initial tensile strength is remaining after immersion of fibres in NaOH solution for periods of 28 days. Similarly, Scheffler et al. [22] also found severe degradation in both fibres while they were immersed in alkali solutions. In both studies [21, 22], authors found a brittle layer on the fibre surface. This layer was found to be the result of chemical reaction between SiO_2 and NaOH, however, a different corrosion mechanism was observed when fibres were immersed in cement solution.

Girgin and Yıldırım [23] investigated the durability of cement composites reinforced with basalt and glass fibres. They found that after 50 cycles of hit-rain ageing test, degradation of mechanical characteristics in BF cement composite was more than that of the GF composite. However, no trace of deterioration on the surface of fibres was reported [23].

Wei et al. [24] studied the corrosion mechanism of basalt and glass fibre composites encapsulated in epoxy resin. The composites were immersed in the seawater for 90 days. The authors found that the degradation of composites is due to the penetration/diffusion of ions into the composite matrix and hydrolise of its components. They also found that after the treatment, BFRP composite maintained about 70 percent of its primary tensile strength.

1.3 Mechanical properties of basalt fibre concrete

Mechanical properties of chopped basalt fibre concrete have been subject to several studies whereby some are cited here. High et al. [25] investigated the mechanical properties of chopped basalt fibre concrete, whereby mixes with water-cement ratios of 0.55 and 0.38 were tested. They found that basalt fibres can significantly improve the flexural capacity of concrete, especially for mixes with the low water-binder ratio.

Kizilkanat et al. [26] report from a study whereby 12 mm chopped basalt and glass fibre concrete with a water-cement ratio of 0.45 were examined. The authors found that adding one volume percent of chopped fibres increases the fracture energy by 50 percent. Moreover, Kabay [27] show that adding basalt fibres may significantly improve the abrasion resistance as well as the fracture energy of concrete.

Jing et al. [28] investigated the effect of fibre content and fibre aspect-ratio on mechanical properties of chopped basalt fibre concrete. They found that flexural strength and toughness are functions of fibre dosage and aspect ratio. However, Ayub et al. [29] found that using more than 2 percent of chopped fibres may increase the void content and consequently reduce the compressive strength.

Li and Xu [30] studied the high-strain-rate properties of basalt fibre reinforced geopolymeric concrete. They found that increasing the strength of matrix may increase the energy absorption capacity while reducing the ductility of fibre concrete [31]. They also concluded that adding fibres may impair the interfacial bonding between the aggregates and the matrix and therefore having an adverse effect on the dynamic compressive strength of concrete [30, 31].

2. RESEARCH SIGNIFICANCE, AIMS AND SCOPE

Several studies have investigated the mechanical properties of chopped basalt fibre concrete. All these studies acknowledge the positive effect of chopped basalt fibres on mechanical properties of concrete. Contrary, very little research is reported about the mechanical properties of macro basalt fibre concrete and the use of this type of fibres for structural applications. Based on the literature review, there are contradictory results regarding the durability of basalt fibres in the severe environments. Previous studies show that the durability of basalt fibres depends on the raw material, production process, sizing, diameter of fibres, etc [32]. Furthermore, in basalt fibre composites, it also depends on the properties of polymeric matrix encapsulating the fibres. Industrial experiences showed that vinyl ester composites are resistant to chemical degradations [33]. Minibar macro fibres and basalt fibre rebars are vinyl ester-basalt composites that may be a potential alternative for steel in corrosive environments. Motivated by these insights and a research mission to improve the durability of marine concrete structures, mechanical properties of macro basalt concrete for marine concrete structures are subject to investigation. More specifically, the paper provides findings pertaining the effect of fibre content, fibre aspect ratios and concrete compressive strength on the post-cracking behaviour of macro basalt fibre concrete. It worth mentioning that durability of macro basalt fibres and rebars need to be verified through further experiments, however, this is not in the scope of this paper.

3. EXPERIMENTAL PROGRAM

3.1 Materials, mix proportioning and mixing process

A Norwegian cement containing fly ash (FA), termed *Standardsement FA*, provided by the Norwegian company Norcem, has been used in this study. *Standardsement FA* contains 19.2% fly ash and 1.7% free lime and satisfies the requirements of NS-EN 197-1:2011 for the Portland CEM II/B-M 42.5R. Physical properties and chemical composition of the cement are given in Table 1. Additionally, micro silica provided by the Norwegian company FESIL was used as a part of binder content. Crushed granite with a maximum aggregate size of 16 mm was used as coarse aggregate. Properties of the aggregates are given in Table 2. The surface dry density of filler (0-4 mm), sand (0-8 mm) and gravel (0-16 mm) were 2660 kg/m^3, 2710 kg/m^3 and 2770 kg/m^3, respectively. A polycarboxylate ether based superplasticizer Mapei Dynamon SX-23 was applied in the mix. The investigation was carried out on 43 mm and 55 mm straight macro basalt fibres with a helical shape provided by the Norwegian company ReforceTech. The macro basalt fibres had a diameter of 0.65 mm and a density of 2100 kg/m^3 [16]. The tensile strength and the elastic modulus were 1000 MPa and 44 GPa, respectively [16]. The number of fibres per kg was 27400 and 21600 for 43 and 55 mm fibres, respectively. The concrete mixes were developed to satisfy the requirements to medium-strength and high-performance concrete. According to DNV-OS-C502 [34], the water-binder ratio of concrete mixes for marine applications is limited to 0.4 for the members in the splash zone and 0.45 for the other parts. For the medium-strength concrete, to investigate the effect of silica content on the mechanical properties of the concrete

matrix, three different water-binder ratios were used. For the high-performance concrete, a water-binder ratio of 0.254 was used. Based on the study performed by Kabay [27], void content can affect the mechanical properties of fibre concrete. Therefore, to limit the number of effective parameters on the flexural behaviour, use of air entering agent is outside of the scope of this study. Based on a literature study Yazici et al. [35] stated that 0.5-2.5 volume percent is the recommended value for the fibre content. However, for offshore structures, DNV-OS-C502 [34] limited the use of fibres to 2%. Therefore, in this study, the fibre content was selected in the range of 0.5% to 2%. For the HPC-II-2 concrete mix (Table 4), fibres with a length of 43 mm were used. All the other concrete mixes were produced with 55 mm fibres. The composition of the concrete mixes is presented in Table 2.

Table 1 - Physical properties and chemical composition of the cement [36].

		Chemical composition (%)	
Compressive strength (MPa)		CaO	51.01
1 day	22.0	SiO_2	25.98
2 days	32.7	Al_2O_3	8.25
7 days	42.6	Fe_2O_3	3.94
28 days	53.8	K_2O	1.15
		Na_2O	0.54
Physical properties		MgO	2.18
Specific gravity (kg/m^3)	3000	Na_2O Eq.	1.30
Specific surface (cm^2/g)	4500	TiO_2	0.423
Volume expansion (mm/m)	1	P_2O_5	0.250
Setting time (start) min	154	Mn_2O_3	0.061
		SO_3	3.40
		Cl^-	0.061
		$\Sigma =$	97.2

Table 2 - Particle size distribution data of the used aggregates.

	Cumulative (%) finer than		
Sieve size (mm)	0-4 mm	0-8 mm	0-16 mm
16	100	100	91.13
11.2	100	100	39.03
8	100	98.45	8.00
4	96.25	81.42	3.65
2	74.41	66.73	3.10
1	58.97	50.88	2.86
0.5	46.15	33.17	2.60
0.25	33.1	18.07	2.23
0.125	19.95	8.25	1.68
0.063	9.89	2.58	1.06

Table 3 - Concrete mix proportions.

Mixture Code	Cement (kg/m^3)	Silica (kg/m^3)	Filler (kg/m^3)	Sand (kg/m^3)	Gravel (kg/m^3)	Water (litres)	Super plasticizer (kg/m^3)	Fibre (kg/m^3) [%][3]	W/B[1]
MSC-I	473.36	40.24	167.10	1037.55	444.38	205	6.98	19.74 [0.94]	0.4
MSC-II	473.36	60.36	167.10	1037.55	444.38	197	6.98	19.74 [0.94]	0.369
MSC-III	496.80	42.23	172.50	1071.34	458.86	207	7.33	41.43 [1.97]	0.384
HPC-I	780.67	99.53	132.34	821.87	352	197	26.4	14.81 [0.71]	0.224
HPC-II[2]	780.20	99.47	131.59	817.20	350	197	26.39	19.74 [0.94]	0.224
HPC-III	780.20	99.47	128.93	800.46	342.83	197	26.39	39.48 [1.88]	0.224

[1] B is the abbreviation for the binder content of the mix including FA cement and silica.
[2] HPC-II mix was used for the fibre size of 43 mm and 55 mm.
[3] The values in the bracket are the fibre volume fraction.

mixer, and a constant speed of 27.9 rpm was used in the entire mixing process. The process started by mixing all the dry ingredients and followed by adding the water and superplasticizer. The mixing process continued until a uniform consistency was obtained. As the final step, fibres were added manually at a constant rate of approximately 5 g/s.

3.2 Sample preparation and testing procedure

To investigate the flexural properties of concrete mixes and due to the mixer capacity, two replicate prismatic specimens with the dimensions of 150×150×550 mm and five-cylinder specimens with a diameter of 100 mm and height of 200 mm were cast. A small-scale concrete vibrator was used to obtain the necessary compaction. Since the operation of marine structures, specifically concrete barges, starts minimum two months after the construction of the concrete part is completed, the hardened properties were also evaluated after sixty days. A plastic layer covered the specimens for the first 24 hours before demolding. All samples were cured in 18ºC water before performing the hardened concrete experiments at the age of 28 and 60 days.

The compressive strength test was carried out according to the standard NS-EN 12390-3 [37] with a loading rate of 6.28 kN/s. ASTM and European standards present three different methods for evaluation of the fibre concrete; ASTM C1399/C1399M-10 [38], ASTM C1609/C1609M-12 [39] and the European standard for measuring the flexural tensile strength of metallic fibre concrete; EN 14651 [40]. In our study, we followed the EN 14651 [40] procedure and RILEM TC 162-TDF [41-43] recommendations.

The three-point bending test was performed using a locally assembled testing machine with a 75 kN upward moving table and an immovable 200 kN load cell unit. All the beam specimens were notched on the bottom side after 90º rotation around the longitudinal axis. The mid-span deflection was measured using two linear variable displacement transducer (LVDT) sensors placed on two sides of the beam; additionally, the crack mouth opening displacement (CMOD) was measured simultaneously by means of a clip gauge installed in the notch centre, see Figure 1. It ought to be mentioned that the test set up was designed in a way that the roller support could rotate freely. A 50 Hz acquisition system was used to obtain and register the data. For safety reasons, the tests were stopped before the final beam failure.
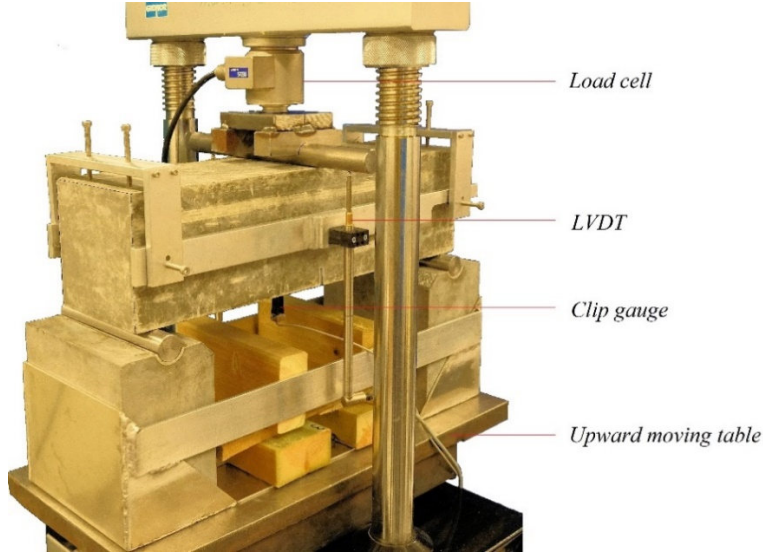
Figure 1 - Experimental set-up of three-point bending test according to EN-14651 [40].

4. EVALUATION OF FLEXURAL BEHAVIOUR

4.1 Equivalent and residual flexural tensile strength

According to RILEM TC 162-TDF [43] and NS-EN 14651:2005 [40] the flexural strength of the fibre concrete is characterized based on the load-crack mouth opening displacement (CMOD) curve at specified reference points [5]. In this study, the flexural strength of the limit of proportionality (LOP) and residual strength of the reference points were calculated by use of Eq. (1) and, Eq. (2), respectively [40].

$$f_{ct,L}^{f} = \frac{3}{2} \frac{F_L l}{b h_{sp}^2}$$
(1)

$$f_{R,j} = \frac{3}{2} \frac{F_j l}{b h_{sp}^2}$$
(2)

F_j (j = 1, 2, 3, 4) is the load at CMOD = 0.5, 1.5, 2.5 and 3.5 mm, respectively.

F_L is the load corresponding to the LOP and defined as the highest load value corresponding to CMOD $\leq$ 0.05 mm [43]. Also, l, b and h_{sp} are the beam length, width and height of the fracture cross section, respectively [40]. Barros et al. [44] reported a significant scatter of f_R values and based on their study; they concluded that the equivalent flexural tensile strength (f_{eq}) concept should be used instead of the f_R concept. Hence, in our investigation, we used both f_{eq} and f_R values to assess the post-cracking behaviour of macro basalt fibre concrete. According to RILEM TC 162-TDF [43] and Barros et al. [44], two parameters of $f_{eq,2}$, Eq. (3), and $f_{eq,3}$, Eq. (4), were calculated based on the allowable deflections of the serviceability limit state and ultimate limit state. These parameters are both functions of the energy absorption capacity of the fibre concrete at specified points [43, 44].

$$f_{eq,2} = \frac{3}{2} \frac{D_{BZ,2}^f}{0.5} \frac{l}{b h_{sp}^2}$$
(3)

$$f_{eq,3} = \frac{3}{2} \frac{D_{BZ,3}^f}{2.5} \frac{l}{bh_{sp}^2} \tag{4}$$

$$D_{BZ} = \int_0^{\delta_i} F(\delta)d\delta \tag{5}$$

$D_{BZ,2}^f = D_{BZ2} - D_{BZ}^b$ and $D_{BZ,3}^f = D_{BZ3} - D_{BZ}^b$, the values of energy absorption capacity corresponding to the deflection of ($\delta_2 = \delta_L + 0.65$ mm) and ($\delta_3 = \delta_L + 2.65$ mm), and D_{BZ}^b the energy absorption capacity of uncracked concrete are shown in Figure 2 [42, 43]. δ_L is the value of the mid-span deflection corresponding to the limit of proportionality [42, 43]. The energy absorption capacity of the fibre concrete up to the point (i) is calculated by use of Eq. (5) [45]. These equations are valid only if 0.5 and 2.5 are given in mm, D_{BZ}^f in Nmm and l, b, h_{sp} in mm. Thus, f_{eq} is given in MPa.

(a)

(b)
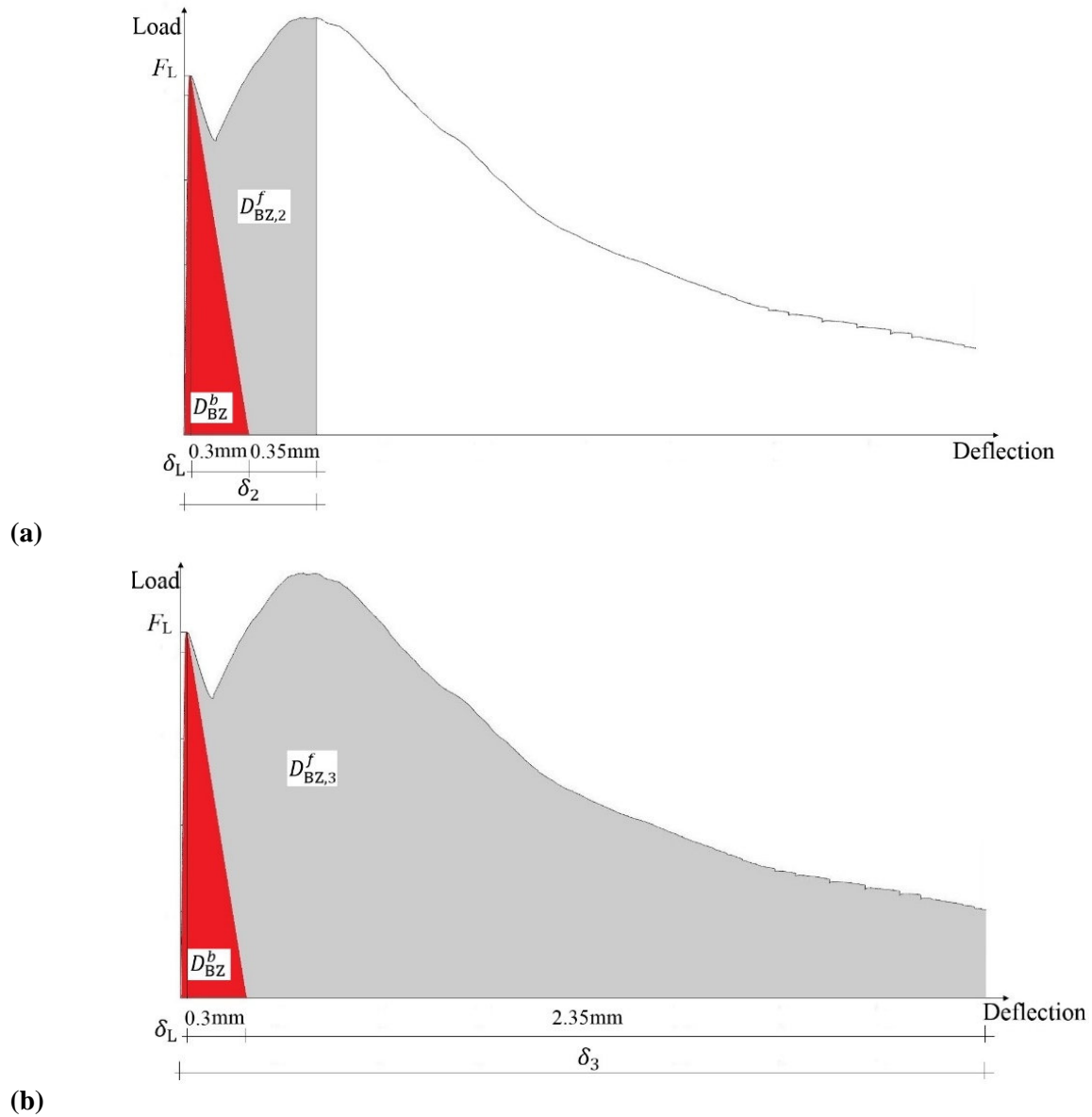
Figure 2 - Definition of (a) $D_{BZ,2}^f$; and (b) $D_{BZ,3}^f$ adapted from Barros et al. [44] and RILEM TC 162-TDF [42, 43].

4.2   Ductility indication

For concrete beams reinforced with steel rebars, the ductility is defined as the ratio of mid-span deflection of collapse to the deflection at the rebars' yielding point [46, 47]. However, this definition is not suitable to evaluate the ductility of fibre concrete beams. In different articles, a variety of parameters are used for evaluation of the ductility in the fibre concrete elements [48-51]. In this study, the ductility is defined by Eq. (6) being the ratio of energy absorption capacity of fibre concrete to the energy absorption capacity of un-cracked concrete. Eq. (6) is adapted from Olivito and Zuccarello [48], Akcay and Tasdemir [50].

$$I_{\text{ductility}} = \frac{D_{\text{BZ}}^{b} + D_{\text{BZ,3}}^{f}}{D_{\text{BZ}}^{b}}$$
(6)

5.   RESULTS AND DISCUSSION

5.1   Compressive strength and bulk density

For all samples, properties of hardened concrete are summarized in Table 4 for the age of 28 days, but HPC-I-2 is reported for 60 days. Based on the presented results in Table 4, the fibre content has a minor influence on the density. The concrete mixes were designed based on the volume fraction of ingredients and the aggregate content varied for different combinations. Therefore, the effect of fibre content on compressive strength cannot be evaluated in this study.

5.2   Bulk electrical resistivity

According to Layssi et al. [52], the degree of porosity and conductivity of pore solution in concrete directly affects its permeability, chloride ingress resistance, therefore its durability. The bulk electrical resistivity can be used to characterize the degree of conductivity of the concrete microstructure [52]. In this study, to indirectly assess the durability of specimens in the marine environment, uniaxial-alternating current (AC) was used to measure the resistance R (Ω) value of the cylindrical specimens. Bulk electrical resistivity was calculated by Eq. (7) [53, 54].

$$\rho = R \frac{A}{L}$$
(7)

where A (m^2) is the surface area of the samples and L (m) is the length of specimens [53, 54]. The values of electrical resistivity of the hardened specimens are presented in Table 4.

Table 4 - Mechanical and physical properties of concrete mixtures.

Mixture Code and Batch[1]	Bulk wet density[2] (kg/m^3)	Bulk resistivity[2] (Ω.m)	f_{cm} (MPa)
MSC-I	2452 [14.1]	209.5 [6.3]	61.3 [2.24]
MSC-II	2425 [24.6]	284.4 [16.5]	75.7 [1.34]
MSC-III-1	2449 [5.5]	220.8 [7.3]	65.7 [1.39]
MSC-III-2	2484 [25.9]	225.8 [3.8]	67.8 [1.30]
HPC-I-1	2450 [20.4]	725.7 [29.2]	96.8 [2.15]
HPC-I-2[3]	2450 [19.7]	1210.6 [71.1]	106.8 [3.81]
HPC-II-1	2452 [41.3]	509.4 [4.9]	91.9 [2.94]
HPC-II-2	2421 [34.7]	482.5 [15.3]	96.4 [2.13]
HPC-III	2378 [8.5]	556.3 [20.2]	90.7 [2.55]

[1] Since the capacity of the concrete mixer was not enough for more than two beams and five concrete cylinders, the specimens B5-B14 were made from similar recipes but different batches.
[2] Bulk density and bulk resistivity of concrete cylinders were measured before compression test, and the average values are reported. The values in [] show the standard deviation.
[3] The mechanical and physical properties of the mix HPC-I-2 at the age of 60 days are presented.

Smith [55] recommended a classification for the risk of chloride ingress in concrete based on the bulk resistivity. He found that concrete with a bulk resistivity higher than 170 Ω.m indicates very low risk and therefore high durability in marine environments [55].

5.3 Flexural behaviour

With the data collected during the experiments, the load-CMOD curves were plotted. Figure 2 to Figure 6 show the load-CMOD curves of the beams reinforced with different fibre content, fibre aspect ratio and matrix compressive strength. Table 5 summarises the test results in different loading steps. As it can be seen, the fibre content does not have a noticeable effect on the load corresponding to the limit of proportionality (LOP), but F_L slightly increased by increasing the compressive strength. As it was expected, an increasing trend was observed by increasing the fibre content.

Figure 2 shows the results of flexural testing on samples with same composition but from different batches. The compressive strengths are slightly different, but the difference in post-cracking properties is more pronounced. The difference may be due to the distribution and directions of fibres in the concrete specimens.

Based on Figure 4, the sample tested at 60 days shows a slight increase in the value of F_L due to the increase in the tensile strength. However, the difference in post-cracking properties is not distinctive. Figure 5 shows the result of concrete reinforced with 43 mm ($\frac{l_f}{d}$ =65) and 55 mm ($\frac{l_f}{d}$ =84) fibres. A comparison between the experimental results of 43 mm and 55 mm fibre concrete shows that increasing the aspect ratio leads to higher anchorage length and consequently an increase in post-cracking peak and $f_{eq,2}$ values. However, the concrete reinforced with $\frac{l_f}{d}$ =65 shows a wider deflection-hardening zone and $f_{eq,3}$ value.
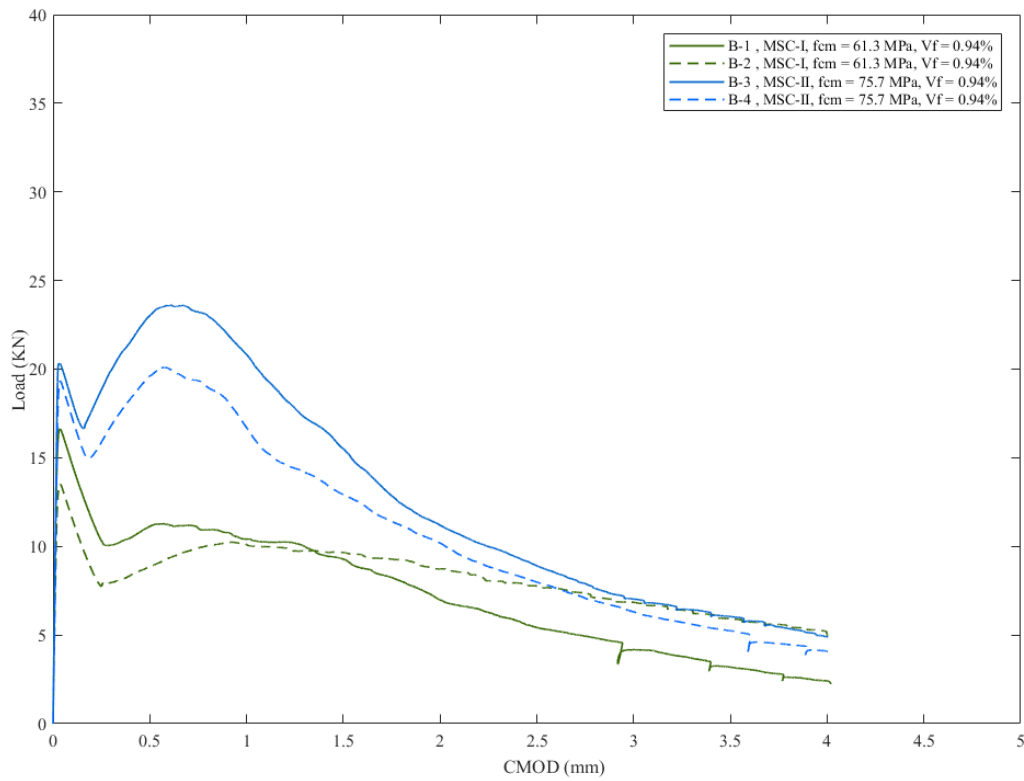
Figure 2 - Load-CMOD curves of basalt fibre concrete under flexural test, with a fibre content of 0.94 % volume fraction and average concrete compressive strengths of 61.3 MPa and 75.7 MPa.
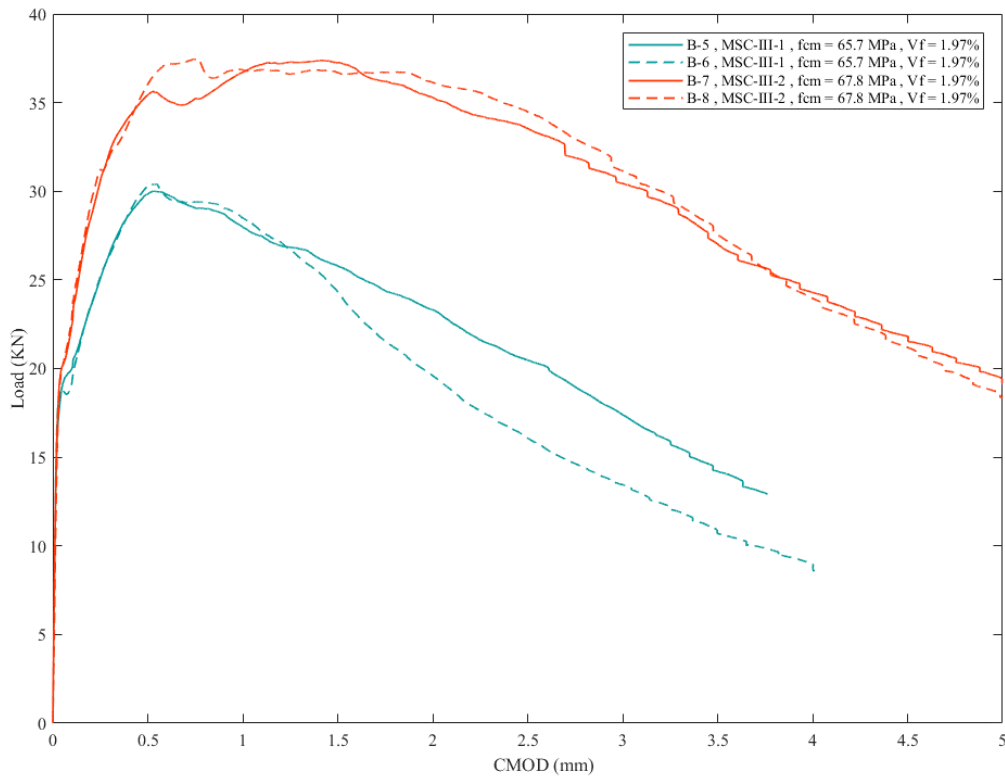

Figure 3 - Load-CMOD curves of basalt fibre concrete under flexural test, with a fibre content of 1.97 % volume fraction and average concrete compressive strengths of 65.7 MPa and 67.8 MPa.
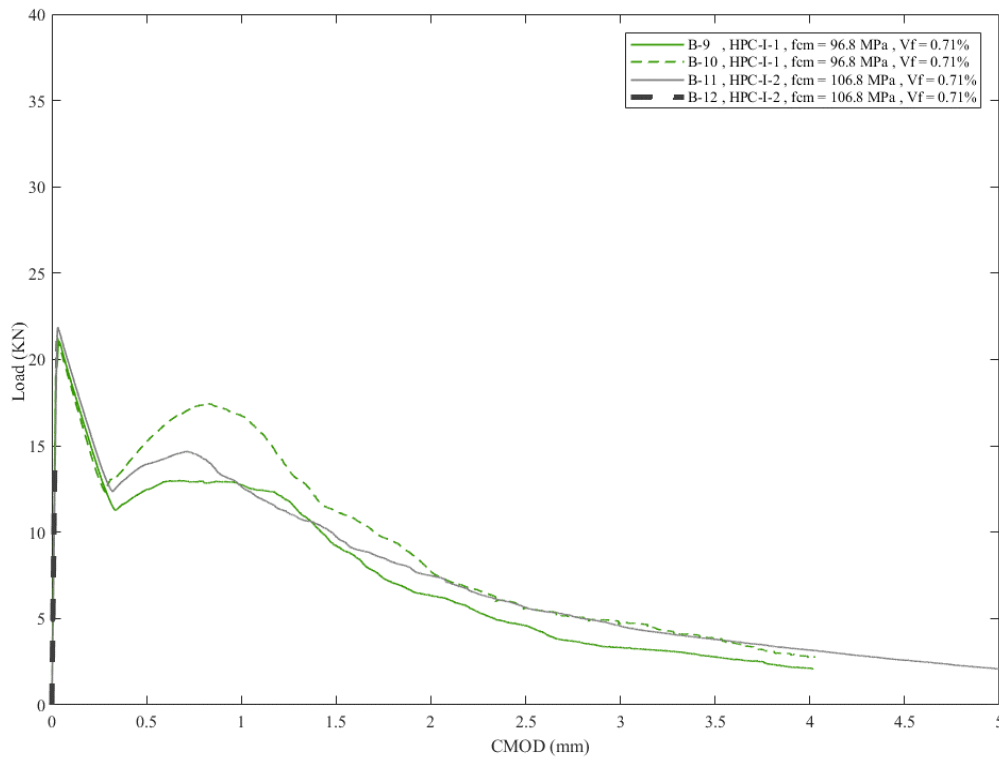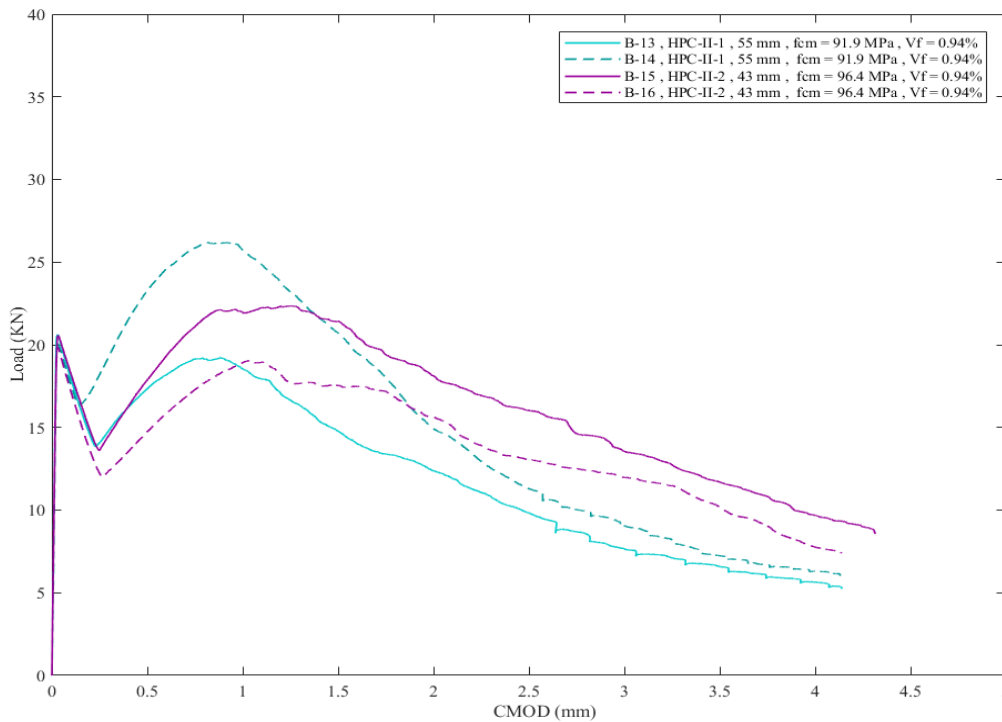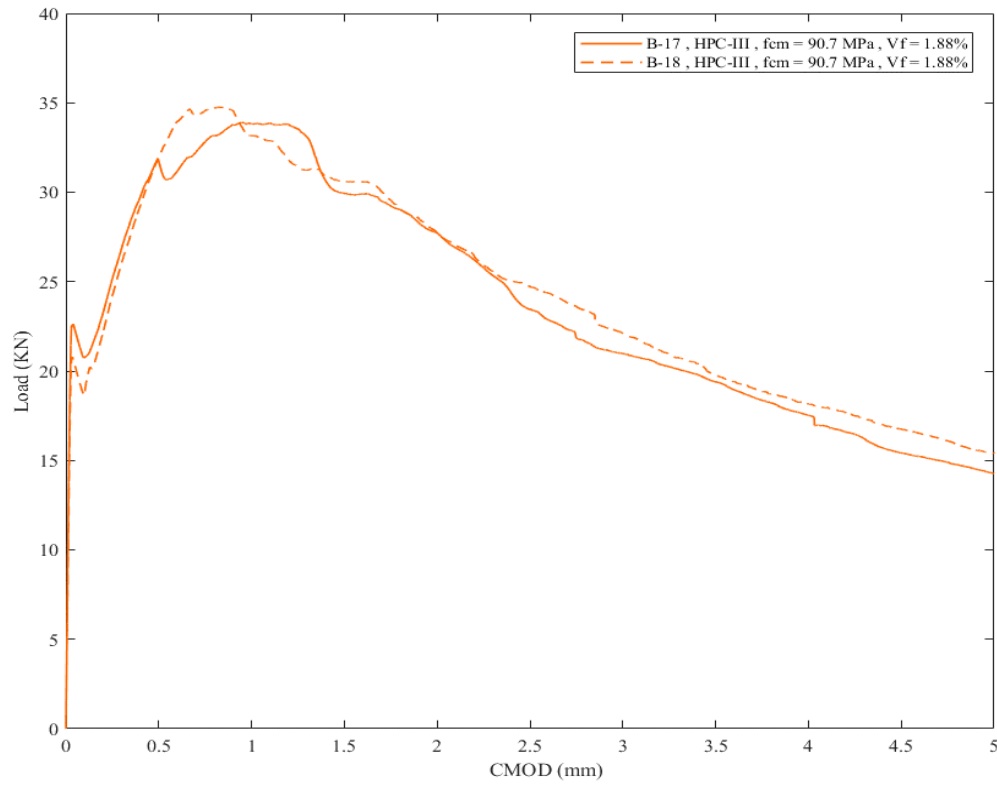
Figure 4 - Load-CMOD curves of basalt fibre concrete under flexural test, with a fibre content of 0.71 % volume fraction and average concrete compressive strengths of 96.8 MPa and 106.8 MPa.

Figure 5 - Load-CMOD curves of basalt fibre concrete under flexural test, with a fibre content of 0.94 % volume fraction and average concrete compressive strengths of 91.9 MPa and 96.4 MPa.

Figure 6 - Load-CMOD curves of basalt fibre concrete under flexural test, with a fibre content of 1.88 % volume fraction and average concrete compressive strength of 90.7 MPa.

Table 5 - Experimental results of peak and post-cracking parameters of test specimens.

Beam Code	Used Mixture	$f_{\text{fct,L}}$ (MPa)	f_{R1} (MPa)	f_{R2} (MPa)	f_{R3} (MPa)	f_{R4} (MPa)	$f_{\text{eq,2}}$ (MPa)	$f_{\text{eq,3}}$ (MPa)
B-1	MSC-I	5.32	3.56	2.97	1.73	1.02	3.19	2.47
B-2	MSC-I	4.32	2.82	3.10	2.49	1.90	2.61	2.69
Average B1-B2	MSC-I	4.82	3.19	3.04	2.11	1.46	2.90	2.58
B-3	MSC-II	6.51	7.37	4.96	2.85	1.93	6.92	4.56
B-4	MSC-II	6.19	6.28	4.13	2.55	1.68	5.72	3.71
Average B3-B4	MSC-II	6.35	6.83	4.55	2.70	1.81	6.32	4.14
B-5	MSC-III-1	6.09	9.56	8.25	6.55	4.54	9.26	7.70
B-6	MSC-III-1	5.96	9.69	7.78	5.15	3.42	9.24	7.09
Average B5-B6	MSC-III-1	6.03	9.63	8.02	5.85	3.98	9.25	7.40
B-7	MSC-III-2	6.44	11.34	11.92	10.73	8.65	11.39	11.09
B-8	MSC-III-2	6.44	11.53	11.74	11.03	8.82	11.49	11.24
Average B7-B8	MSC-III-2	6.44	11.44	11.83	10.88	8.74	11.44	11.17
B-9	HPC-I-1	6.75	3.99	2.95	1.47	0.89	3.67	2.52
B-10	HPC-I-1	6.85	4.87	3.58	1.79	1.24	6.57	3.57
Average B9-B10	HPC-I-1	6.80	4.43	3.27	1.63	1.07	5.12	3.05
B-11[d]	HPC-I-2	6.99	4.46	3.12	1.81	1.21	4.09	2.76
B-12[d]	HPC-I-2	-	-	-	-	-	-	-
Average B11-B12	HPC-I-2	6.99	4.46	3.12	1.81	1.21	4.09	2.76
B-13	HPC-II-1	6.60	5.55	4.73	3.14	2.11	5.12	4.19
B-14	HPC-II-1	6.43	7.45	6.63	3.61	2.32	7.32	5.38
Average B13-B14	HPC-II-1	6.52	6.50	5.68	3.38	2.22	6.22	4.79
B-15	HPC-II-2	6.58	5.72	6.85	5.13	3.74	5.90	5.35
B-16	HPC-II-2	6.36	4.73	5.61	4.18	3.27	4.50	4.65
Average B15-B16	HPC-II-2	6.47	5.23	6.23	4.66	3.51	5.20	5
B-17	HPC-III	7.24	10.16	9.58	7.50	6.21	9.69	8.71
B-18	HPC-III	6.66	10.22	9.79	7.91	6.34	9.89	8.83
Average B17-B18	HPC-III	6.95	10.19	9.69	7.71	6.28	9.79	8.77

[d] The B-11 and B-12 were tested at the age of 60 days.

Many researchers [44, 56-58] have investigated the relationship between aspect ratio, shape, volume fraction, the number of fibres in the fracture cross-section, bonding properties, concrete compressive strength and the mechanical properties of steel fibre reinforced concrete. Previous studies [59] show that post-cracking properties of steel fibre concrete can be presented as a function of the number of fibres, fibre volume fraction and the fibre aspect ratio.

In this study, the Pearson product-moment coefficient [60] was used to find the relationship between concrete compressive strength, fibre content, ductility and post-cracking properties of fibre concrete. The ratio $V_{\text{f}} f_{\text{cm}}^{\frac{1}{n}}$ is assumed to be the primary parameter for estimation of the properties. There are only a limited number of results available regarding the two different fibre lengths studied here, therefore, the fibre aspect ratio is not considered in this comparison. Furthermore, concrete compressive strength is used to indirectly include the concrete bonding properties. This assumption is based on Eurocode 2 [61], whereby the bonding strength of steel rebars to the concrete matrix is presented as a function of concrete compressive strength.

A large number of *n* values (*n* = 1 to 100) were examined and the best correlation for ductility was found for *n* = 2. For the post-cracking properties, the best correlation was found by using *n* = 3. Table 6 and Figures 7 to 9 show the relationship between these properties. According to the fib Model Code 2010 [62], for structural purposes, fibre concrete can be used as a replacement

for the conventional rebars if the following equations are satisfied for the characteristic values of post-cracking parameters:

$$\frac{f_{R1K}}{f_{LK}} > 0.4 \tag{8}$$

$$\frac{f_{R3K}}{f_{R1K}} > 0.5 \tag{9}$$

Barros et al. [44] showed that there is a linear relationship between f_{R1} and f_{R4} also between f_{eq2} and f_{eq3}. Table 5 shows the same set of correlations between these parameters for macro basalt fibre concrete. The structural capacity of fibre concrete can be estimated based on the results presented in Table 5 and the equations presented in Table 6.
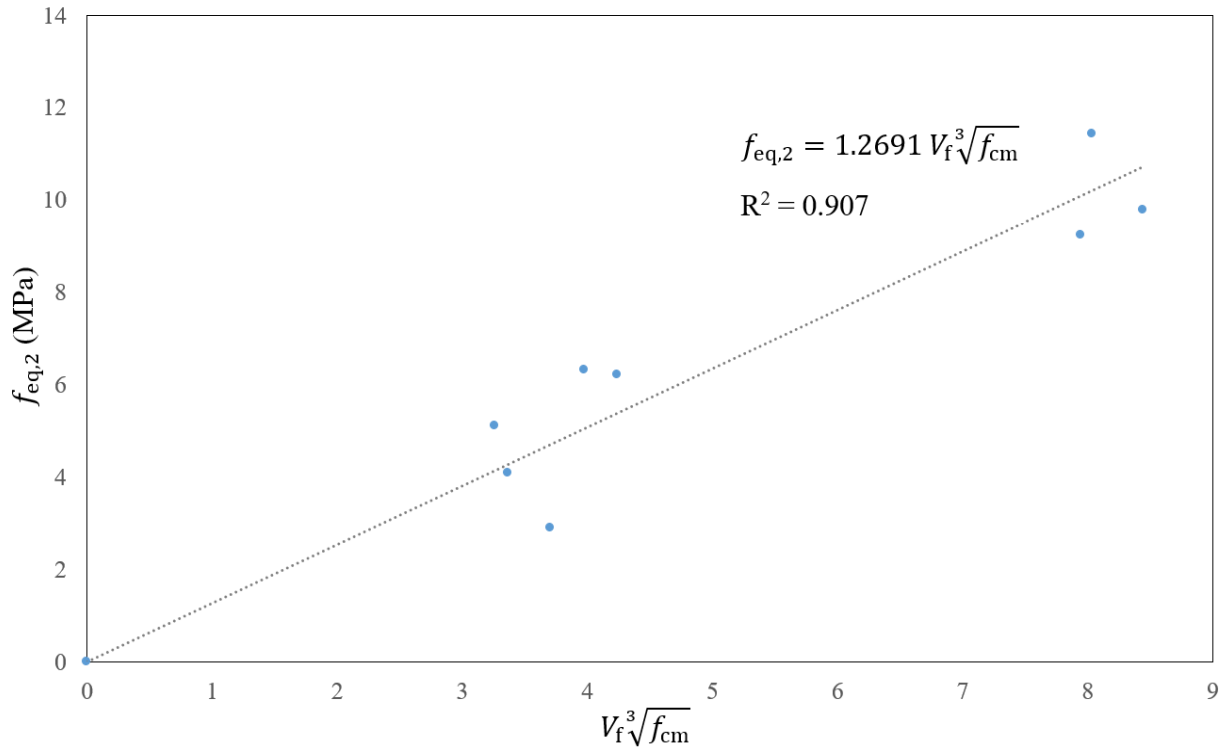
Figure 7 - Relationship between fibre volume fraction, V_f (%), average concrete compressive strength, f_{cm} (MPa) and $f_{eq,2}$ (MPa).
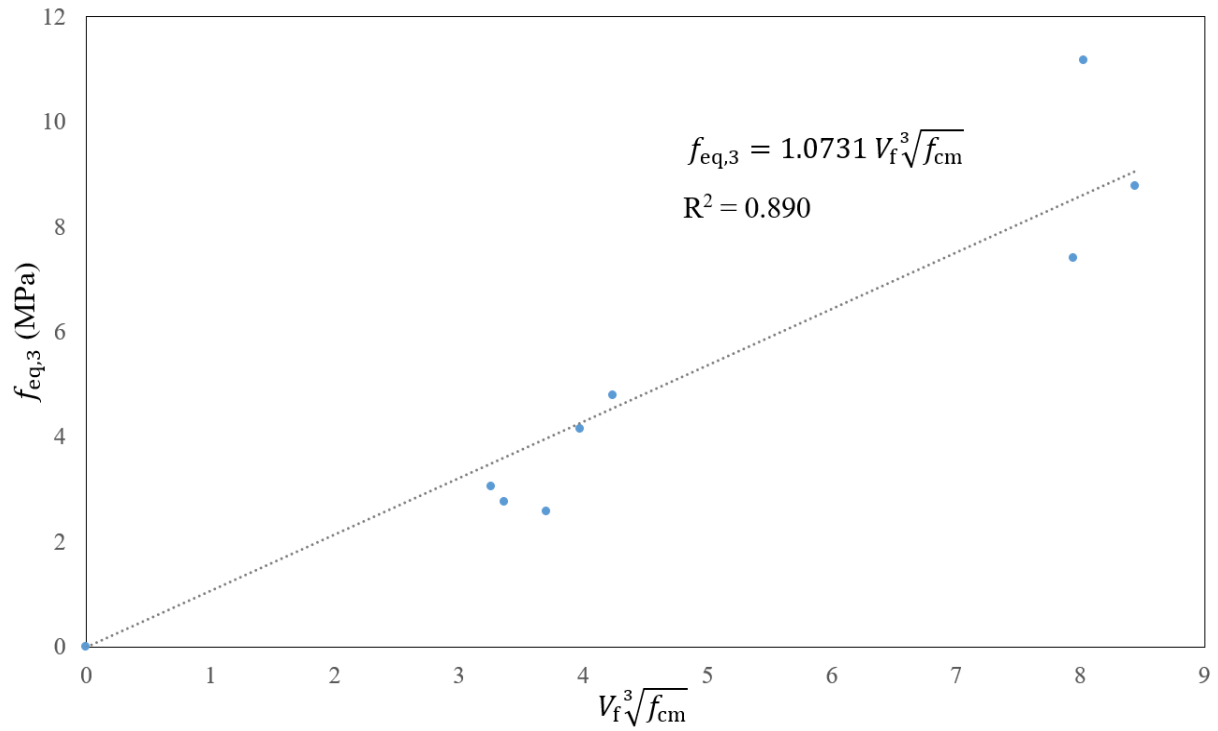
Figure 8 - Relationship between fibre volume fraction, V_f (%), average concrete compressive strength, f_{cm} (MPa) and $f_{eq,3}$ (MPa).
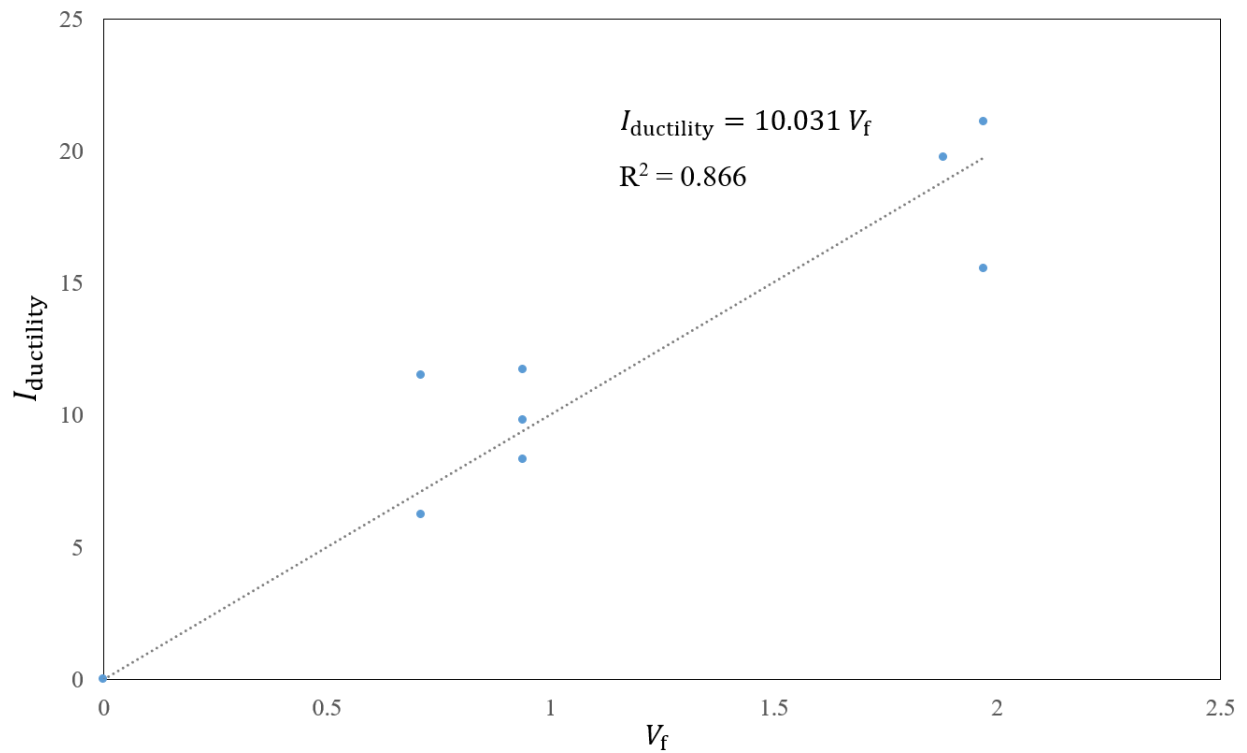
Figure 9 - Relationship between fibre volume fraction, V_f (%) and $I_{ductility}$.

Table 6 - The relationship between the fibre volume fraction, V_f (%), average concrete compressive strength, f_{cm} (MPa), ductility and post-cracking parameters of concrete reinforced by 55 mm macro basalt fibres.

Relationship between parameters	R-squared value
$f_{R1} = 1.3051\, V_f \sqrt[3]{f_{cm}}$	0.922
$f_{R2} = 1.1738\, V_f \sqrt[3]{f_{cm}}$	0.904
$f_{R3} = 0.906\, V_f \sqrt[3]{f_{cm}}$	0.786
$f_{R4} = 0.6869\, V_f \sqrt[3]{f_{cm}}$	0.725
$f_{eq,2} = 1.2691\, V_f \sqrt[3]{f_{cm}}$	0.907
$f_{eq,3} = 1.0731\, V_f \sqrt[3]{f_{cm}}$	0.890
$f_{R4} = 0.5233 f_{R1}$	0.739
$f_{eq,3} = 0.8421 f_{eq,2}$	0.934
$I_{ductility} = 10.031\, V_f$	0.866

6.   CONCLUSIONS AND FUTURE STUDIES

An experimental programme was performed, and 18 beams and 45 standard cylindrical samples made of macro basalt fibre concrete were tested. Four different fibre volume fractions and two different fibre aspect ratios, 65 and 84, were selected for this study. Compressive strength, density and bulk resistivity of cylinder specimens were investigated to evaluate the performance. Load-crack mouth opening displacement and load-mid span deflection of the beams were automatically measured utilising a 50 Hz acquisition system. Based on the analysis of the experimental results, the following conclusions are drawn from this study.

- The result of electrical resistivity test indirectly shows that the fibre concrete mixes have a high resistance to chloride ingress.
- By increasing the fibre content, a significant increase in ductility and post-cracking flexural strength of fibre concrete was observed. However, the flexural capacity at LOP was not notably affected by the fibre content.
- Based on the Pearson product-moment coefficient, both post-cracking behaviour and equivalent flexural strength were found to be a function of $V_f \sqrt[3]{f_{cm}}$ and the ductility to be a function of V_f.
- The results show that for the same fibre volume fraction (0.94%); the fibres with the aspect ratio of 65 show a wider deflection-hardening, $f_{eq,3}$ value and smaller standard deviation than the fibres with the aspect ratio of 84. However, since only a few samples of two different fibres have been tested, it is not possible to draw a conclusion regarding the effect of the fibre aspect ratio. Usually by increasing the fibres aspect ratio the performance of fibre concrete improves.
- There is a lack of knowledge about the durability, alkali ageing, shear capacity, fatigue behaviour, shrinkage and creep properties of macro basalt fibre concrete. Therefore, the authors suggest those properties as potential topics for future studies. Additionally, the mechanical behaviour of the hybrid system of macro basalt and chopped basalt fibres and the hybrid system of macro basalt fibre concrete and basalt fibre reinforced bars (BFRPs) need to be investigated for practical applications.
- Use of air-entraining agent could affect the bonding between fibres and concrete matrix. Therefore, due to the lack of knowledge, the authors suggest an extensive investigation on the bonding mechanism of macro basalt fibre concrete and the effect of entertaining

air-entraining agent, aggregate size and bond increasing additives on the flexural strength of fibre concrete.

Based on the conclusions, this study gives an estimation of the mechanical properties of macro basalt fibre concrete. However, the conclusions are based on the selected concrete mixes. The bonding mechanism and mechanical properties of fibre concrete are dependent on the composition of concrete matrix, mixing procedure, casting and curing conditions. Therefore, for structural applications, the designed concrete mix shall be adjusted and tested before casting.

ACKNOWLEDGEMENTS

REFERENCES

1. Lee S-J & Won J-P: "Flexural behavior of precast reinforced concrete composite members reinforced with structural nano-synthetic and steel fibers," *Composite Structures*, Vol. 118, 2014, pp. 571-579.
2. Holschemacher K, Mueller T & Ribakov Y: "Effect of steel fibres on mechanical properties of high-strength concrete," *Materials & Design*, Vol. 31, No. 5, 2010, pp. 2604-2615.
3. Hossain K, Lachemi M, Sammour M & Sonebi M: "Strength and fracture energy characteristics of self-consolidating concrete incorporating polyvinyl alcohol, steel and hybrid fibres," *Construction and Building Materials*, Vol. 45, 2013, pp. 20-29.
4. Soutsos M N, Le T T & Lampropoulos A P: "Flexural performance of fibre reinforced concrete made with steel and synthetic fibres," *Construction and Building Materials*, Vol. 36, 2012, pp. 704-710.
5. Buratti N, Mazzotti C & Savoia M: "Post-cracking behaviour of steel and macro-synthetic fibre-reinforced concretes," *Construction and Building Materials*, Vol. 25, No. 5, 2011, pp. 2713-2722.
6. Yoo D Y, Yoon Y-S & Banthia N: "Flexural response of steel-fiber-reinforced concrete beams: Effects of strength, fiber content, and strain-rate," *Cement and Concrete Composites*, Vol. 64, 2015, pp. 84-92.
7. Saleh M F, Yeow T, MacRae G & Scott A: "Effect of Steel Fibre Content on the Fatigue Behaviour of Steel Fibre Reinforced Concrete. *Proceedings*, 7th RILEM International Conference on Cracking in Pavements, 2012 (Springer).
8. Wang Z L, Wu J & Wang J G: "Experimental and numerical analysis on effect of fibre aspect ratio on mechanical properties of SRFC," *Construction and Building Materials*, Vol. 24, No. 4, 2010, pp. 559-565.
9. Dias D P & Thaumaturgo C: "Fracture toughness of geopolymeric concretes reinforced with basalt fibers," *Cement & Concrete Composites*, Vol. 27, No. 1, 2005, pp. 49-54.
10. Hooton R D & Bickley J A: "Design for durability: The key to improving concrete sustainabilit," *Construction and Building Materials*, Vol. 67, 2014, pp. 422-430.

11. Koch G H, Brongers M P H, Thompson N G, Virmani Y P & Payer J H: "Corrosion Costs and Preventive Strategies in The United States," *Publication* No. FHWA-RD-01-156., Federal Highway Administration, USA, 2002.

12. Zhishena W, Xina W & Ganga W: "Advancement of structural safety and sustainability with basalt fiber reinforced polymers," *Proceedings*, 6th International Conference on FRP Composites in Civil Engineering, Rome, Italy, 2012.

13. Banibayat P & Patnaik A: "Variability of mechanical properties of basalt fiber reinforced polymer bars manufactured by wet-layup method," *Materials & Design*, Vol. 56, 2014, pp. 898-906.

14. Dhand V, Mittal G, Rhee K Y, Park S J & Hui D: "A short review on basalt fiber reinforced polymer composites," *Composites Part B: Engineering*, Vol. 73, 2015, pp. 166-180.

15. Fiore V, Scalici T, Di Bella G & Valenza A: "A review on basalt fibre and its composites," *Composites Part B: Engineering*, Vol. 74, 2015, pp. 74-94.

16. ReforceTech. Basalt MiniBars Data Sheet. [cited 2017 12 September]; Available from: http://wpstatic.idium.no/reforcetech.com/2016/12/Basalt-MiniBars.pdf.

17. Morozov N N, Bakunov V S, Morozov E N, Aslanova L G, Granovskii P A, Prokshin V V & Zemlyanitsyn A A: "Materials based on basalts from the European North of Russia," *Glass and Ceramics*, Vol. 58, Nos. 3-4, 2001, pp. 100-104.

18. Ying S & Zhou X: "Chemical and thermal resistance of basalt fiber in inclement environments," *Journal of Wuhan University of Technology-Mater. Sci. Ed.*, Vol. 28, No. 3, 2013, pp. 560-565.

19. Ramachandran B E, Velpari, V & Balasubramanian N: "Chemical durability studies on basalt fibres," *Materials Science*, Vol. 16, No. 11, 1981, pp. 3393-3397.

20. Lee J J, Song J & Kim H: "Chemical stability of basalt fiber in alkaline solution," *Fibers and Polymers*, Vol 15 No. 11, 2014, pp. 2329-2334.

21. Sim J, Park C & Moon D Y: "Characteristics of basalt fiber as a strengthening material for concrete structures," *Composites Part B: Engineering*, Vol. 36, Nos. 6-7, 2005, pp. 504-512.

22. Scheffler C, T. Förster T, Mäder E, Heinrich G, Hempel S & Mechtcherine V: "Aging of alkali-resistant glass and basalt fibers in alkaline solutions: Evaluation of the failure stress by Weibull distribution function," *Journal of Non-Crystalline Solids*, Vol. 355, Nos. 52-54, 2009, pp. 2588-2595.

23. Girgin Z C & Yıldırım M T: "Usability of basalt fibres in fibre reinforced cement composites, *Materials and Structures*, Vol. 49, 2016, pp. 3309-3319.

24. Wei B, Cao H & Song S: "Degradation of basalt fibre and glass fibre/epoxy resin composites in seawater," *Corrosion Science*, Vol. 53, No. 1, 2011, pp. 426-431.

25. High C, Seliem H M, El-Safty A & Rizkalla S H: "Use of basalt fibers for concrete structure," *Construction and Building Materials*, Vol. 96, 2015, pp. 37-46.

26. Kizilkanat A B, Kabay N, Akyüncü V, Chowdhury S & Akça A H: "Mechanical properties and fracture behavior of basalt and glass fiber reinforced concrete: An experimental study," *Construction and Building Materials*, Vol. 100, 2015, pp. 218-224.

27. Kabay N: "Abrasion resistance and fracture energy of concretes with basalt fiber," *Construction and Building Materials*, Vol. 50, 2014, pp. 95-101.

28. Jiang C, Fan K, Wu F & Chen D: "Experimental study on the mechanical properties and microstructure of chopped basalt fibre reinforced concrete," *Materials & Design*, Vol. 58, 2014, pp. 187-193.

29. Ayub T, Shafiq N & Nuruddin M F: "Mechanical Properties of High-performance Concrete Reinforced with Basalt Fibers," *Proceedings*, Fourth International Symposium

on Infrastructure Engineering in Developing Countries, IEDC 2013, 2014. (Procedia Engineering).

30. Li W & Xu J: "Mechanical properties of basalt fiber reinforced geopolymeric concrete under impact loading," *Materials Science and Engineering: A*, Vol. 505, Nos. 1-2, 2009. pp. 178-186.

31. Li W & Xu J: "Impact characterization of basalt fiber reinforced geopolymeric concrete using a 100-mm-diameter split Hopkinson pressure bar." *Materials Science and Engineering: A*, Vol. 513-514, 2009, pp. 145-153.

32. Williams Portal N: "Sustainability and Flexural Behaviour of Textile Reinforced Concrete," *Doctoral Thesis*, Department of Civil and Environmental Engineering. Division of Structural Engineering, Chalmers University of Technology, Göteborg, Sweden, 2013.

33. Jacob A: "Vinyl esters lead the corrosion challenge," Reinforced Plastics, Vol. 47, No. 6, 2003, pp. 32-35.

34. Det Norske Veritas, DNV OS-C502, Offshore Concrete Structures, Norway, 2012.

35. Yazıcı S, İnan G & Tabak V: "Effect of aspect ratio and volume fraction of steel fiber on the mechanical properties of SFRC. *Construction and Building Materials*, Vol. 21, No. 6, 2007, pp. 1250-1253.

36. Norcem. A. S Brevik (Cement and Concrete Laboratory), Report on Quality Test (Ref. Num. A-l 2015-0003), 2015.

37. European Standard, NS-EN 12390-3:2009, Testing hardened concrete - Part 3: Compressive strength of test specimens. Norwegian Standard, Lysaker, Norway, 2009.

38. ASTM C1399/C1399M - 10, Standard Test Method for Obtaining Average Residual-Strength of Fiber-Reinforced Concrete. ASTM International, USA, 2010.

39. ASTM C1609/C1609M - 12, Standard Test Method for Flexural Performance of Fiber-Reinforced Concrete (Using Beam With Third-Point Loading). ASTM International, USA, 2013.

40. European Standard, NS-EN 14651:2005+A1: 2007, Test method for metallic fibre concrete - Measuring the flexural tensile strength (limit of proportionality (LOP), residual). Norwegian Standard, Lysaker, Norway. 2008.

41. Vandewalle L et al., RILEM TC 162-TDF: "Test and design methods for steel fibre reinforced concrete – Ϭ-ε-design method," *Materials and Structures*, Vol. 36, 2003, pp. 560-567.

42. Vandewalle L et al., RILEM TC 162-TDF: "Test and design methods for steel fibre reinforced concrete – Recommendations, Bending test," *Materials and Structures*, Vol. 33, 2000, pp. 3-5.

43. Vandewalle L et al., RILEM TC 162-TDF: "Test and design methods for steel fibre reinforced concrete – Final Recommendation, Bending test," *Materials and Structures*, Vol. 35, 2002, pp. 579-582.

44. Barros J A O, Cunha V M C F, Ribeiro A F & Antunes J A B: "Post-cracking behaviour of steel fibre reinforced concrete," Materials and Structures, Vol. 38, 2005, pp. 47-56.

45. Ding Y, Zhang Y & Thomas A: "The investigation on strength and flexural toughness of fibre cocktail reinforced self-compacting high performance concrete," *Construction and Building Materials*, Vol. 23, No. 1, 2009, pp. 448-452.

46. Yanga I H, John C & Kimb B-S: "Structural behavior of ultra high performance concrete beams subjected to bending, Engineering Structures, Vol. 32, 2010, pp. 3478–3487.

47. You Z, Chen X & Dong S: "Ductility and strength of hybrid fiber reinforced self-consolidating concrete beam with low reinforcement ratios.," *Proceedings*, International Conference on Risk and Engineering Management (REM), 2011. (Systems Engineering Procedia).

48. Olivito R S & Zuccarello F A: "An experimental study on the tensile strength of steel fiber reinforced concrete," *Composites Part B: Engineering*, Vol. 41, No. 3, 2010. pp. 246-255.

49. Shaikh F U A: "Deflection hardening behaviour of short fibre reinforced fly ash based geopolymer composites," *Materials & Design*, Vol. 50, 2013, pp. 674-682.

50. Akcay B & Tasdemir M A: "Mechanical behaviour and fibre dispersion of hybrid steel fibre reinforced self-compacting concrete," *Construction and Building Materials*, Vol. 28, 2012, pp. 287–293.

51. Yu R, Spiesz P & Brouwers H J H: "Development of Ultra-High Performance Fibre Reinforced Concrete (UHPFRC): Towards an efficient utilization of binders and fibres," *Construction and Building Materials*, Vol. 79, 2015, pp. 273–282.

52. Layssi H, Ghods P, Alizadeh A R & Salehi M: "Electrical Resistivity of Concrete: Concepts, applications and measurement techniques," *Concrete International*, Vol. 37, No. 5, 2015, pp. 41-46.

53. Spragg R P, Castro J, Nantung T, Paredes M & Weiss W J:, "Variability Analysis of the Bulk Resistivity Measured Using Concrete Cylinders," JTRP - Joint Transportation Research Program, Indiana Department of Transportation and Purdue University, West Lafayette, Indiana, USA, 2011.

54. Gjørv O E: "Durability Design of Concrete Structures in Severe Environments," CRC Press, 254, 2014.

55. Smith D: "The Development of a Rapid Test for Determining the Transport Properties of Concrete", *Master Thesis*, University of New Brunswick, New Brunswick, Canada, 2006, 94 pp.

56. Song P S & Hwang S: "Mechanical properties of high-strength steel fiber-reinforced concrete," *Construction and Building Materials*, Vol. 18, No. 9, 2004, pp. 669-673.

57. Xu B W & Shi H S "Correlations among mechanical properties of steel fiber reinforced concrete," *Construction and Building Materials*, Vol. 23, No. 12, pp. 3468-3474.

58. Pająk M & Ponikiewski T: "Flexural behavior of self-compacting concrete reinforced with different types of steel fibers," *Construction and Building Materials*, Vol. 47, 2013, pp. 397-408.

59. Löfgren L: "Fibre-reinforced Concrete for Industrial Construction - a fracture mechanics approach to material testing and structural analysis," *Doctoral Thesis*, Department of Civil and Environmental Engineering, Structural Engineering, Chalmers University of Technology, Göteborg, Sweden, 2005.

60. Miller, W., Statistics and Measurement Concepts with OpenStat. 2013. 237.

61. European Standard, NS-EN 1992-1-1: 2004+NA: 2008, Eurocode 2: Design of concrete structures Part 1-1: General rules and rules for buildings. Norwegian Standard, Lysaker, Norway, 2008.

62. International Federation for Structural Concrete (fib): Model Code 2010, first complete draft. Vol. 1, *Publication* No. 281, Lausanne, Swizerland, 2010.